INVESTIGATION OF FLOW AND EROSION CHARACTERISTICS THROUGH A SET OF RESTRICTING ORIFICES

BY

ARAOYE, ABDULRAZAQ ADENIYI

A Thesis Presented to the
DEANSHIP OF GRADUATE STUDIES

KING FAHD UNIVERSITY OF PETROLEUM & MINERALS

DHAHRAN, SAUDI ARABIA

In Partial Fulfillment of the
Requirements for the Degree of

MASTER OF SCIENCE

In

MECHANICAL ENGINEERING

DECEMBER, 2015

KING FAHD UNIVERSITY OF PETROLEUM & MINERALS
DHAHRAN- 31261, SAUDI ARABIA
DEANSHIP OF GRADUATE STUDIES

This thesis, written by **ARAOYE, ABDULRAZAQ ADENIYI** under the direction his thesis advisor and approved by his thesis committee, has been presented and accepted by the Dean of Graduate Studies, in partial fulfillment of the requirements for the degree of **MASTER OF SCIENCE in MECHANICAL ENGINEERING.**

Hassan Badr
Dr. Hassan M. Badr
(Advisor)

Zuhair Gasem
Dr. Zuhair Gasem
Department Chairman

Med Habib
Dr. Mohamed A. Habib
(Member)

Dr. Salam A. Zummo
Dean of Graduate Studies

Dr. Al-Sarkhi Abdelsalam
(Member)

19/4/16
Date

Dedicated to

My parents and siblings,

for their relentless support and encouragement

ACKNOWLEDGMENTS

I would like to thank Almighty Allah for His abundant mercies on me.

I wish to acknowledge my sincere gratitude to all those who have rendered their support in various ways towards the success of this study. First to my thesis advisor Dr. Hassan M. Badr and thesis committee members, Dr. Mohamed A. Habib, and Dr. Al-Sarkhi Abdelsalam, as their understanding, recommendations, criticisms and corrections are far more than expectations. Then to all faculties and staffs in the Department of Mechanical Engineering for their academic support and hands on job intervention.

My sincere appreciation goes to my parents, Alhaji Rasheeed Araoye and Mrs. Risikat Araoye for their supports in terms of moral, financial, encouragements and unrivaled support. May Almighty Allah bless and reward them abundantly. I wouldl also like to recognize the supports of my very good friends and siblings, Mr. Araoye Ibrahim and Miss. Araoye Rasheedat.

TABLE OF CONTENTS

LIST OF TABLES

LIST OF FIGURES

ABSTRACT

Full Name : ARAOYE, ABDULRAZAQ ADENIYI
Thesis Title : INVESTIGATION OF FLOW AND EROSION CHARACTERISTICS THROUGH A SET OF RESTRICTING ORIFICES
Major Field : MECHANICAL ENGINEERING
Date of Degree : DECEMBER, 2015

This study investigates the erosion and flow characteristics in a serial arrangement of two similar bevel-edged thin orifice plates with different diameter ratios and orifice spacing. The single or double-orifice arrangements were tested in one-inch-diameter carbon steel pipe. A fully developed pipe flow was ensured well upstream and downstream the orifice arrangement. The numerical analysis was performed on FLUENT 12.1 using the k-ε eddy viscosity model and the discrete phase model (DPM) in conjunction with relevant erosion correlations to predict the flow and erosion features in the orifice spacing and downstream the orifice arrangements. The continuous phase is water while the dispersed phase is sand. To verify the computational results and have a better understanding of the flow regime, an experimental setup was locally designed and manufactured. The flow velocity was measured using Particle Image Velocimeter system (2D-2C PIV) while the pressure drop across the orifice configurations were measured using simple manometers.

The effects of various parameters such as pipe flow velocity in the range 1−4m/s, diameters of sand particles within the range 50−400μm, orifice spacing of 1D and 2D, and orifice plate diameter ratios of 0.5, 0.63 and 0.77 have been considered. Validation of the computational code was carried out through several comparisons with previous computational results as well as present experimental PIV measurements. The presence of vena contracta downstream of the first orifice was verified computationally and experimentally, however the presence of vena contracta downstream of the second orifice was found to depend on the orifice spacing. Not only the flow structure between the two orifices and downstream the second orifice was found to depend on the orifice spacing but also the total pressure drop and hydraulic losses.

The double orifice configuration with one pipe diameter spacing was found to produce the least pressure drop due to reduced hydraulic losses. The investigation of solid particle erosion in the entire domain revealed the presence of two critical erosion locations downstream the second orifice namely the recirculation and reattachment zones. The least erosion rate was found for double-orifice configuration with 1-D spacing. Although a high-velocity region exists in the spacing between the two orifices, it experienced negligible erosion for large particle size $\left(D_p \geq 100\ \mu m\right)$. The results also showed strong dependence of erosion rates on the parameters investigated. Erosion rates increases as orifice diameter ratio and diameters of solid particles decreases and as flow inlet velocity increases.

Keywords: erosion, pressure drop, multiple orifices, PIV, two-phase flow

ملخص البحث

الاسم الكامل: عراوأي عبد الرزاق أديني

عنوان الرسالة: تحقيق التدفق وخصائص التأكل من خلال مجموعة فى تقييد الفوهات

التخصص: الهندسة المكانيكية

تاريخ الدرجة العلمية: ديسيمنبر 2015

تبحث هذه الدراسة التآكل وخصائص السريان في الشكل التسلسلي فوهتين متماثلتين رقيقتين ذو شطبتين حادتين مع نسب قطر مختلفة ومسافات مختلفةبين الفوهتين. تم اختبارمنظومات مفردة أو مزدوجة الفوهة في انبوب قطره بوصة واحدة من الصلب الكربونى. تم ضمان ان السريان كامل التطور من صعيد وسافل ألفوهة. كما تم إجراء التحليل العددي باستخدامم برنامج Fluent 12.1 باستخدام نموذج الدوامة و اللزوجة (k-ε) ونموذج الطور المتقطع (DPM) بالتزامن مع معادلات التآكل ذات الصلة للتنبؤ بالتدفق ومظاهر التآكل في المسافه بين الفتحات وفي سافل الفوهة مع العلم بأن الطور المستمر هو الماء في حين أن الطور المتناثر هو الرمال. وللتحقق من النتائج الحسابية والحصول على فهم أفضل للسريان، تم إعداد جهاز تجريبي مصمم ومصنع محليا حيث تم قياس سرعة التدفق باستخدام نظام قياس السرعة عن طريق تصوير الجزيئات PIV (2D-2C) ، في حين تم قياس هبوط الضغط عبر الفوهة باستخدام مانومترات بسيطة.

وقد تم دراسة تأثير معايير مختلفة مثل سرعة التدفق داخل الأنابيب في الحدود 4m/s-1 , أقطار حبيبات الرمل في الحدود 400µm-50 ، تباعد فوهة 1D و 2D، وتم اعتبار ان فتحة اللوحة قطرها 0.5، 0.63 و 0.77 كما وتم التأكد من صحة نتائج البرنامج الحسابي من خلال عدة مقارنات مع النتائج الحسابية السابقة وكذلك عن طريق القياسات الحاليةباستخدام PIV. وقد تم التحقق من وجود vena contracta سافل الفوهة الأولى حسابيا وتجريبيا، ولكن وجود vena contracta سافل الفوهة الثانية تعتمد على المسافة البنية مع الفوهة الأولى. وقد وجد انه ليس فقط التدفق بين الفوهتين وسافل الفوهة الثانية هو الذي يعتمد على مسافة الفوهة ولكن أيضا هبوط الضغط الكلي والفقودات الهيدروليكية.

وقد تم التأكد من ان الشكل ذو الفوهة المزدوجة مع مسافة بين الفوهتين مساوية لقطر انبوب واحد تعطي اقل هبوط في الضغط وذلك من خلال تقليل الفقودات الهيدروليكية. كما كشفت دراسة تاكل الجزيئات الصلبة في المجال بأكمله كشفت وجود موقعين للتآكل الحرج سافل الفوهة الثانية وهي مناطق إعادة التدوير وإعادة المرتكز ووجد ان اقل معدل تاكل في حالة الفوهة المزدوجة

مع مسافة بينية قدرها قطر واحد. وعلى الرغم من أن منطقة السرعة العالية موجودة فى االمسافة بين الفوهتين, حيث انها شهدت قليل من التآكل يمكن تجاهله للجزيئات ذات الحجم الاكبر. كما أوضحت النتائج اعتماد قوي لمعدل التاكل علي الوسائط التي تم دراستها.تزيد معدلات التآكل بنقصان نسبة قطر الفتحة وقطر الجزيئات الصلبة وايضا تزيد بزيادة سرعة التدفق الداخل.

كلمات البحث: تآكل، انخفاض الضغط، فتحات متعددة، **PIV**، السريان ذي الطورين.

CHAPTER 1

INTRODUCTION

Many engineering applications involving internal flows utilize restrictions such as valves, tees bends, and orifices to achieve control of pressure, flow direction and flow rates. Due to the simplicity in design and ruggedness in use amongst other attributes, orifice plates in conjunction with carrier assemblies, pressure taps, flange and sometimes micro-computers are the most widely used differential flowmeter. Orifice meters are suitable for measurement in both steady and unsteady pulsating flows [1, 2]. As restricting orifices, they are used to attain a high level of atomization without cavitation even at large pressure difference in spray atomizers, as control measures in HVAC, for quality control in food processing industry and metering of high viscous liquids and calibrating tools in metrology of vacuum or gas flows [3]. Single orifices can also be used to enhance uniformity in flow distribution and exchange of heat and mass as applicable in pre-mixed combustion.

However, the use of restricting orifices results in a high-pressure loss which may lead to energy loss and non-linear characteristics that intensify the effect of pulsation on various measurements, cavitation effect in liquids or critical flow in gases. There is also the issue of increased flow velocity induced by restricting orifices which enhances the material loss in flow accelerated corrosion. The use of multistage restricting orifices is becoming essential in applications requiring higher pressure drop that cannot be achieved by a single orifice. Some designs of multi-hole orifices and multiple orifices are suitable for achieving a lower pressure drop because of their high discharge coefficient [4, 5]. A multistage orifice tube can be used to achieve a higher pressure drop through the effective arrangement of the orifices and optimum geometry design as applicable in the pipe letdown line in cooling systems of power plants and other process controls [6].

The extensive application of orifice plate is due to its flexibility in usage, lesser cost and the wealth of data gathered over the years and documented in standards like ISO 5167, BS1042, ANSI, which makes design, construction and uncertainty calculations convenient. Moreover, the simplicity in structure, reliability and longevity of the orifice plate makes it different from other devices such that some of its applications may not require calibration before use when manufactured and installed following standard procedures. Different types of orifice plates in use are concentric, eccentric, segmental, quadrant edge and conical edge plates. Their applications are guided by standard practices like the area ratio which must be within certain recommended limits. An orifice is said to be thick if its thickness to diameter ratio (t/d) is greater than 0.5 otherwise, it is called thin orifice [7].

Characteristics of flow through an orifice have been studied extensively both numerically and experimentally. Numerous works have been published for the numerical investigation of orifice flow using software like ANSYS CFX-10 [4], MATLAB and OPEN-FOAM 1.6 [8] and most utilized ANSYS/FLUENT. Also, experimental investigations have been carried out in the past using measurement techniques such as Pitot tube, Hot Wire Anemometer and in recent times with laser techniques such as Laser Doppler Anemometry (LDA) [9], Particle Image Velocimetry (PIV) [10] etc. PIV is a non-intrusive, relatively accurate, reliable and convenient flow measuring technique. It is a powerful diagnostic tool that gives quantitative measurements of whole field velocity profile for single- or multiphase flows at high temporal and spatial resolutions. This technique has contributed immensely to the knowledge of fluid dynamics and the advancement and continuous development in methodology and hardware components have placed it amongst standard flow measuring techniques[11–13].

The underlining principle of orifice flow is the creation of pressure difference across the orifice plate. The flow pressure decreases towards the orifice windward face, decreases within the orifice, reaches its minimum at the vena contracta and builds up afterward. The behavior of single-phase flow passing through a thin orifice is such that it contracts to a region of minimum area downstream of the orifice known as the vena contracta with the minute loss of energy and irreversibly re-attaches to the pipe wall further down the flow channel. Whereas for a thick orifice plate, the vena contracta appears within the orifice opening with reattachment occurring twice at the outer edge of the orifice and at the pipe wall downstream. The presence of the restriction in flow paths in the form of orifices, valves or sudden contraction influences the flow field characteristics. An orifice plate placed in flow paths distorts the upstream fully developed flow in its vicinity, creates recirculation zones on both sides and a reattachment zone further downstream.

The region between the orifice plate and reattachment location is important in this study because it is characterized by the greatest sudden change in turbulent flow parameters due to change in geometry [14]. This region has also been found to be most susceptible to solid particle erosion, flow-accelerated corrosion (FAC), and Liquid Droplet Impingement Erosion (LDIE). Nemitallah et al. [15] reported that the maximum wear rate by solid sand particles occurs in the reattachment zone at approximately 4.4 pipe diameters downstream of the orifice. Thinning of pipe walls due to LDIE is prominent in the reattachment zone at approximately two-pipe diameters downstream of the orifice [16]. Locations of maximum Mass Transfer Coefficient (MAC) due to FAC occur in the reattachment zone at 2-3 pipe diameters downstream of the orifice [17,18]. Internal flow fluctuations in these zones can also induce noise in the pipe which may excite the confining surface leading to disturbance of external flows [19].

Erosion is gradual removal of pipe materials through impingements either by solid particles or liquid droplet. Studies on erosion characteristics and methods of erosion mitigation have been an important research area over the years because of the debilitating effects of erosion on pipes mostly used in water treatment plants, product transportation in petrochemicals and petroleum industries or heat exchangers in power plants. Negative impacts of erosion lead to loss of revenue due to downtime of plant operation, damage of equipment or complete breakdown of a whole system. Hwang et al. [16] cited cases of an inch diameter low moisture steam extraction pipe in a 1000MWe Korean PWR and an equal diameter high moisture, high-pressure stream extraction pipe in Arkansas Nuclear One Unit in the USA where erosion caused pipe leakages downstream of the orifice in April 2013 and February 2009 respectively.

The mechanism of erosion depends on several factors such as properties of target material in terms of hardness [20], eroding substance in terms of size, shape, concentration, impact velocity and impact angle [21, 22], fluid properties such as velocity and flow characteristics resulting from flow passage geometry [23]. The flow structure in straight sections like pipes are subjected to random impingements due to flow fluctuations while the nature of impingement on the target material is direct for flow regimes in elbows, tees or containing flow components such as orifices, valves. The total volumetric erosion by impact is the summation of two well-known erosion mechanisms of micro-cutting and deformation erosion [24]. Erosion models have been developed for each mechanism in the form of separate discrete models and combined model [25, 26].

Numerous studies were carried out to investigate the effects of parameters such as flow velocity, particle size, flow properties on erosion rate in straight pipe sections, elbows, tees and orifices [15, 27, 28]. The experimental studies on erosion are targeted at providing data for developing correlations to establish a relationship between the erosion rate and the controlling factors while the numerical simulations of erosion characteristics are mostly intended for better understanding. Different methods of reducing the occurrence of erosion have been devised over the years. The most common method is material selection approach which involves the use of composites for pipes such as 2% chromium steel. Another method is the design approach which involves increasing the target material thickness in the critical regions or fixing of protruded pipe at the point of sudden contraction was suggested by [29]. Badr et al. [30, 31] proposed the dynamics approach of determining the threshold velocity below which negligible erosion rate is observed.

In lieu of this, this study focusses on the computational investigation of erosion characteristics in single and multiple orifices. Very little work has been done on the effect of orifice spacing on flow characteristics and study of erosion phenomenon in serial arrangement of multiple orifices. Most works on multiple orifices have been on applications requiring higher pressure drop devoid of the existence of cavitation. This work proposed multiple orifice configurations capable of producing lower and higher pressure drops than single orifice and an in-depth knowledge of their flow characteristics was seen to serves as the basis for understanding erosion characteristics. This necessitates the experimental and computational study of flow characteristics in the single orifice and serial arrangement of two orifices.

1.1 Problem Description

The present study considers the investigation of erosion and flow characteristics downstream an ANSI specified thin concentric bevel-edged orifice/s of varying diameter ratios; 0.5, 0.63 and 0.77 placed in a 1-inch internal diameter horizontal pipe by computational analysis using FLUENT 12.1 CFD code. In the case of two orifices, orifice spacing of one and two pipe diameters was adopted based on the submission of [10] that the shear layer region develops from the orifice edge and merge at a distance of one pipe diameter downstream. The orifices are assumed to be placed in the fully developed region of the flow by ensuring adequate upstream straight pipe section of 35 pipe diameter and a downstream length of 60 pipe diameter. The fluid used is water, pipe walls are made of carbon steel, spherical sand particles served as erosive particles and the orifice plates are modeled to be wear resistant. A parametric study was carried out to study the effect of inlet velocity, orifice size, orifice spacing and sand particle diameter on erosion rates. The inlet velocities and particle diameter sizes considered were 1m/s, 2m/s, 4m/s and 50μm, 100μm, 200μm, and 400μm respectively. An experimental study was also carried out using 2D/2C digital Particle Image Velocimetry (PIV) measuring technique to determine flow behavior involving orifice of diameter ratio 0.63 for configurations similar to the computational work. The test section and orifices were fabricated from Plexiglas.

1.2 Objectives

The objectives of this work are:

- To determine velocity and pressure profiles
- To measure, pressure drop across the orifice plate
- To study the effect of diameter ratio on flow behavior
- To investigate flow fields in a series of restricting orifices
- To study erosion characteristics in both single and multiple restricting orifices

CHAPTER 2

LITERATURE REVIEW

Extensive work has been done in the study of flow field characteristics of a single phase of gasses, liquids and multiphase flows through an orifice by investigating the effects of parameters like flow velocity, orifice size, and pipe size numerically and experimentally. The important flow characteristics studied are velocity distribution, pressure distribution, void fraction, turbulence parameters, discharge coefficients and cavitation effects with the goal of establishing a relationship with the orifice geometry.

A numerical study by CFD computations of two-phase flow through orifices of different geometries in terms of thickness and size was conducted by Mammatha and Sukamta [32] using the Eulerian-Eulerian model to determine the variation of pressure losses with different geometries while taking into consideration the influence of orifice plate on void fraction distribution. Hollingshead et al. [33] carried out performance analysis of four differential pressure flow meters types namely Venturi-tube, wedge, standard concentric orifice and V-cone based on discharge coefficient by modeling flow at low Reynolds number using FLUENT software and established equations for correction factors of discharge coefficient at low Re. The equation shows the dependence of the correction factor on the discharge coefficient of flowmeter type and Reynolds number.

An extensive analysis of the effect of orifice sizes on flow characteristics for turbulent air flow involving a circular concentric bevel-edged orifice was done by Eiamasa-ard et al. [34]. The orifice diameter ratios used were 0.5, 0.6 and 0.8. They also studied the influence of turbulence model on results by comparing the standard k-ε model with the Reynolds-stress model. In solving the conservation equations of mass and momentum, the SIMPLE ALGORITHM was employed to de-couple the velocity-pressure relationship while comparing three different types of convection and diffusion transport discretization methods namely first order-upwind, second order-upwind and QUICK. The obtained downstream flow has features like recirculation zone, shear layer zone, and reattachment zone. Better flow representation was achieved with the second order upwind scheme. The RSM model prediction of flow downstream the orifice is closer to the experimental results than the standard k-ε model. The standard k-ε model under predicts the velocity distribution and over predicts the pressure distribution in that region. They also noticed that the reattachment length predicted by RSM is longer than that of the standard k-ε model. They, however, concluded that both models are good enough for orifice flow prediction. Regarding the effect of orifice size, they observed that decreasing orifice size leads to bigger recirculation zone and longer downstream distance to re-attain uniform distribution.

Dabiri et al.[35] determined the cavitation sites for laminar and turbulent liquid flow through atomizer's orifice by solving the Navier-Stokes equation for two-dimensional, viscous, incompressible axisymmetric flows using the Finite-Volume approach by Patankar [36] and made a comparison between the pressure and total stress criteria. Results showed that the total stress criterion gives a better prediction of cavitation for laminar flows than the pressure criterion, a little difference in their predictions for turbulent flow and that cavitation is less likely to happen at high Reynolds numbers. They explained that the pressure (traditional) criterion links occurrence of cavitation to the drop of liquid pressure below the fluid vapor pressure while total stress criterion assumes cavitation occurs when the maximum principal stress (viscous stress + pressure) is lower than the vapor pressure.

Nygard and Andersson [37] carried out numerical simulation by solving 3-D Navier-Stokes equation in cylindrical coordinates for an incompressible turbulent flow through a pipe with sudden axisymmetric constriction of 0.5D. They utilized the 'direct forcing' scheme of IBM (Immersed Boundary Method) to embed the boundary conditions of the constriction in the equations. They obtained a good prediction for the upstream flow profile and attributed the slight difference in the downstream velocity profile and greater turbulent kinetic energy to lower Reynolds number used and the periodicity on the IBM scheme used and insufficient inlet length for fully developed flows when compared with experimental results. They also showed that the Coanda effect (causing flow asymmetry) which is inherent in planar symmetric flows due to the disconnected pressure profile is absent in axisymmetric flows because of the even distribution of low pressure along the length of pipe downstream. The Coanda effect created a reduction in pressure which spreads along pipe length and results in asymmetric flow behavior. A comprehensive study was also done on the efficient analysis of flows through a pipe fitted with an orifice by Nilsson et al. [38] using Phoenics CFD commercial code.

Arun et al. [39] conducted a computational study, using FLUENT, on the discharge coefficient of non-Newtonian fluids using SCMC (sodium salt of carboxymethyl cellulose) of densities 0.2, 0.4, 0.6 and 0.8 kg/m^3 by varying the pipe diameter; 50, 100 and 200mm, diameter ratio, D_r; 0.4, 0.6, and 0.8 and flow velocity within $100 < Re < 10^5$. Results showed that for all SCMC densities, the discharge coefficient increases with Reynolds number up to a certain high Reynolds number where it assumes a constant value. Also, the discharge coefficient increases with increase of SCMC density and decreases with increase in the pipe diameter at each D_r over the range of Reynolds number considered. A model for the prediction of pressure drop and discharge coefficient over a wide range of Re for incompressible flow through orifice tube was developed by Jankowski et al. [40]. Orifice tube refers to an orifice with a very high thickness to diameter ratio and is mostly used for creeping flows.

Computational solutions are beneficial in increasing our understanding of flow field behavior. In order to establish a relationship between factors influencing the flow field like Reynolds number, diameter ratio, flow velocity, erosion determinants, experimental works are required. Bull and Agrawal [19] carried out an experimental study of turbulent flow characteristics in the fully-developed region of a horizontal pipe by varying the orifice diameter and rate at which air flows. Their results showed profiles of Mach number and velocities at pipe centerline, sites at which separated and reattachment flows occurs and the relationship existing between these flow regions and turbulence properties.

Ramamurthi and Nandakumar [41] investigated experimentally the discharge coefficient and cavitation in the recirculation and reattachment region for water flowing through a small sharp-edged concentric orifice by varying parameters such as orifice diameter, aspect ratio, and Reynolds number. They explained that the inception of cavitation occurs at Reynolds number higher than that at which the cavitated flow reverses back to the attached flow. They also discovered that the discharge coefficient depends on Reynolds number and aspect ratio in the attached flow region and depends on the orifice diameter in the separated flow with cavitation. Shah et al. [8] employed a combination of experimental and numerical methods using OPEN-FOAM 1.6 to carry out a comprehensive analysis of orifice flow. They reported that the turbulent intensity value specified for inlet and outlet boundary conditions has negligible effects on the velocity profiles obtained by the k-ε model.

Morrison et al. [42] investigated experimentally how the three parameters Swirl (15°, 45°) β-ratio (0.5, 0.75) and Reynolds number (54700, 91100 and 122800) influence wall pressure in orifice flowmeters for air. Swirl similar to disturbances induced by pipe fittings like valves, bends, tees was generated upstream using a swirl generator and the pipe wall pressure was monitored across a length of 4D upstream to 6D downstream. They reported that the upstream wall pressure is independent of β-ratio. The increase in swirl reduces the inlet pressure and increases the downstream wall pressure; thus, pressure drop decreases. Also, the discharge coefficient increases as the swirl increases. Enrique et al. [43] carried out a 3-D numerical study validated with experiments on the effects of vortices and dead zones inherent in the downstream for non-Newtonian fluid flowing through an orifice meter designed for such purpose. They found that a high pressure is required to minimize the effect of vortices and dead zones with abrupt contractions of 8:1 ratio and suggested a semi-hyperbolic die geometry to achieve the same results at lower pressure.

Dempster and Arebi [44] performed experiments to study the effects of varying flow rates of neighboring orifices on the bubble characteristics in a parallel arrangement of three orifices of similar size with 1mm and 10mm separation distance in a subcooled water column. They reported that the flow conditions in each orifice are independent of one another. Singh and Tharakan [4] compared the pressure recovery associated with a single- and multi-hole orifice flowmeters over an Re range of 500-20,000. The multi-hole orifice has one central hole and eight periphery holes arranged on pitch circle diameter sized to have the same total flow area as the single-hole orifice flowmeter. The CFD simulation of the flow of water through the two types of flowmeters considered was carried out on

ANSYS CFX-10 by using the finite-volume method with coupled solver to ensure fully implicit discretization of the equation and was used to solve pressure-velocity coupling in the momentum equation. The boundary conditions were specified as static pressure and mass flow rate at the inlet and outlet faces. They discovered that the multi-hole orifice flowmeter produced a better pressure recovery and has a higher discharge coefficient over the Re range considered than the single orifice flowmeter. They attributed the lower pressure drop to the smaller eddies generated downstream the multi-hole orifice. They also pointed out that the lower velocity magnitude downstream the multi-hole orifice allows the turbulent parameters to mix better and as such makes it more accurate has a flowmeter.

Reis et al. [45] carried out a CFD simulation to model turbulent flow of natural gas through a non-premixed industrial burner. The burner can be taken as a multi-hole orifice. They also compared the different turbulence k-ε models of standard, RNG, Realizable and RSM in terms of flow characteristics such as velocity and pressure distribution and discharge coefficient to determine the model that gives the most accurate representation of experimental data for flow through the non-premixed industrial burner. They concluded that the predictions of all the models agree well with the experimental results and the Realizable model is the most suitable in terms of accuracy and computation time. The standard k-ε model gave the least computation time while RNG and RSM are the most accurate. The minimum center to center spacing of orifices on a multi-hole orifice required to achieve negligible influence on air flow due to neighboring orifices was determined by Gronych et al. [3]. They monitored the total conductance while measuring the transition to translational flow from molecular flow regime. They found the suitable spacing to be approximately thrice the orifice size.

Alimonti et al. [5] measured the flow characteristics of air-water two-phase flow through a WILLIS MOV (multiple orifice valve) which comprises of two-disc sets with equal orifice size. The WILLIS MOV consists of an inlet section, a diverting section followed by a set of discs with holes for flow regulation. A rotating disc moves over the stationary one to regulate the flow. Three different sizes of disc sets with varying thickness to diameter ratio of 1.41, 1.66 and 2.21 at orifice thickness of 30mm and a range of two-phase flow rates were used to analyze the two-phase multiplier, frictional pressure drop, and void fraction. The available two-phase multiplier correlations were adjusted by changing the constants to achieve a reasonable agreement with experimental results. They reported that the flow structure at high flow rates is in the form of separation such that the gas phase concentration is more at the core vortex while the valve wall is occupied by the liquid phase. They also observed swirl motion at the valve outlet which was related to the existence of radial velocity component that influences the pressure value. They concluded that two-phase flows are likely to have higher pressure value at the multiple valve outlet than liquid flow because the air-liquid flow has a lower density.

Haimin [6] carried out experiments to determine the optimal design of a multistage letdown orifice tube to achieve a higher pressure drop of 14.82 MPa at a flow rate of 22.7 m^3/h in the cooling system of a nuclear power plant. The multistage orifice tube designed is 700mm in length and contains 6 orifices (stages) with a constant distance of separation of approximately 2.4D. The internal orifices are eccentric orifices with staggered centers fixed to the pipe with constant orifice sizes while the first and last orifices (inlet and outlet orifices respectively) are concentric removable ones. The pressure control was investigated by varying the sizes of orifices at the multistage tube inlet and outlet for flow of water at an inlet temperature of 54.4ºC. The pressures upstream the first orifice and downstream every orifice were recorded. They observed that the first produces the highest pressure drop out of the six irrespective of the method of pressure control and that the highest pressure drop was achieved with the smallest orifice size considered at either the first or sixth stage. The inlet pressure control method was chosen to have given a better total pressure drop (the difference between the pressure upstream the first orifice and pressure downstream the sixth orifice) based on the required flow parameters. They also investigated the possibility of cavitation effects at every stage of the optimum orifice tube design to conclude that the design is free of cavitation.

A design of orifice meter was proposed by Shaaban [46] which involves the installation of a ring of optimum size at an optimum downstream location to achieve reduced gas pressure loss which invariably decreases the energy loss at even a reduced upstream installation distance. The ring is a sharp-edged concentric disc with 7° tapered edge. The diameter ratio of the orifice is 0.5 and the range of diameter ratio and downstream location of the ring considered are 0.38-0.58 and 0.2D-0.7D respectively for $Re = 1.8\times10^4$. The downstream location of the ring was determined by the location of the vena contracta for the given orifice size. The optimization of pressure loss was achieved through CFD simulation and generic algorithm. The solution was obtained using FLUENT finite-volume approach with RANS flow solution in an axisymmetric domain using the Realizable k-ε model with SIMPLEC and second order upwind discretization schemes for pressure-velocity coupling and convection-diffusion flow constituents respectively. The optimum diameter ratio and location of ring discovered are 0.5 and 0.38D respectively. Results show that the new design with ring produces an approximate reduction in pressure drop of 33.5% and 17%

increase in discharge coefficient for Re=1.8×10^4. The installation of ring reduces wall recirculation and velocity gradient in the shear layer region.

Some studies have also been done on the experimental determination of flow structures in pipes with or without orifices using optical techniques. DeOtte et al. [9] investigated the velocity profile around a 0.5 diameter-ratio orifice experimentally using 3-D Laser Doppler Anemometry (LDA) for airflow at Reynolds number 54700 through a 50mm diameter pipe. Instantaneous velocities were obtained from the LDA which were used in calculating means, variances and covariances of velocity for better understanding of flow characteristics associated with orifices. They concluded that the trend of turbulence kinetic energy is such that it increases slowly from the orifice face downstream to the vena contracta due to the presence of the shear layer. This is followed by a rapid increase in the region between the vena contracta and reattachment zone due to deceleration complementing the shear forces and diffuses away after the recirculation region because of the decrease in magnitude of velocity gradient in radial direction. The centerline variation of the turbulent kinetic energy was described using the covariance of velocities.

Shan et al. [47] used Particle Image Velocimetry (PIV) measuring technique to carry out a detailed investigation of flow characteristics behind a square-edged concentric orifice by varying the Reynolds number to obtain the instantaneous and mean velocities. They carried out a detailed analysis of the shear layer region in relation to turbulent parameters such as turbulent intensity and Reynolds shear stress. A comparison between the experimental results from PIV and numerical results from Reynolds Stress Model (RSM) shows a good agreement up to the vena contracta and a slight difference beyond this point. They also made a comparison between orifice flows and other separated flows and concluded that remarkable difference exists beyond one pipe diameter distance downstream because the shear layer begins to merge at an approximate distance of one pipe diameter downstream the orifice.

The effects of chemical constituents of water in terms of density on flow accelerated corrosion, FAC rate was investigated by Rani et al. [14] by comparing the Sherwood number for heavy water and light water flow (based on Fe ions constituents of water) through an orifice at high Re. The numerical simulation was carried out using FLUENT 12.1 and the conservation equations of continuity and momentum were solved using Realizable k-ε, RSM model. They also studied the turbulence parameters of the flow such as TKE, dissipation rate, Reynolds shear and normal stresses, wall shear stress and reported that they have maximum values in the recirculation region. The recirculation region was considered to be very important in this study it was believed to experience the greatest sudden change in turbulent flow parameters due to change in geometry and this has significant effects on the rate of mass transfer. There was negligible difference in the MTC values recorded for both water types prior to the location of peak MTC after which there is a reasonable difference with the heavy water flow yielding higher values due to the higher Fe constituents. Also, the peak Sherwood number was discovered to exist at the center of the recirculation region which justified the correlation of MTC with TKE.

Wood et al. [24] studied the wear rate in straight pipe and bends for slurry flows by computation using a combination of CFD and erosion models and compared the results with wear measured with micrometer/ultrasonic equipment. A level of agreement between both results was achieved and they reported that the most susceptible areas to wear rates for slurry flows in straight pipes and bends are the side walls and exterior curved surface respectively. The constituents of the slurry flow are water and sand particle of diameter 1mm and density 2670kg/m^3 and the target material is carbon steel with a density of 7850 kg/m^3. The solution procedure involves using the standard k-ε model flow solution on FLUENT v5.4 to predict the impact velocity distribution and impact angle which were incorporated into modified Hashish–Bitter erosion model for the determination of wear rates. The erosion rate distribution in upstream straight pipe section and bends made of AISI 304L stainless steel for flow of water-sand mixture with 10% solid particle concentration by volume at 3m/s was also investigated by Wood and Jones [48] and the comparison between the erosion results from their CFD simulation and experiments shows correctness of numerical computations.

Badr et al. [30] determined the erosion threshold velocity in a vertical pipe with sudden contraction by conducting an extensive study on the effect of particle size, flow rate and direction of flow (up or down) on erosion rate for flow of water through a steel pipe contraction of 0.5. They used numerical models of the continuous phase and particle tracking for the prediction of flow field velocity and particle trajectory respectively. The results showed that erosion rates are highly dependent on particle sizes and flow inlet velocity. The flow direction has no effect on the pattern of flow and erosion rate except for larger particle diameters (400×10^{-6}m) and medium flow velocity (5m/s). This was said to be due to the gravitational effect on particle trajectory. They reported that the rate of erosion increases with increasing particle diameter and inlet flow velocity. The velocity below which negligible erosion rate is observed is termed the threshold velocity and was found to be 2m/s. Also, the region prone to significant erosion was found to be the inner tube surface of the tube sheet connecting the two pipes in the vicinity of the small pipe.

Badr et al. [31] investigated solid particle erosion of the entrance region linking the inlet header to the tube region under various erosion parameters like solid particle size and flow inlet velocity by simulating a real operating condition of an air cooled heat exchanger using commercial FLUENT software package. Air at flow velocity range 0.18-4.5m/s, the solid particle diameter of sizes in the range of 10-350μm are considered and the tube material is carbon steel. They predicted the flow pattern and erosion rate by solving the time-average governing equations for mass and momentum and proven erosion correlations sequentially. The results indicated that the tube entrance region is most prone to erosion. Erosion rates increase exponentially with increasing flow velocity and decreases with increasing particle size. They also reported that erosion is bound to take place whenever particles are present in the flow and also suggested the possibility of determining the threshold flow velocity at which erosion is considered negligible for a projected lifespan of the pipe material.

Habib et al. [29] investigated numerically the erosion of a protruded pipe situated at the point of sudden contraction and developed a correlation relating erosion rate to inlet velocity and protruded pipe geometry such as thickness and height. The essence of the protruded pipe was to reduce solid particle erosion in the critical erosion area. They considered a two-phase flow (liquid and solid) through a steel pipe with contraction ratio of 0.5. Their solution procedure involves the determination of the flow velocity vectors using the continuous phase model, solid particles motion using the Lagrangian particle-tracking model and erosion rates were determined by semi-empirical correlation. Penetration rates were calculated in mm/yr. The dependence of erosion rate on flow and geometric parameters such as the inlet velocity (3-10m/s), the particle size ($10\text{-}400\times10^{-6}$m), the contraction ratio (0.25-0.5) and geometry of the protruded pipe (height H = 2-5mm and width T = 1-5mm) were investigated. They found that particle diameter and inlet flow velocity variations are important determinants influencing erosions. It was also reported that increase in thickness and height of the embedded protruded pipe decreases erosion and penetration rates and this was attributed to increasing pathline curvature with thickness and height. The most eroded protruded pipe was 2mm thick and 3mm depth. Their results showed that the velocity below which significant erosion rate may not be observed was 3m/s. The authors also developed a correlation relating erosion rate to inlet velocity, thickness and height raised to powers 2, -0.25 and -0.2 respectively.

Bozzini et al. [49] studied the erosion-corrosion characteristics of a four–phase two immiscible-gas-solid particle multiphase flow in a 90° bend by studying the effects of void fraction, fluid velocity, and solid phase concentration using CFD capacity on FLUENT. They assumed that the liquid and gas phases modeled together with (volume of fluid) VOF model are perfectly homogeneous to deactivate the interactions at the phases interface. The k-ε and discrete phase model (DPM) were used to solve the flow turbulence and solid phase tracking respectively. These were coupled with erosion model and electromechanical aspect of corrosion mechanism to achieve a combined erosion-corrosion effects. They reported that flow velocity is the most important factor affecting erosion-corrosion phenomenon. Shirazi et al. [27] also developed a semi-empirical model that accounts for erosion parameters such as size, shape and density of solid particles and target material and fluid velocity, viscosity for the prediction of solid particle erosion in straight pipes sections, bends and tees made of mild steel and suitable for gas, liquid and gas-liquid mixture flows.

The problem of solid particle erosion downstream of a single orifice of diameter ratio 0.5 installed in a round pipe of internal diameter 50mm was studied by Nemitallah et al. [15].

They investigated the effects of solid particle sizes, flow velocity and pipe material on erosion rate by applying the Lagrangian approach using FLUENT. Their results showed that the locations with the highest erosion rates are the downstream primary recirculation zone and reattachment zones. The pipe section downstream the orifice is more susceptible to erosion. They reported that the rate of erosion increases with increasing flow velocity, decreasing particle sizes for both pipe materials of carbon steel and aluminum. Also, the total erosion reported for carbon steel is more than of aluminum because of the high ductility of the latter material.

Based on the above review, it is believed that no previous work has been carried out on erosion characteristics in a multiple orifice arrangements. The aim of this work is to study the effects of flow inlet velocity, particle size, orifice spacing and orifice sizes on the rate of solid particle erosion in the sections between the orifices and downstream the second orifice. The key steps taken to obtain results were flow modeling by solving time-averaged mass and momentum conservation equations, track the solid particle trajectories using the Lagrangian particle-tracking technique and estimation of erosion rates using semi-empirical erosion equations. Flow visualization and measurements were carried out with PIV and simple manometers for better understanding and validation of computational result.

CHAPTER 3

RESEARCH METHODOLOGY

The present study was carried out in two phases. The numerical analysis was carried out using FLUENT CFD software to investigate the erosion characteristics in a pipe equipped with one orifice and two orifices arranged in series at varying distances. The second part was based experimental measurements for flow characteristics downstream of the orifice with the aid of Particle Image Velocimetry (PIV).

3.1 Governing Equations and Computational Model

The prediction of flow field for steady state turbulent flow through an orifice involves solving the time-averaged steady state continuity and momentum equations and adopting the realizable k-ε turbulence two-layer model which suffices for single and multiphase flows. In order to study the erosion characteristics, Lagrangian particle tracking model was incorporated to predict the trajectory of particles for low-concentration one-way coupling simulation using Discrete Phase Model (DPM). The following assumptions were made:

- A Newtonian fluid
- An axisymmetric flow
- Constant temperature flow
- The solid particles do not interact with each other (low particle intensity)

3.1.1 Conservation of Mass

$$\frac{\partial}{\partial x_j}\left(\rho \bar{U_j}\right) = 0 \; ; j=1,\, 2 \tag{3-1}$$

3.1.2 Conservation of Momentum

$$\frac{\partial}{\partial x_j}\left(\rho \bar{U}_\iota \bar{U}_J\right) + \frac{\partial}{\partial x_j}\left(\rho \overline{u_\iota u_J}\right) = -\frac{\partial \mathrm{P}}{\partial x_j} + \frac{\partial}{\partial x_j}\left(\mu \frac{\partial U_i}{\partial x_j}\right) \tag{3-2}$$

where the stress tensor is represented as

$$\rho \overline{u_\iota u_J} = \left[\mu_{eff}\left(\frac{\partial \overline{U_\iota}}{\partial x_j} + \frac{\partial \overline{U_J}}{\partial x_j}\right)\right] - \frac{2}{3}\rho k \delta_{ij} \tag{3-3}$$

$\mu_{eff} = \mu_t + \mu$ is the effective viscosity and δ_{ij} is Kronecker delta (δ_{ij}= 1 for i = j and δ_{ij} = 0 for i$\neq$ j)

where turbulence viscosity is calculated by $\mu_t = \rho C_\mu \frac{k^2}{\varepsilon}$, C_μ is expressed as a variable function as $\frac{1}{A_0 + A_S \frac{kU^*}{\varepsilon}}$ where, $U^* = \sqrt{S_{ij}S_{ij} + \widetilde{\Omega_{\iota J}}\widetilde{\Omega_{\iota J}}}$

and $\widetilde{\Omega_{\iota J}} = \Omega_{ij} - 2\epsilon_{ijk}\omega_k$, $\Omega_{ij} = \overline{\Omega_{\iota J}} - \epsilon_{ijk}\omega_k$, $\overline{\Omega_{\iota J}}$ represents the mean-rate-of rotation tensor in the rotating reference frame with the angular velocity ω_k. A_0 and $A_S$are model constants and are expressed as A_0 = 4.04 and A_0= $\sqrt{6}\cos\phi$

where $\phi = \frac{1}{3}\cos^{-1}\sqrt{6}W$, $W = \frac{S_{ij}S_{jk}S_{ki}}{\tilde{S}^3}$, $\tilde{S} = \sqrt{S_{ij}S_{ij}}$, $S_{ij} = \frac{1}{2}\left(\frac{\partial u_j}{\partial x_i} + \frac{\partial u_i}{\partial x_j}\right)$

3.1.3 Conservation of Turbulence Kinetic Energy (k) and Dissipation Rate (ε)

$$\frac{\partial}{\partial x_j}\left(\rho \bar{U}_J k\right) = \frac{\partial}{\partial x_j}\left(\frac{\mu_{eff}}{\sigma_k}\frac{\partial \mathrm{k}}{\partial x_i}\right) + G_k - \rho\varepsilon \tag{3-4}$$

$$\frac{\partial}{\partial x_j}\left(\rho \bar{U}_J \varepsilon\right) = \frac{\partial}{\partial x_j}\left(\frac{\mu_{eff}}{\sigma_\varepsilon}\frac{\partial \varepsilon}{\partial x_i}\right) + \rho C_1 S\varepsilon - \rho C_2 \frac{\varepsilon^2}{k + \sqrt{\frac{\mu}{\rho}\varepsilon}} \tag{3-5}$$

where $G_k$represents turbulence kinetic energy production due to men velocity gradients and calculated as $$G_k = -\rho\overline{u_i u_j}\frac{\partial\overline{U_j}}{\partial x_i} \qquad (3\text{-}6)$$

σ_k and $\sigma_\varepsilon$are the effective Prandtl numbers for turbulence kinetic energy and its dissipation rate, respectively. C_1 is a function of k/ε as this shows that the model takes into cognizance the strain rate and streamline curvature which makes it suitable for this study and it is expressed as $\left[0.43, \frac{\eta}{\eta+5}\right]$, $\eta = S\frac{k}{\varepsilon}$, where S is related to deformation strain tensor by the relation $\sqrt{2S_{ij}S_{ij}}$, with S_{ij}= $0.5((\partial u_j/\partial x_i) - (\partial u_i/\partial x_j))$. The constants of the realizable k- ε model have specified values of $C_2 = 1.9$, $\sigma_k = 1.0$ and $\sigma_\varepsilon = 1.2$.

The realizable model has been found to provide the best performance of all the k- ε models especially for separated flows, boundary layer flows involving high pressure gradients, flows with complex flow structures. In the transport equations for k and ε for realizable model expressed above, the transport equation for k is similar to other k- ε models except for the model constants. The distinct features in the realizable model proposed by Shih et al. [50] are

- the introduction of new eddy-viscosity relation with a variable C_μ as suggested by Reynolds [51] which is sensitive to mean flow, k and ε
- new model equation for ε based on the dynamic equation of mean-square vorticity fluctuation has the generation term (second term on the right hand side) independent of production of k and the destruction term (last term on the RHS) not having singular value (differentiating it from the other k- ε models with G_k).

3.1.4 Pressure Difference

The flow of single phase fluid through a thin orifice fixed in a pipe of flow area *A* involves reversible contraction with a negligible mechanical loss to a downstream point of the minimum flow area A_c, known as vena contracta. This is followed by a process of irreversible expansion in which the fluid re-attaches to the pipe wall. Assuming that the fluid has a constant density throughout the flow and applying Bernoulli's equation between a point 5D upstream and vena contracta, the pressure difference ΔP across the orifice can be expressed in terms of density ρ, flow velocity V, area ratio $\beta = (d/D)^2$ and contraction coefficient $\beta_c = A_c/A\beta$ as

$$\Delta P = \frac{\rho V^2}{2}\left[\left(\frac{1}{\beta\beta_c} - 1\right)\right]^2 \tag{3-7}$$

Lin [52] suggested a relationship between ΔP and Coefficient of discharge C_d as,

$$\Delta P = \frac{\rho V^2}{2}\left[\left(\frac{1}{\beta}\right)^2 - 1\right]\frac{1}{C_d} \tag{3-8}$$

An expression for the contraction coefficient β_c in terms of C_d and β can be formed from Eqns. (3-7) and (3-8) as

$$\beta c = \frac{1}{\beta + \left(\sqrt{1-\beta^2}\right)/C_d} \tag{3-9}$$

The expression for contraction coefficient in Eqn. (3-9) can be compared to the common expression for β_c below given by [1] as,

$$\beta c = \frac{1}{[0.639(1-\beta)^{0.5}+1]} \tag{3-10}$$

3.1.5 Lagrangian Particle –Tracking Model

Two important parameters related to solid particle needed for the calculation of erosion rates are impact angle and impact velocity. These values are deduced from the trajectory of the particles across the whole length of the pipe form introduction at the inlet to exit at outlet. Some assumptions made based on the low volume concentration of the particles at 2% by volume are that the only effective collision occurred between the particles and the wall. Also, the particles are non-interacting with each another and the effect of the motion of particles on the continuous phase is negligible as suggested by Benchaita et al. [53]. Also, the particle's impact velocity and impact angle is dependent on the mean flow but independent of the turbulence effect that exists in the flow. This is based on the report of Postletwaite and Nesic [54] that erosion due to random motion downstream a sudden expansion is relatively negligible in magnitude to erosion due to impingement. Based on Newton's Second law and the influence of hydrodynamic forces, the motion of particles can be expressed as

$$\frac{du_p}{dt} = F_D\left(u - u_p\right) + g(\rho_p - \rho)/\rho_p + F_{vm} + F_{pg} + F_{sl} \qquad (3\text{-}11)$$

The term on the LHS stands for the acceleration term. The first term on the RHS is the drag force term where $F_D = 3C_D\mu R_{ep}/4\rho_p D_p^2$. Expressions for particle's Reynolds number and drag coefficient are given as

$$R_{ep} = \frac{\rho D_p |u_p - u|}{\mu} \qquad (3\text{-}12)$$

$$C_D = a_1 + \frac{a_3}{R_{ep}} + \frac{a_3}{R^2{}_{ep}} \qquad (3\text{-}13)$$

The values of the constants a_1, $a_{2,}$ and a_3 in Eq. (3-14) are given by Morsi and Alexander [55] for smooth spherical particles over a wide range of Reynolds number.

The second term is the buoyancy term while the force needed to accelerate the continuous flow around any particle is represented by the third term F_{vm} known as virtual mass force expressed as

$$F_{vm} = \frac{1}{2}\frac{\rho}{\rho_p}\frac{d}{dt}\left(u - u_p\right) \tag{3-14}$$

F_{pg} represents the pressure force which defines the influence of presence gradient on every control volume of the flow domain and can be expressed as $\left(\rho/\rho_p\right)\nabla p$. The last term in the equation F_{sl} represents Saffman lift force which defines force due to shear layer. The drag force and buoyancy force are of a higher of magnitude and of more relevance to discrete phases than pressure gradient, virtual mass and Saffman lift force which were neglected.

Integration of Eq. (3-11) over time steps for each particle gives the velocity at every point on the trajectory. Trajectory of the particle can be predicted from the integration of Eq. (3-15)

$$\frac{dr}{dt} = u_p \;, \underline{r} \text{ represents position vector} \tag{3-15}$$

3.1.6 Erosion Calculations

The erosion ratio depends majorly on the particle's characteristics like shape, material property, size, impact speed and angle, and material property of the pipe. Erosion ratio is generally defined as the ratio of mass eroded from the pipe to mass of particles impinging on it and it is represented by Mclaury [56] as

$$W = QF_sF_\theta V^n \ (kg/kg) \tag{3-16}$$

where Q, F_s, F_θ, V and n are empirical constant, particle shape coefficient, impact angle function, particle impinging speed and empirical coefficient respectively. For carbon steel, the value of Q is $15.59 \times (120)^{-0.50} \times 10^{-7}$ as specified by [57]. The values for n and F_s used are 1.73 and 0.2 respectively ass obtained from [58]. The impact angle function varies with impact angle and can be expressed as

$$F_\theta = \begin{cases} a\theta^2 + b\theta & for\ \theta < \alpha \\ xcos^2\theta \sin w\theta + ysin^2\theta + z & for\ \theta > \alpha \end{cases} \tag{3-17}$$

a, b, x, y, z and α are empirical constants and they vary with target materials. The values of these constants for carbon steel used in this work are (-33.4, 17.9 1.239, -0.1192, 1.0, 2.167 and Π/2) respectively [57]

Another important erosion parameter which describes the depth to which erosion has taken place at different points on the wall is the local penetration rate. The local penetration rate based on average yearly rate P_n, measured in (mm/year), as represented by Eq. (3-14) is;

$$P_n = 31.536\, X\, 10^6 \dot{s}/(\rho_m Ai\,)\, E_{lc} \tag{3-18}$$

Where E_{lc} is the local erosion rate (mg/g), Ai is the impingement area (m^2), $\dot{s}$ is sand rate (kg/s), and ρ_m is the density of target material (kg/m^3).

3.1.7 Boundary Conditions and Solution Methodology

The inlet condition is set as velocity inlet boundary condition, the pipe and orifice walls are set as walls such that the no-slip and non-penetration condition applies while pressure outlet condition is applied at the exit to cater for possible backflow that may occur for the flow domain in Fig. 1. An axis boundary condition is imposed on the centerline and as such normal gradient of all properties and radial velocity are zero along it. The flow is assumed as axisymmetric so that it can be treated as two-dimensional flow. The turbulence length scale and turbulent intensity ($\sqrt{k}/\bar{U}$) are set as internal pipe diameter and 2% respectively to specify inlet conditions for turbulent kinetic energy and dissipation rate. Their values in the flow domain are controlled by the governing equations for turbulence model.

In the case of boundary conditions for the erosion model, the inlet is set as surface injections while the outlet is specified as escape which means trajectory calculation for every particle is terminated once crossed. Particles with no impacts on the walls at locations of zero velocities trapped in circulation zones upstream and downstream also have their trajectory computation terminated. Particles impact velocities after every impingement is dependent on the type of wall being considered. To account for exchange of momentum between the particle and the wall, reflect boundary condition is specified at the wall with 0.9 normal coefficient of restitution. Normal coefficient of restitution specifies the portion of normal momentum retained by the impacting particles after impingement.

The equations governing the conservation of mass and momentum together with turbulence kinetic energy and dissipation rate are solved simultaneously over discretized volumes using the finite volume approach resulting into system of discretized (algebraic) equations which are solved using double precision, segregated, implicit scheme inherent in FLUENT 6.3 after subjecting every control volume to the appropriate boundary conditions. The Realizable k-ε model with SIMPLE and PRESTO second order upwind discretization schemes for pressure-velocity coupling and convection- diffusion respectively. The convergence criterion is set such that solution is reached when the residuals of mass continuity, velocity components, turbulence kinetic energy and dissipation rates are unchanging at mass continuity equation < 10^{-13} and the mass-weighted average of pressure and velocity at 5 pipe diameters upstream and downstream and orifice face is monitored as done by [8]. The geometry was discretized to achieve fine grids at the walls and regions around the orifice for better prediction of wall parameters and abrupt change in velocity respectively as shown in Fig. 2.

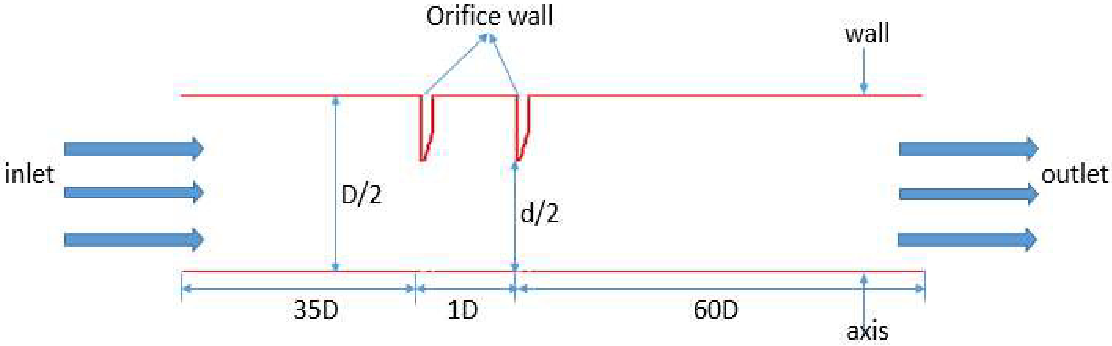

Figure 1 Schematics of flow domain around the orifice

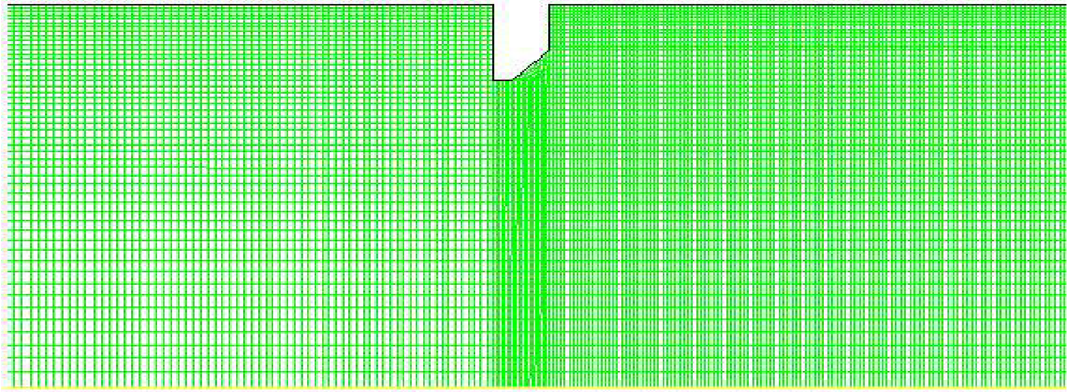

Figure 2 Mesh around the orifice

3.1.8 Grid Independence Test

In order to show the independence of the solution on control volume mesh, grid independence test was carried out using four different grid densities with 57,310, 129,858**,** 230,500 cells. A comparison of the centerline velocity magnitude profiles among the grid densities at inlet velocity of 1m/s and $D_r = 0.63$ is shown in Fig. 3. It can be seen that an almost identical profile was observed for cell the three mesh densities but the difference between 129,858 and 230,500 cells is negligibly small. This implies that more grid refinement will have a negligible effect on the solution since the influence of grid refinement is less than 2%. The 129,858 cell was chosen for accuracy and effective computational time. Furthermore, the numerical meshes adopted for other D_r and configurations were selected after subjecting various grid densities to grid independence test.

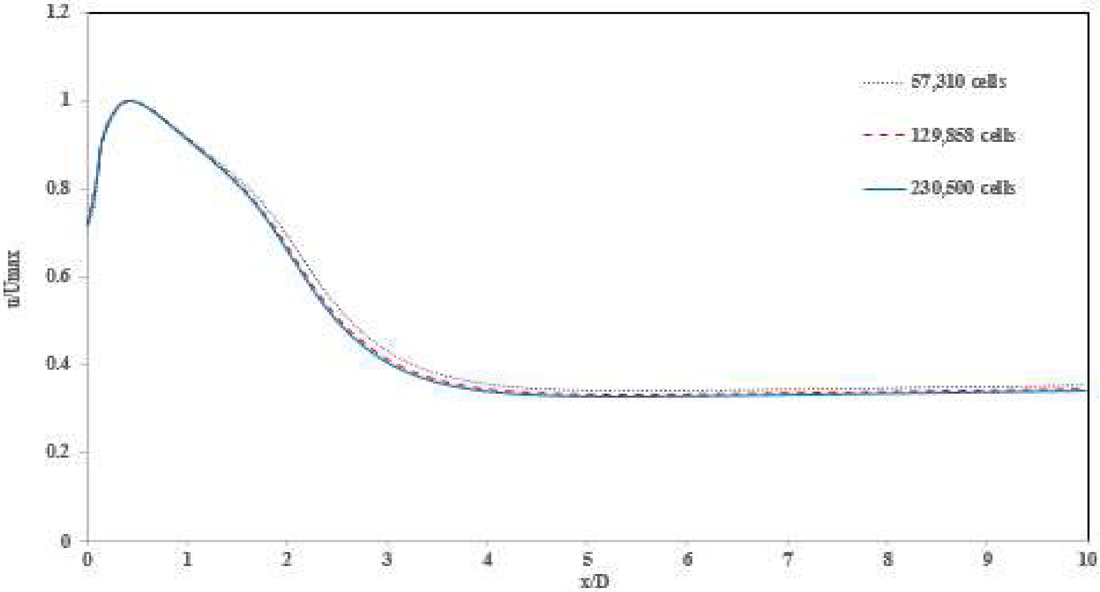

Figure 3 Comparison of downstream centerline variation of axial velocity for different grids at inlet velocity=2m/s

3.1.9 Model Validation

Figure 4. shows validation of the present computational solution with the work of Eiamsa-ard et al.[34] using the centerline velocity magnitude profile. The validation was done by modeling with FLUENT the flow of water at Reynolds number = 1.84×10^4 through an orifice with a diameter ratio of 0.5 and thickness 3.2mm positioned in a circular pipe of internal diameter 25.4mm. The figure depicts a very small difference between the profiles which implies the correctness of the present model.

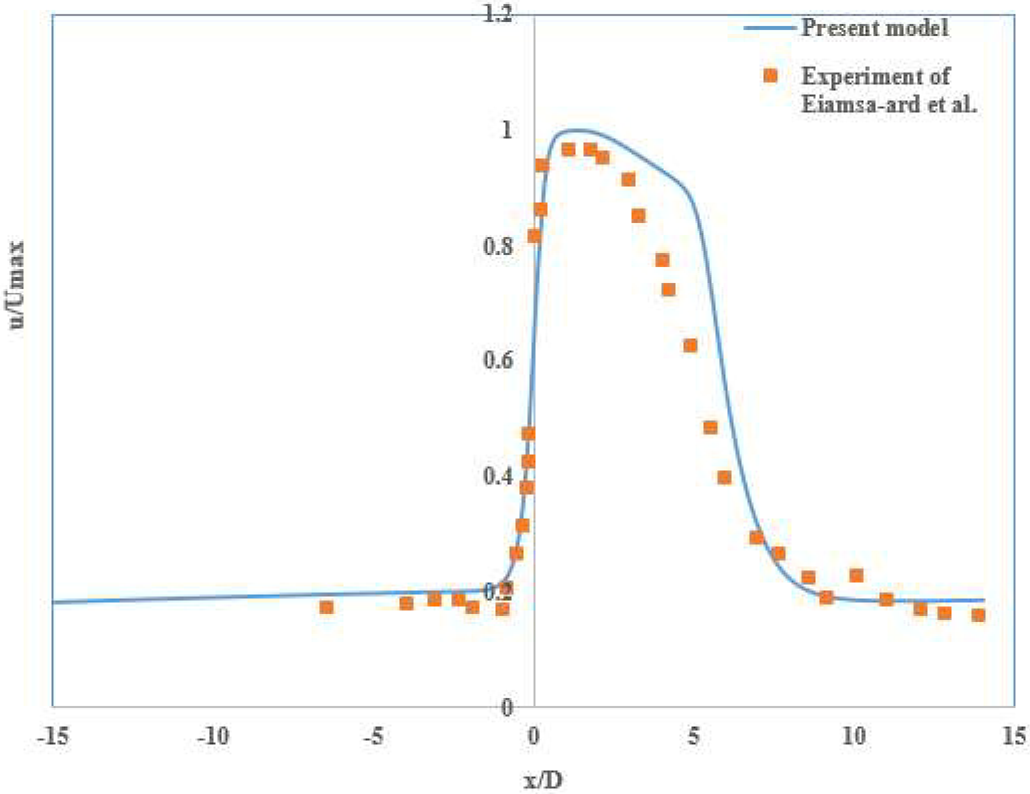

Figure 4 Comparison between the numerical result from the present model and the experimental data of Eiamsa-ard et al. [15]

3.2 Experimental Test Rig and Measurements

The schematic of the flow loop used in carrying out experiments for single phase orifice flows is represented by Fig. 5. The line connecting different components in the flow loop is mostly made of acrylic pipe with an inner diameter of 25.4mm and an outside diameter of 38.3mm. Some portions are made of flexible hose to aid adjustment during orifice replacement. A closed flow loop was ensured with negligible leakage and the flow direction is anticlockwise. A tank of 100 liters serves as water storage and a medium of introducing seeding particle into the flow. The centrifugal pump drives water from the tank through the loop. Flow rate was controlled by the rotational speed of the pump and gate valve installed on the discharge line of the pump.

A turbine flow meter with digital display of specifications SN:503399, MODEL: FTB791 and K/F:2562ppg in conjunction with a gap meter with MODEL: FL-1504A and SN:0100100158847 installed ahead of the straight pipe section upstream the orifice inlet was used to measure the flow rate. The total length of the straight pipe section upstream is more than 60D so as to ensure that the flow assumes fully developed condition. The key section of this set up is the test section labeled (5) because it contains the orifice/s and serves as the main focus for the PIV measurement. The test section as shown in Figure 6 was designed in a way to accommodate multiple orifices and allow flexibility in a variation of the distance between the orifices. The parts were machined by boring an inch diameter hole in a block glass block prism of rectangular cross section. The machining work was finished with honing the inner surface to reduce the diffraction of laser sheets.

The test section consists of parts of 4D length at both upstream and downstream sections of the orifice for single orifice flow and additional parts of 2D and 1D lengths which serve as orifice spacing for multiple orifice set up as shown in Fig.7. O-rings are fitted in between these sections to prevent leakages. The orifice was machined to ANSI standard for D_r = 0.5 and 0.63 with dimensions shown in Fig.8. To ensure uniformity and avoid misalignment which might lead to leakages, the orifices were made in the form of squares of 3mm thickness and matching size with other parts. Holes of sizes M3 were bored at the four edges of the orifices and other parts of the test section for the fastening purpose. Four threaded rods of diameter 3 mm were slotted through the length of the test section and tightened with nuts at flanges on the setup. Other fasteners employed are bolts and nuts that were used to fasten the flanges on both 4D upstream and downstream parts of the test section to the flanges on the test rig.

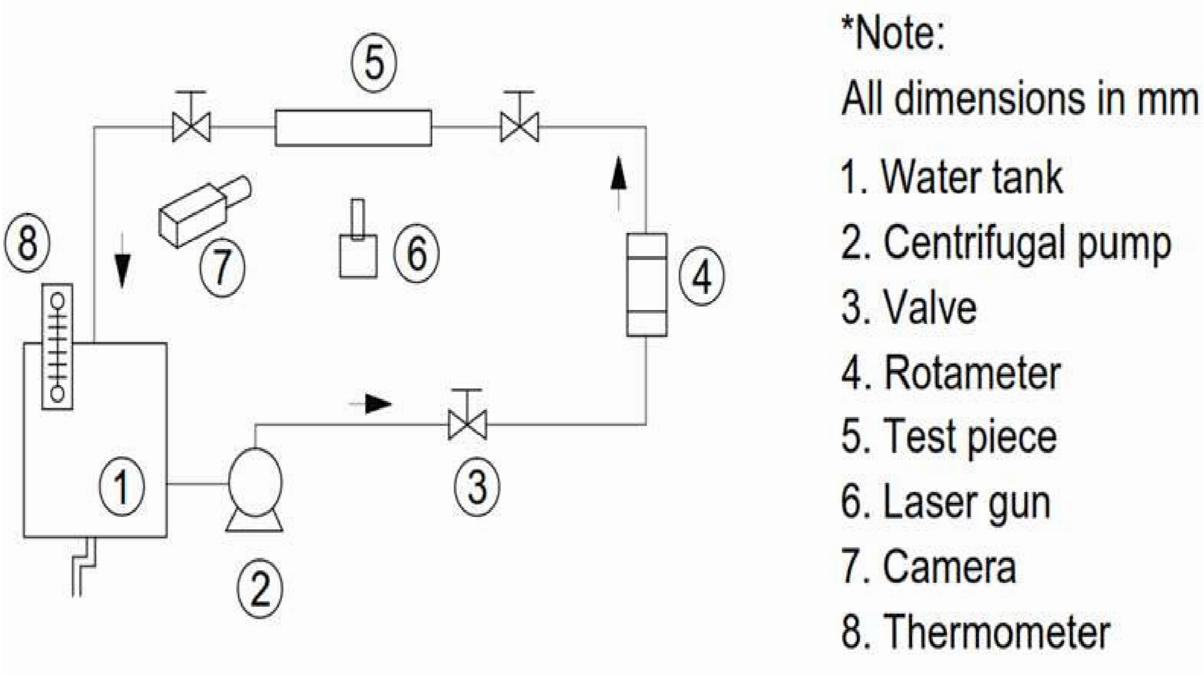

Figure 5 Flow loop schematics

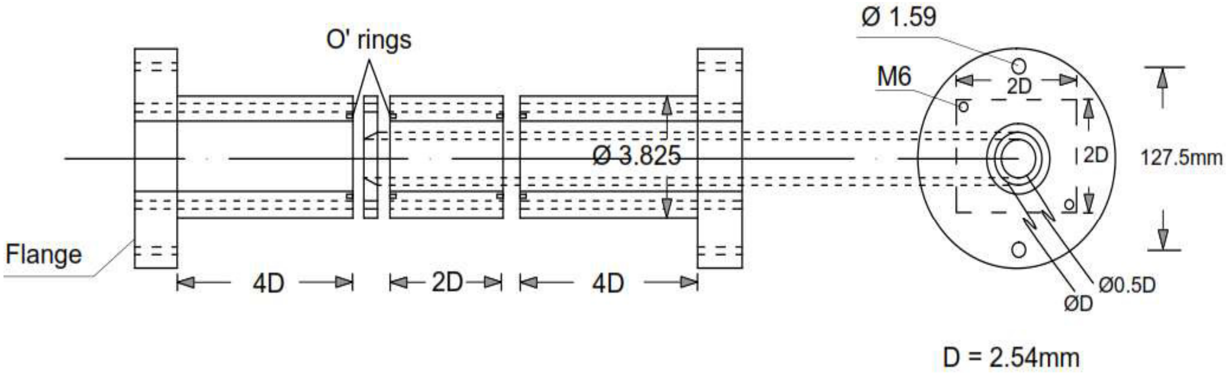

Figure 6 Sectional view of test section

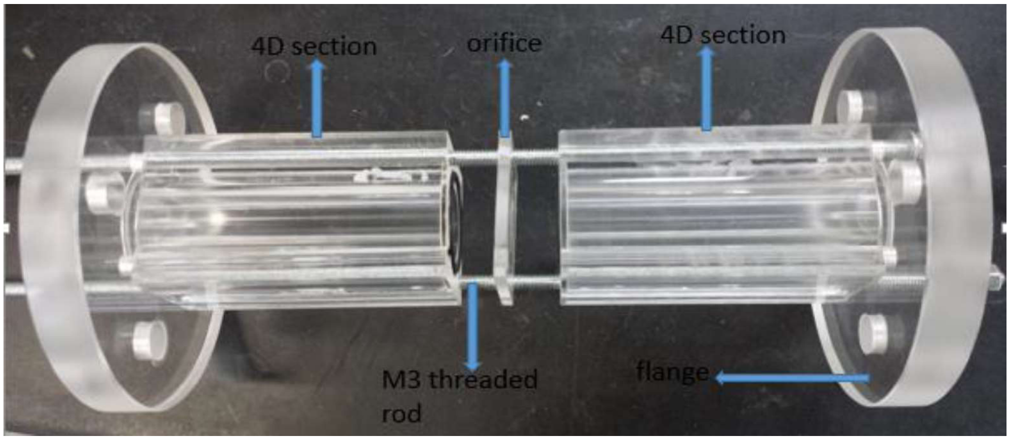

(a)

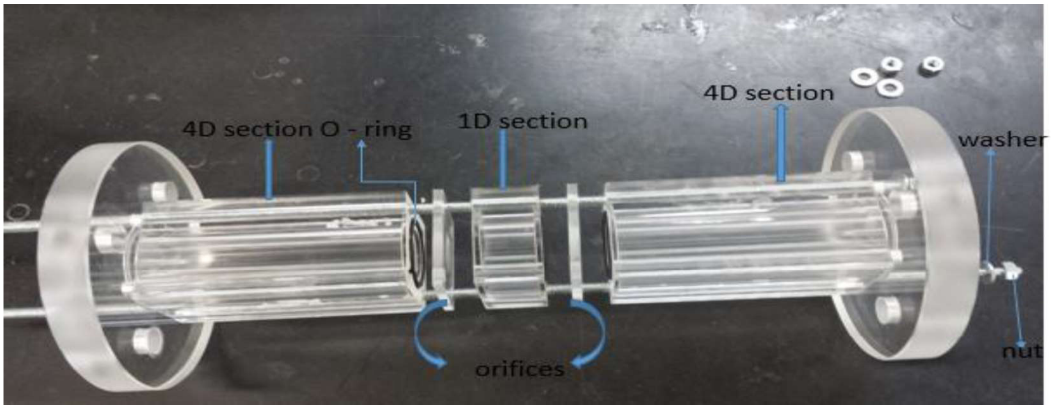

(b)

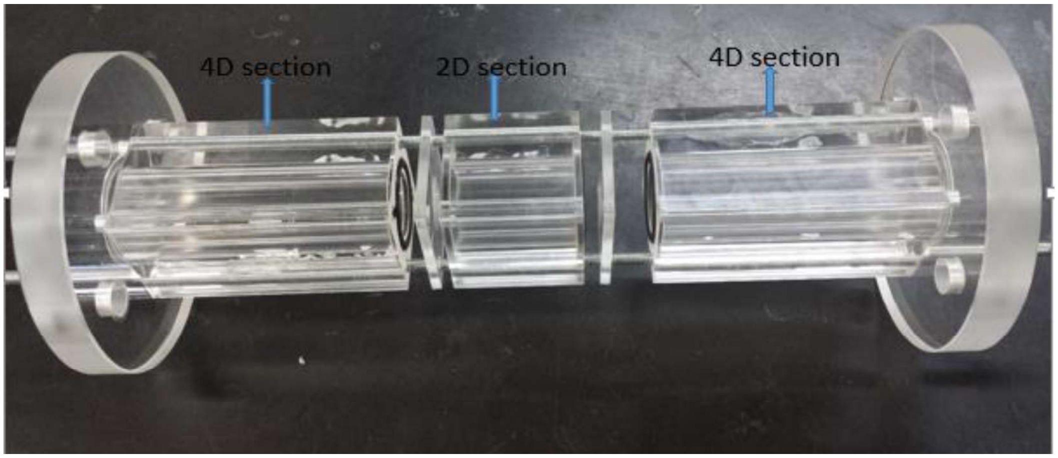

(c)

Figure 7 Figure 3-7 Assembly of test sections of three different configurations (a) Single orifice, (b) Double orifice one pipe diameter (1D) orifice spacing, (c) Double orifice two pipe diameter (2D) orifice spacing

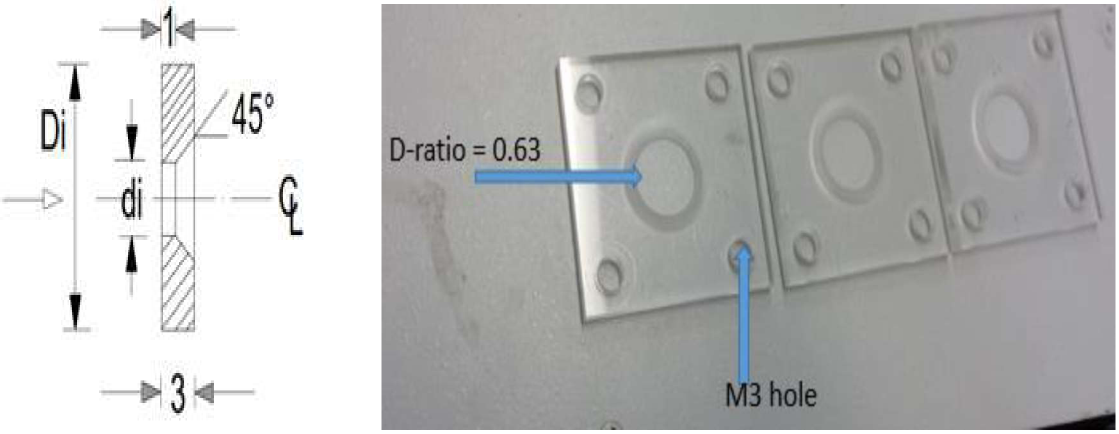

(a) (b)

Figure 8 ANSI standard orifice (a) sectional drawing (b) manufactured pieces

A section of the straight pipe downstream is made of flexible hose of the inner diameter of 25.4mm to aid easy adjustment during assembling and disassembling of the test section from the setup.

A 2D2C PIV measuring technique was employed in measuring flow velocity in the downstream section of the orifice. The light source which is a laser was situated such that it illuminate the test section from below while the camera was placed at right angles to the laser, to capture images of the seeded flow fields from the front. The squared surface of the test section helps in minimizing optical distortion during capturing of images. A more effective method is to place the test section with a rectangular basin containing the same fluid as that flowing through the pipe. This study was focused on the downstream section of the orifice and an axial length of 2D – 2.5D was considered due to the limitation of the width of light sheet by the vertical distance of separation between the light source and test section.

Particle Image Velocimetry (PIV) is a type of quantitative optical measuring technique that is non-intrusive and provides an instantaneous measure of flow field characteristics. Its non-intrusive approach gives the technique an edge over other probing optical techniques like Laser Doppler Anemometry (LDA), as PIV techniques require no probing. This eliminates errors in measurements due to disturbances introduced by inserting probes in the flow regime which makes PIV a more appropriate technique in studies of shock waves, boundary layer flows etc. PIV produces a high spatial resolution of flow field which also makes it highly relevant in the study of spatial structures in unsteady flows [59]. Conventional methods of velocity measurements, like pitot tube and Hot Wire Anemometry (HWA), provide single point velocity measurements while PIV has the capability of determining whole field measurement. As the name implies, the main flow properties measured by PIV is instantaneous velocity. Other properties like vorticity, shear stress which are in the form of derivatives of velocity can be determined subsequently.

The PIV measuring technique is sometimes referred to as an indirect velocity measurement technique because the actual velocity determined is that of the seeding particles from which the velocity of the flow field is implied. Earlier PIV techniques had the capacity of determining two components of velocity in a two-dimensional plane. A comprehensive information on the development of PIV technique in terms of operational procedure and advancement in equipment can be found in [13], [60]. Velocity measurements are to be read in three components in order to satisfy the curiosity of researchers. Implementing single point measurement techniques like LDA and HWA in their 3D modified forms to determine the 3-components of velocity can be tedious and time expensive for large volume and non-stationary flows. In lieu of these challenges, different velocimetry techniques have been designed and they may be classified using the (l-m-n) method of [61].

In this terminology, l = 1, 2, 3 stands for velocity components; m = 0, 1, 2, 3 signifies space dimensions and n = 0, 1 specifies time conditions of velocity measurements either single instant or complete time. Table 1 indicates various velocimetry techniques and their class based on the (l-m-n) method. The 2D2C PIV technique which was adopted for this study has been defined as (2, 2, 0) by the table i.e. velocity vector measurement is in two components, two dimensions at every instant. Tomographic PIV technique yields a complete data of velocity vector measured in the entire domain as a time-dependent function i.e. (3, 3, 1).

Figure 9 represents a 2D2C PIV setup and general measuring techniques. The fundamental materials and equipment needed for a basic PIV measurement are seeding/tracer particles, light source, light sheet optics, digital camera, a computer system installed with the PIV software. The flow is seeded with adequate seeding particle appropriate for PIV analysis. Light sheet from a combination of light sources and light sheet optics beamed on the region of interest illuminates the seeded flow. Light reflected from the region of interest is captured by a digital camera as image pairs with a pre-defined time interval (Δt) of separation between each image of the pair. The digital images obtained are then analyzed with PIV software.

Calibration images are captured separately and designated as such for the purpose of converting pixel measurement to object measurement. Individual image 1 and 2 of an image pair is divided into desirable Interrogation Areas (IA) with fewer particles to facilitate cross correlation process.

Table 1 Classification of Optical Velocimetry techniques in terms of velocity components, space and time

Technique	Velocity component	Space	Time	Classification	No of cameras
	l	m	n	(l, m, n)	
LDA	1(u)	0	1	(1, 0, 1)	1
3-D LDA	3(u, v, w)	0	1	(3, 0, 1)	2
Planar PIV	2(u, v)	2(x, y)	0	(2, 2, 0)	1
Stereoscopic PIV	3(u, v, w)	2(x, y)	0	(3, 2, 0)	2
High Speed PIV	3(u, v, w)	2(x, y)	1	(3, 2, 1)	2
Double-pulsed Holographic PIV	3(u, v, w)	3(x, y, z)	0	(3, 3, 0)	2
Tomographic PIV	3(u, v, w)	3(x, y, z)	1	(3, 3, 1)	multiple

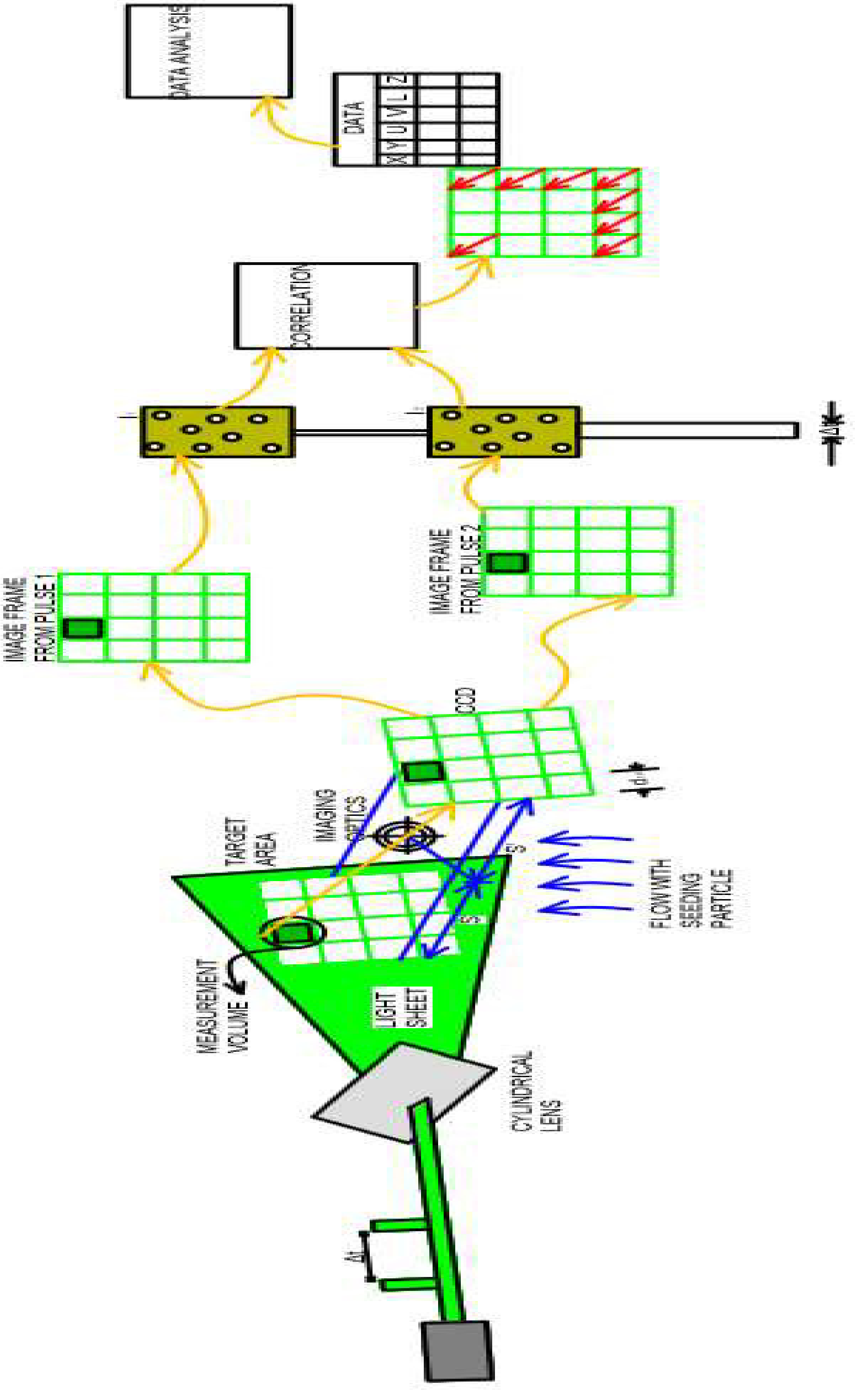

Figure 9 2D2C PIV set-up and general measuring technique

Cross correlation literally means finding the particle pattern with best match by placing IA from image 2 on IA from image 1 of a particular image pair. This produces a signal peak displacement ($\Delta\bar{x}$) which represents resultant pixel displacement. A velocity vector can be calculated for this IA using Eq. (3-19). A repetition of these steps for other IAs yields a vector map.

$$\bar{U} = \lim_{\Delta t \to 0} \frac{\Delta\bar{x}}{\Delta t} \tag{3-19}$$

Subsequently, we take a brief look at the theoretical background in relation to the procedures implemented in conducting the experiments for this study. Every procedural step will be discussed in consonance with materials and apparatuses that constitute the 2D2C PIV set-up.

3.2.1 Seeding Particle

As earlier stated, the velocity measured by PIV is that of the seeding particles. So, adequate knowledge of the relationship that exists between the fluid and tracer particle is necessary for verifying the accuracy of PIV experiments. Features of ideal particles suitable for a PIV analysis are:

- there must be negligible difference in the densities of fluid and seeding particles
- particles must be easily visible
- they should neither interact with each other nor influence continuous phase flow
- they should be chemically inactive
- they should have diameter d_p close to the light sheet wavelength λ.

Based on the features stated above, compromises such as like better reflection of light which is relevant in signal-to-noise-ratio (SNR) (large tracer particles) and the need for tracer particles to follow the flow field (small light particles) sets in [62]. The primary source of error is the prominence of gravity due to the large discrepancy in the densities of the tracer particles and the continuous phase which implies that proper selection of tracer particles that matches in density with continuous phase is very important. Raffel et al. [13] represented the velocity lag between a particle and an accelerating fluid by

$$\overline{U_s} = \overline{U_p} - \overline{U} = {D_p}^2 \frac{(\rho_p - \rho)}{18\mu} \bar{a} \tag{3-20}$$

where $\overline{U_s}$= velocity lag, $\overline{U_p}$= velocity of particle, D_p= particle diameter, ρ_p= particle density, $\overline{U}$= local fluid velocity, $\bar{a}$= fluid acceleration, ρ = fluid density and μ = fluid dynamic viscosity. According to Li et. al. [59], proper selection of seeding particles is a more efficient and economical method of increasing the image density than increasing lighting power or particle sizes and concentration. Numerous seeding particles are available that are suitable for liquid flows. The method of introduction of seeding particles to the continuous flow is another important process that needs to be done carefully. A homogeneous mixture of particle and fluid is required for a complete flow field analysis by PIV technique [63]. Unlike aerodynamic, liquids are easily seeded by homogeneous mixing to achieve desired image contrast Polyamide was selected as seeding particle due to its relative closeness in density (1.03g/cm^3) to the working fluid and its availability for use.

3.2.2 Light Sources

PIV measuring technique require a light source to illuminate flow region of interest from which low images are captured. The suitable light sheet for PIV measurement should have a top-hat shape, be collimated, and have minimum divergence. The thickness of light sheets can be controlled and minimum light sheet thickness allowed for an application can be calculated using Equation (3-21).

$$\delta m = 4f\lambda/\Pi d_{\circ} \text{ provided Rayleigh length} > \text{focal length} \tag{3-21}$$

Main sources of light sheets are white light, LED light, and laser light. The suitability of LED illumination for planar PIV experiments in water and air media was investigated by [64]. Laser lights are the most used light sources for PIV measurement techniques. Laser light sources produce high energy density monochromatic light with strong brightness and almost constant converging thickness that enables recording of tracer particles devoid of chromatic aberration when combined with sheet optics of positive and cylindrical lenses [13], [59].

Laser light sources used for PIV analysis can be grouped into three namely continuous wave (CW), solid-state or pulsating lasers and semiconductor lasers. Continuous wave laser produces a good beam of low power light within short intervals and accompanied by little amount of heat, solid-state laser produces high power light with high frequency which makes them suitable for high-speed flows, but are expensive and difficult to set-up with synchronizers, and semiconductor lasers (Nd: YLF) are used for small scale experiments as they produce lights with energy lower than solid-state lasers. The laser used for this study was Continuous Wave (CW) Raypower2000 laser supplied by Dantec Dynamics with specifications stated in Table 2.

Table 2 Laser specifications

Specifications	Raypower 2000
Lasing medium	Gas
Wavelength	532 ± 1 nm
Output power	>2000mW
Operating mode	CW
Transverse mode	Near TEM00
Beam diameter at the aperture	3.0nm
Polarization ratio	>100:1
Operating temperature	10-35^{o}C
Mains supply	100-240VAC 3A max, 50-60Hz
TTL modulation frequency	max 10kHz

3.2.3 Camera

Due to the weak light reflected by seeding particles, cameras with large apertures and high-quality lenses are required for PIV measuring techniques [59]. Over the years, there has been an upgrade from photography recording cameras to digital recording cameras. Digital recording cameras contain charged couple device (CCD) arrays with large pixels that converts light into electric charges which gives the advantages of avoiding photograph processing, obtaining instant images of flow incidents and allowing review of incidences [13]. The experiments carried out in this study were done with Dantec Speedsense Camera 9040 and lens with specifications shown in Tables 3 & 4 respectively.

3.2.4 Particle Imaging

Two important phenomena which affect the images of particles when carrying out PIV analysis are refraction through curved surfaces and diffraction limited imaging. Differing refractive indices of water, glass and air and curvature of interfaces causes distortion of images of seeding particles in terms of shapes and location when viewed from outside. To minimize the effects of optical distortion, several solutions has been proposed such as machining the exterior curved surface of the circular tubes to rectangular shapes [65]. They also proposed filling the circular pipe with a fluid that has a refractive index close to that of the pipe material, but Lowe & Kutt [66] suggested that these methods limit the extent of experiments. Most studies adopted the method of situating the cylindrical pipe in a rectangular tank filled with the same fluid running through the pipe. Figure 10 illustrates the distortion process in relation to pipe thickness. Hidden regions and multiple images appear in the inner wall regions in pipes with thin radial ratio, but thicker pipes attenuate the power of light rays.

Table 3 PIV Camera Specification

Specifications	SpeedsenseCamera 9040
Sensor type	CCD progressive scan monochrome
Chip size (mm)	18.77 × 13.8
Resolution (pixels)	1632 × 1200
Pixel size (µm)	11.5
Bit depth	8, 12, 14
Maximum exposure time (µs)	2
Fps (full frame)	1016/508

Table 4 PIV Lens Specification

Specifications	Nikon AF Micro Nikkor 60mm f/2.8D
Focal length (mm)	60
f-number	2.8-32
Distance scale (m)	0.219 - ∞

The radial ratio is the ratio of outer pipe radius to inner pipe radius. Raffel et al. [13] gave a mathematical representation of diffraction limiting diameter (D_{diff}) in terms of light wavelength (λ), magnififcation (M) and camera's f-number ($f_{\#}$) defined as ratio of focal length to diameter of aperture, as

$$D_{diff} = 2.44(M+1)f_{\#}\lambda \tag{3-22}$$

3.2.5 Correlations and Data Processing

An important step in PIV technique is image evaluation by correlation methods. To perform any of the correlation methods, the image map is first discretized into interrogation areas (IA). The common sizes used are 16×16 pixels or 32×32 pixels and the choice of size depends on desired accuracy, resolution and quality of the image maps. To achieve optimum results in PIV, the number of particles per IA should be in the range 8-25.The peak displacement vector of each IA is determined through statistical techniques realized by either digitally performed Fourier algorithms or Optical techniques. Such statistical techniques are important since visualization of matching pairs is quite impossible in PIV analysis. In similitude to signal analysis, statistical evaluation applies correlation theory to determine the displacement between two-dimensional images with time interval [13].

Correlation in this domain is of order $\Theta(N^4)$ which implies a quadratic increase in multiplication per correlation value in relative proportion to IA. Fast Fourier Transform (FFT) built on frequency domain provides a more efficient, faster and less computational correlation platform. Two-dimensional FFT has order of operation $\Theta(N^2 \log_2 N)$ and it capitalizes on the symmetry and anti-symmetry of the real and imaginary parts of functions to half computation time. Raffel et al. [13] provided a broad explanation of different correlation applications.

$$R_{II}(\bar{s}, \bar{x}, \overline{\mathrm{D}}) = \frac{1}{A} \sum_{j=1}^{N} V_0(\bar{X}_\imath)\, V_0'\left(\bar{X}_\jmath + \bar{D}\right) \int_A \tau\left(\bar{x} - \bar{x}_\imath - \bar{d}\right) \tau\left(\bar{x} - \bar{x}_\imath + \bar{s} - \bar{d}\right) \quad (3\text{-}23)$$

$\bar{s}$ and A have been introduced to represent the separation vector and the interrogation area respectively.

A brief look at the mathematical representation of cross-correlation for image pairs. The cross-correlation of the two interrogation areas can be written as

$$R_{II}(\bar{s}, \bar{x}, \overline{\mathrm{D}}) = \frac{1}{A} \sum_{j=1}^{N} V_0(\bar{X}_\imath)\, V_0'\left(\bar{X}_\jmath + \bar{D}\right) \int_A \tau\left(\bar{x} - \bar{x}_\imath - \bar{d}\right) \tau\left(\bar{x} - \bar{x}_\imath + \bar{s} - \bar{d}\right) \quad (3\text{-}24)$$

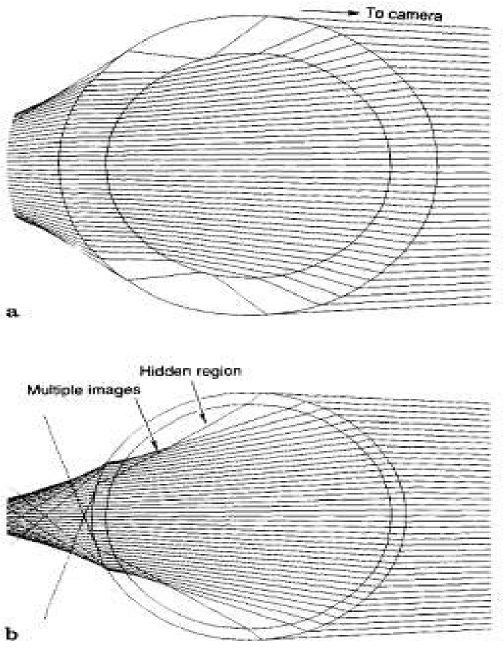

Figure 10 Distortion of light rays due to curved surface and refraction for radial ratios (a) 1.33 (b) 1.1 (adapted from Lowe & Kutt [66])

If we make a differentiation of the terms representing the correlation of particle images with themselves (i = j) from the terms representing the correlation of a particle image with a different particle image (i ≠ j), then Equation (3-24) can be represented by

$$R_{II}(\bar{s},\bar{x},\bar{\mathrm{D}}) = R_C(\bar{s},\bar{x},\bar{\mathrm{D}}) + R_F(\bar{s},\bar{x},\bar{\mathrm{D}}) + R_D(\bar{s},\bar{x},\bar{\mathrm{D}}) \qquad (3\text{-}25)$$

Where $R_C(\bar{s},\bar{x},\bar{\mathrm{D}})$is the convolution of the mean intensities and $R_F(\bar{s},\bar{x},\bar{\mathrm{D}})$gives a fluctuating noise component, both these components relate to i ≠ j. The cross-correlation analysis is based on $R_D(\bar{s},\bar{x},\bar{\mathrm{D}})$, which gives the convolution of matching particle pairs between the first and second exposures (i = j) and can be written as

$$R_D(\bar{s},\bar{x},\bar{\mathrm{D}}) = R_\tau(\bar{s} - \bar{d})\sum_{i=1}^{N} V_0(\bar{X_\iota})\, V_0'(\bar{X_J} + \bar{D}) \qquad (3\text{-}26)$$

$R_\tau(\bar{s} - \bar{d})$ represents the correlation of an image of a particle. For a better understanding, refer to Raffel et al. [13].

3.2.6 Application

As stated earlier, image analysis involves dividing into smaller uniform IA followed by applying the cross-correlation algorithm. In order to achieve optimized results, the following rules have to be followed,

- A minimum of number of particles (15) should be present in an IA to achieve at least 90% detection of valid particles
- The relation between the size of IA (w) and maximum velocity gradient is represented by

  $$\left|\frac{\partial u}{\partial x}\right| \Delta t < \frac{d_p}{w}$$

- One-quarter rule must be adhered to minimize loss of data. The quarter rule is that the maximum displacement of particles between image pairs should be ¼ of the IA size.
- The time sequence between consecutive pulses of the laser must be adjusted such that it is not lesser than the equivalence of 8 pixels in order to prevent a reduction in velocity dynamic range.

Once the size of IA and time delay is selected (typically sizing's of 32 × 32 and 64 × 64 pix^2) the light intensity distribution of each pixel in an interrogation window is cross-correlated between image exposures. The displacement vector of a particle is derived as the displacement between the correlation peak and the center of IA. The normalized correlation function (Equation 3-26) is based on spatial domain and will involve a long processing time as stated earlier. The temporal domain is exploited to overcome this setback based on the correlation theorem that the cross correlation of two functions is equivalent to the complex conjugate multiplication of two Fourier Transform.

$$R_{II}(x,y) = \frac{\sum_{i=1}^{N}\sum_{j=1}^{M}(I(i,j)-\bar{I})(I'(i+x,j+y)-\bar{I})}{\sqrt{\sum_{i=1}^{N}\sum_{j=1}^{M}(I(i,j)-\bar{I})^2}\sqrt{\sum_{i=1}^{N}\sum_{j=1}^{M}(I'(i,j)-\bar{I'})}} \qquad (3\text{-}27)$$

The most suited method of solving the discrete correlation function is by the FFT which can be written as

$$I(i,j)\Theta I'(i,j) \leftrightarrow FFT^{-1}[FFT(I) \times (FFT(I)')^{*}] \qquad (3\text{-}28)$$

Where the operations are defined as; Θ means correlation function, * represents complex conjugate and × is the piecewise multiplication of frequency components. Westerweel [63] suggested sub-pixel analysis to minimize the bias error introduced in the determination displacement vector.

Subsequently, we describe the set-up of planar 2D2C PIV experiment for the measurement of velocity components in the downstream section of an orifice.

3.2.7 Procedures

Here, we outline the apparatus set-up, flow set-up and optimization, experimental runs and data processing.

3.2.7.1 Apparatus set-up

1. To set-up the PIV, we determine the appropriate distance between the camera and the test piece section (object). For instance, using a camera resolution of 1152 × 480 pixels, and camera chip's pixel size of 11.5 microns, the size of the sensor in metric units is 13.248 × 5.52 mm. The focal length of the lens is 60mm. We can calculate the field-of-view (FOV) based on the horizontal and vertical angle of views as expressed in Equations (3-37) and (3-38) respectively and object distance. FOV is the portion visible to the camera based on orientation and position and it depends on focal length, sensor size, and object distance. The diameter of the pipe which is 25.4mm and the distance scale of the lens within which objects can be brought to a focus is set as 219mm - ∞. Since we want to focus on the pipe centerline and to create room for camera adjustment, the object distance can be fixed at 279.4mm (11D). Then, the FOV obtained based on these values is 61.69 × 25.70 mm.

$$\theta_h = 2\tan^{-1}\frac{h}{2f}, \text{ in degrees} \tag{3-29}$$

$$\theta_v = 2\tan^{-1}\frac{v}{2f}, \text{ in degrees} \tag{3-30}$$

where h and v represents x and y size of camera chip.

- Estimate the maximum velocity U_{max} is the downstream section of the orifice. From theoretical knowledge, the maximum velocity will be at the vena contracta and an idea can be gotten from computational results. This value is needed to determine recording parameters such as sample rates and exposure time (dt) in consonance with PIV guidelines. For example, 1152 × 480 pixels resolution is used for is 61.69×25.70 mm^2

  i.e. 61.69 mm = 1152 pixels.

  Let Δx be equivalent of 1pixel.

  The time Δt it takes a particle to travel a distance of 1 pixel is

  $\Delta t = \Delta x / U_{max}$

  Time for the particle to travel 8 pixels (one-quarter rule) $\Delta t_8 = 8 \times \Delta t$

  Exposure time = $\Delta t_8 / 10$

  Sample rate (fps) = $1/ \Delta t_8$

  The exposure rate determines the time delay between pulses of the laser. In this case, this value is recorded when importing images to PIV Dantec Dynamic studio. Also, the sample rate must not exceed the maximum allowable frame rate of the camera. The sample rate increases with decreasing resolution.

2. Align the laser with test section

   - The distance of center of pipe from the board is 6.61 cm while the distance from the base of laser head to the center of the laser aperture is 4.5 cm. The laser had to be raised by a platform with 2.21 cm thickness. The platform was fabricated to permit movement of the laser along pipe axial distance.

- connect the laser to power source, here 110V.
- The laser should be set to a low current setting to give laser light strong enough to graze the test section to check for alignment of laser light with pipe centerline
- Switch off the laser.

3. Set-up and align the camera
    - Place the tripod at a distance within the depth of field that guarantees a clear view of the pipe centerline. Here, an estimate of the depth of field based on the lens specification and calculated distance between the test-piece and camera is 277.8 mm – 279.4 mm.
    - Set the camera using the tripod and bubble gage in achieve alignment and stability.
    - Switch on the camera, load the PCC camera program on the computer system and adjust the camera to focus on the test piece.
    - Cover the camera lens with the cap and carry out intensity calibration.
    - Remove the cap and return to continuous grab mode. Adjust the camera resolution to accommodate the desired FOV (for example 60mm × 25.4mm corresponds to 1152 × 480 pixels).
4. Flow Set-up
    - Prepare a homogeneous mixture of seeding particle and add to water tank.
    - Keep the flow running for some minutes to enhance mixing and correct possible leakages
    - Adjust the flow rate to the desired value using valve upstream the pump

5. Set-up optimization

   - Enter the sample rate into the PCC program and adjust the exposure time.
   - Switch on the laser and set the current to the highest value (here, 5.7A). Then check for saturation of the camera by the image intensity. Adjust the laser current if such is noticed.
   - Record hundreds of images, preview recorded images to check for image density, particle drift, and out-of-plane motion and make the necessary adjustment to recording parameters to achieve improved PIV images.
   - Check that the image density is suitable for PIV technique and verify the focus of the images. Particle images must be 8-15 particles per 32 × 32 pixel IA. A simple approach is to count the number of particles in the cross-hair. The size of the cross-hair is approximately 32×32 pixels. Increase a number of seeding particles to meet this condition if not met.
   - The particles must follow the one-quarter rule i.e. particle drift must not be more than 8 pixels for 32×32 pixel. If the particles shift more or less, decrease or increase time delay dt respectively.
   - If a group of particles is difficult to track due to out-of-plane motion, it can be rectified in two ways. Offset the camera from the focal point to increase the light thickness or increase the depth of focus by increasing the distance between the camera and light sheet.

6. Experimental Runs

    - Perform a camera intensity calibration with the cap on the camera assembly to set a reference for the intensity. Once calibration is finished, remove the cap.
    - Set the laser to the optimized repetition rate and current. Before switching the laser to external mode, make sure the laser receives a continuous trigger signal that matches the set frequency. Turn the laser on.
    - Run the pump and adjust the valve until the desired flow rate is set and flow stabilizes.
    - Set the mode of the camera to Continuous grab and check that the particle images are focused.
    - Set the mode of the camera to Record and save the desired number of images.
    - Turn off the laser when recording is finished. Review the images to check for particle density, particle shift and out-of-plane motion.
    - Take more runs and record more images.

Images of flows were acquired as single frames with the camera using the PCC studio. Proceeding to the PIV analysis, the images were exported to Dantec Dynamic Studio and stored in the database as normal images to notify the system that they are meant for measurements. The field of view method of calibration was adopted for this study to inspect and modify origin and scale factor used in converting image plane (pixels) to object plane (metric units) by specifying the height which is equivalent to the pipe diameter Then the analysis sequence displayed in Figure 11 was applied to the normal images stored in the database. A brief look into each step of the sequence goes thus;

1. Making Double Frame; this process is applied to the raw images to convert them from single frames to double frames by combining them in twos. This was done by specifying N/2 double images in the option.
2. Image Min and Max; this method is a subset of Image Processing category and it is used to determine the field of minima/maxima over a series of images. Here, the method is used to extract the field of minima from the paired raw images obtained from the previous conversion. It returns one image.
3. Image Arithmetic; this method allows performing arithmetic (addition, subtraction, multiplication and division) on pixel values of any image type like 8, 10 or 12-bit. Here, it is used to subtract the minimum image from step (2) from the raw images in step (1). This is a form of background subtraction technique to remove background noises from the raw images.
4. Image Mean; this calculates the average intensity of corresponding pixels (pixels with identical coordinates) in all selected images. The images must be compatible in terms of dimensions and grayscales. The inputs for this step are images from step (3) and the output is a single map.
5. Image Processing Library (IPL)-Blur; this module contains filters like low-pass filters, high-pass filters, Morphology, signal processing, utility and threshold that can be used smooth images, detect edges, enhance image contrast, carry out non-linear calculations. The image from step (4) is processed to reduce the particle image intensity by blurring.

6. Image Arithmetic; this is used to subtract output image of step (5) from the raw images obtained in step (3). The aim is to reduce the intensity of each image in the ensemble.
7. Image Processing Library (IPL); here we applied Gaussian filters (5×5) twice to images from step (6) to smooth the images. This step makes the images of particles more visible. The Gaussian filter is a linear low-pass filter like mean filters but differs is the sense that it weighs grayscale at the center of kernels higher than those at the edges.
8. Image Min and Max; this step selects the minimum field form images from the output of step (8).
9. Image Arithmetic; this is used to subtract output image of step (8) from the raw images obtained in step (7). The aim is to check the numeric diffusion that may have been introduced by applying filters.
10. Adaptive Correlation; Correlation algorithm is applied to output images from step (9) to generate vector maps. Adaptive correlation is a form cross-correlation with additional post-processing algorithms like local validation. It calculates velocity vectors by specifying an initial IA (256×256) with size multiples (N=refinement steps) of the size of final IA (32×32) and uses the intermediate results as information for the next smaller size till the final IA is attained. Additionally, processes like local validation to detect bad vectors, the overlap of IA to compensate for the loss of vector field resolution, high accuracy module, and window deformation were applied to the images using this correlation type. Local validation was achieved through Peak Validation and Local Neighborhood

Validation. The overlap of IA was achieved with 50% overlap between IA pairs in both horizontal and vertical directions. The velocity vectors were obtained from displacement vectors and time interval using the Central Difference Scheme which is the most accurate methodology suitable for PIV measurement.

11. The high accuracy sub-pixel interpolation is part of the adaptive correlation algorithm that is used to determine correlation peak.
12. Vector Statistics: this calculates statistics from multiple vector maps and presents the results of mean velocity vectors in a vector map. Other statistical quantities calculated are standard deviations, variances, and covariances between different velocity components.

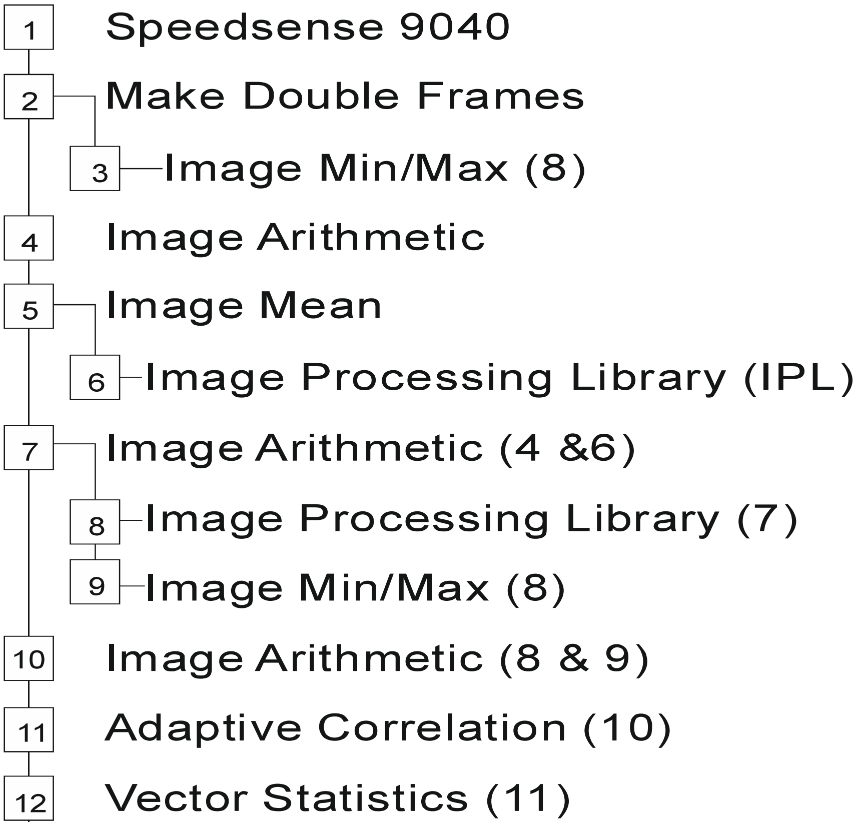

Figure 11 Analysis Sequence

CHAPTER 4

FLOW FIELD CHARACTERISTICS

Results obtained from computational investigation of flow characteristics for the three geometries considered; single orifice flow, double orifices with one-pipe diameter spacing and double orifices with two-pipe diameter spacing are presented here. These results are presented in such a way to enable discussion of flow field characteristics for single orifices of diameter ratios 0.5, 0.63 and 0.77 at inlet velocities 1 m/s, 2 m/s and 4m/s. This is followed by results of the other geometries for the diameter ratios and velocities specified above together with comparisons with single orifice geometry.

4.1 Main Flow Features

Orifices influence flow field both upstream and downstream of the orifice plate. Figure 12a represents the velocity vectors for single orifice of diameter ratio, $D_r = 0.63$ at $V_i = 2$m/s. It is evident that the fully developed velocity profile becomes distorted as the flow approaches the upstream face of the orifice plate. The flow accelerates towards the orifice throat by contraction process which extends downstream the orifice as the flow is driven by the vortex structures formed due to flow separation to a point of minimum area of jet flow called vena contracta. Downstream of the vena contracta the flow decelerates and continues to develop until reaching the fully developed region. The vena contracta takes place at the section of maximum velocity and minimum pressure as shown in Fig. 12b.

Figure 13 is a plot of lines of constant stream function which shows the streamline patterns for flows involving orifices of $D_r = 0.5$, 0.63 and 0.77 in a single orifice configuration for the case of $V_i = 2$ m/s. It can be seen that there are regions of recirculation immediately downstream of the orifice plate and reattachment further downstream.

The streamlines are drawn with constant $\Delta\psi$. From the expression of stream function-velocity relation; $\Delta\psi = -v\,dx + u\,dy$, it can be deduced that the region with dense streamlines has higher velocity since the streamline spacing is very small and vice versa. Then, the velocity decreases towards the reattachment zone far downstream of the orifice plate. It is also evident that as the orifice diameter ratio decreases the recirculation zone gets larger. This invariably causes more vortex pairing bringing about increased velocity as will be shown later. These regions are very important in studying erosion features. Previous studies by [17] showed that separation of flow at the throat of an orifice produces downstream field features possessing higher velocities, streamlines with large curvatures, formation of recirculation and reattachment zones.

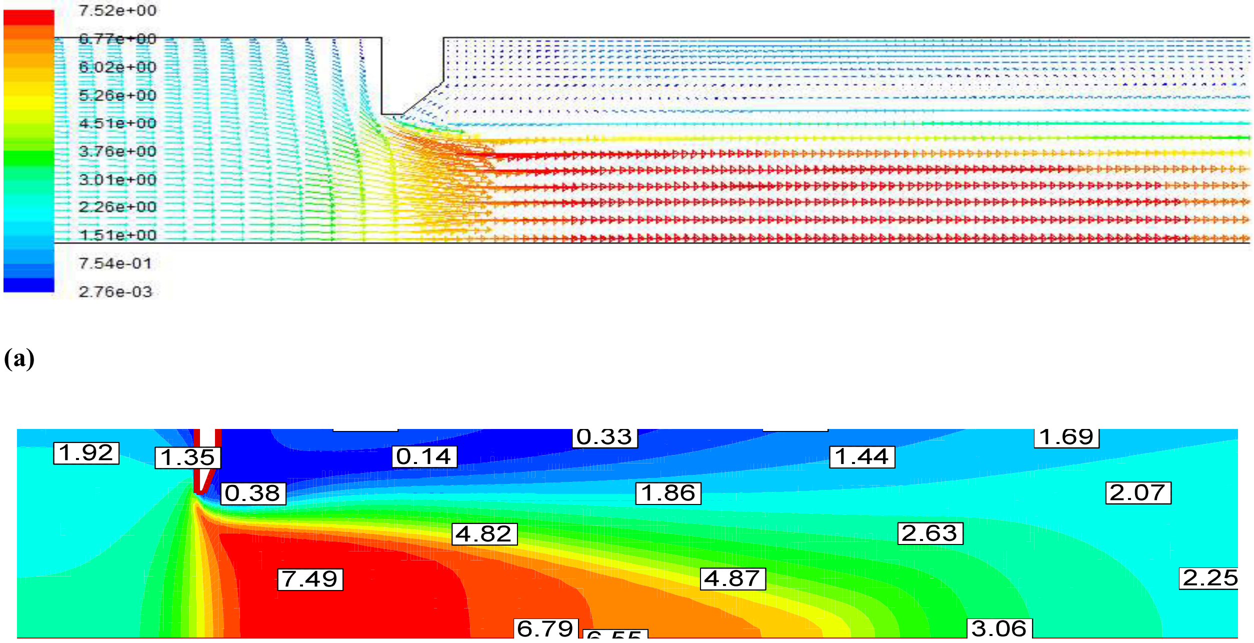

(a)

(b)

Figure 12 Contour plots of velocity vectors and velocity magnitude (m/s) downstream orifice, for single orifice Dr = 0.63, Vi = 2m/s: (a) Velocity vectors and (b) Velocity magnitudes

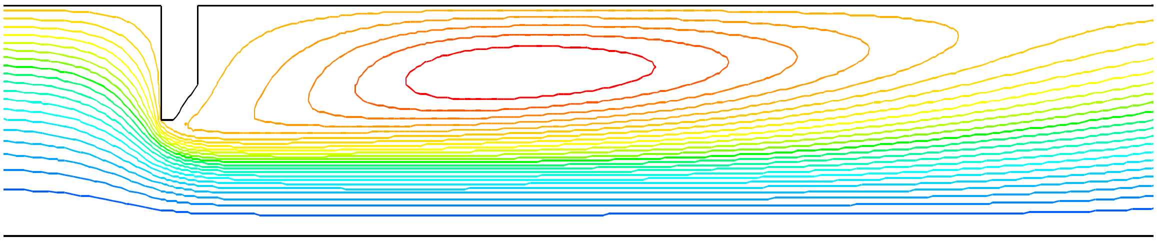

(a) Diameter ratio = 0.5

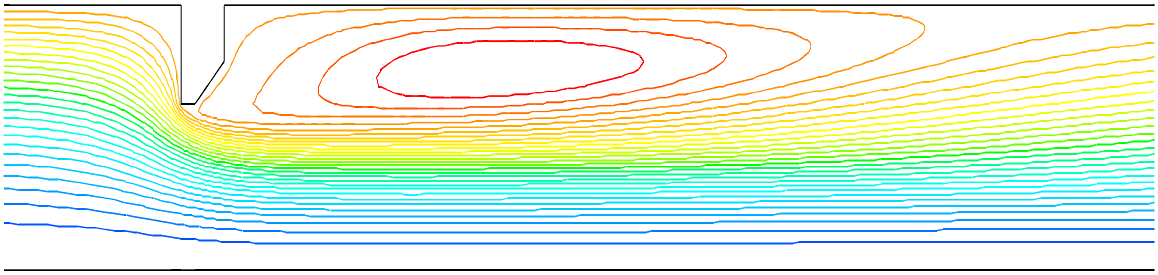

(b) Diameter ratio = 0.63

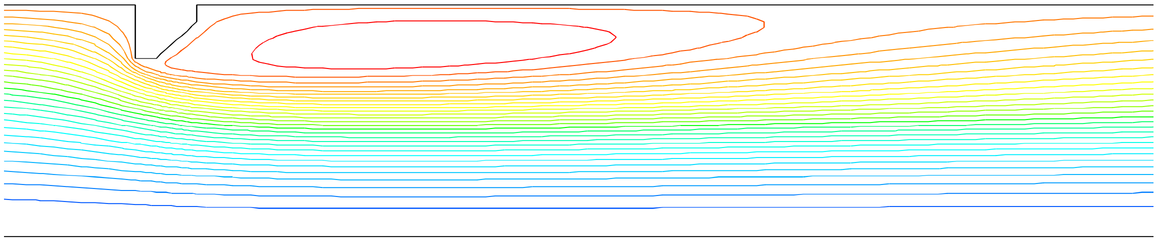

(c) Diameter ratio = 0.77

Figure 13 Comparison between streamline plots for a single orifice at Vi = 2m/s, cases of (a) Dr = 0.5, (b) Dr = 0.63, (c) Dr = 0.77

The effects of placing a second identical orifice at axial distance of 1D and 2D downstream on velocity distribution, pressure drop and skin friction coefficient were also investigated. From the contour plots of velocity vectors and magnitudes shown in Fig.14, the upstream conditions and occurrence of vena contracta associated with the first orifice is qualitatively similar to those observed for a single orifice flow. It is clear from the figure that the location of the second orifice at 1D or 2D spacing disrupts the recirculation and reattachment processes caused by the first orifice respectively.

This causes the whole annular region between the two orifices to be occupied by recirculation zones as shown in Fig.15.

In the case of 1D spacing, the flow structure in between the two orifices is characterized by a jet-like flow in the inner region (core region) surrounded by a donut-shaped vortex (recirculating flow) in the outer region (wall region). This recirculating flow region is characterized by higher vorticity near the upstream side of the second orifice and lower vorticity in the leeside of the first one. As for the region between the two orifices in the case of 2D spacing, a longer recirculation zone occupies the entire length of orifice spacing. A second low velocity recirculation zone (almost stagnant fluid zone) exists near the second orifice.

The streamlines in the core region between the two orifices in the case of 2D spacing (Fig.15b) indicate wider jet associated with lower axial velocities in the immediate neighborhood (upstream region) of the second orifice. This gives rise to the formation of a vena contracta downstream of the second orifice due to the streamtube contraction (Fig.15b). This makes the flow structure upstream and downstream of the second orifice in the case of 2D spacing totally different from that in the 1D spacing (Fig.15a). The presence of this vena contracta downstream of the second orifice led to the formation of a recirculation zone possessing higher velocity and higher vorticity in comparison with that in the case of 1D spacing (Fig.15a).

In addition, the flow structure upstream of the second orifice in both cases of 1D and 2D orifice spacing is completely different from that upstream of the orifice in the case of single orifice configuration. The jet-like flow approaching the second orifice (Fig.15a,b) has a significant impact on the flow structure downstream of the second orifice, thus affecting the velocity distribution, separation and reattachment flow zones as well as the vortex formation and recirculating flow zone.

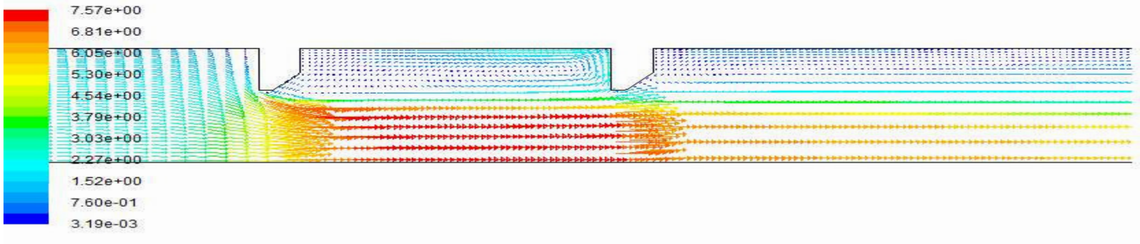

Single orifice-1D-separation

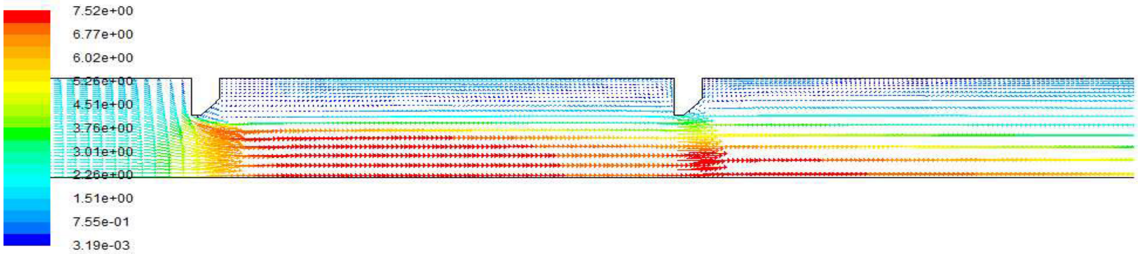

Double orifice-2D-separation

(a)

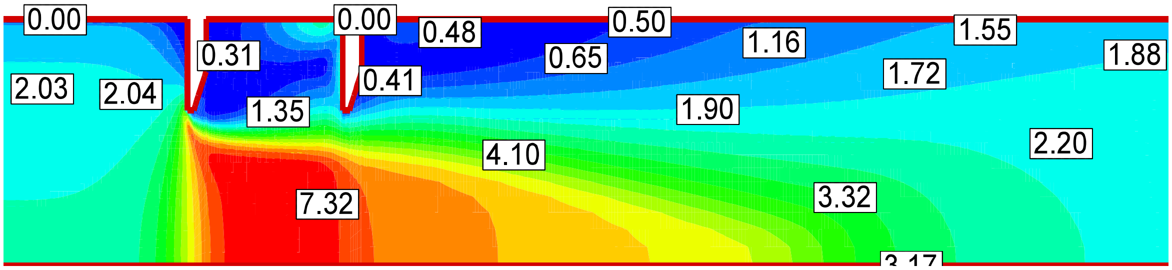

Double orifice-1D-spacing

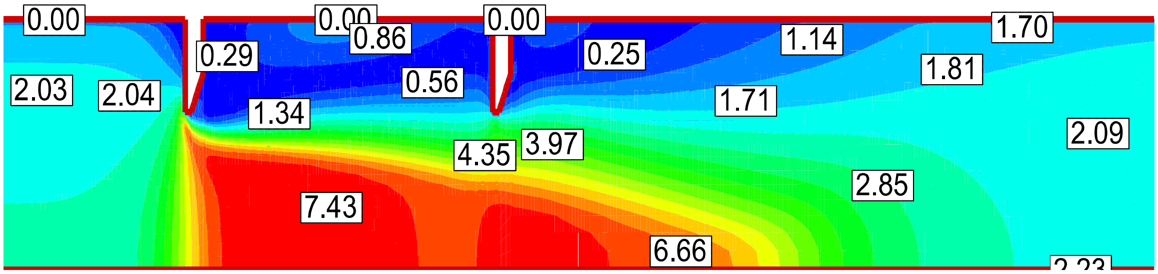

Double orifice-2D-spacing

(b)

Figure 14 Contours plot of velocity vectors and velocity magnitude (m/s) downstream orifice, for Double orifice with $D_r = 0.63$, Vi = 2m/s: (a) Velocity vectors and (b) Velocity magnitudes

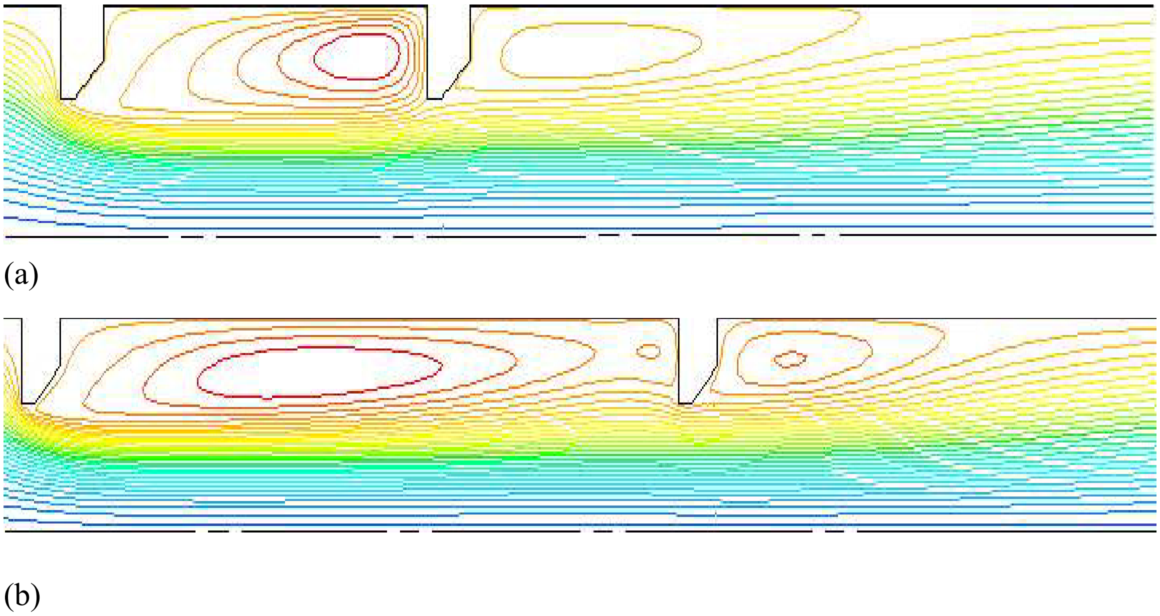

Figure 15 Comparison between streamline plots for double orifice of Dr = 0.63 and Vi = 2m/s with (a) 1D and (b) 2D spacing

4.2 Axial Velocity and Vena Contracta

The location of vena contracta was determined by identifying the point of maximum centerline axial velocity. Figure 16 shows the variation of the downstream centerline axial velocity normalized with the average axial velocity at different inlet velocities for single orifice with $D_r = 0.63$. It can be seen that the location of peak normalized axial velocity for the average velocities considered is approximately at X/D = 0.5 which invariably indicates the position of vena contracta in this region. This agrees very well with observations of location of vena contrata at approximately X/R = 1 obtained by Shan et al.[10]. It is also observed that varying inlet velocities has negligible effect on the position of vena contracta and small effect on the normalized axial velocity variation. In this study, similar trend was observed for orifices with different diameter ratios. Also, the flow re-attains its mean axial velocity at approximately x = 8D for all velocities considered.

In the case of double-orifice arrangement, the location of vena contracta downstream of the first orifice is approximately at X/D = 0.5 for both cases of 1D and 2D orifice spacing as shown in Fig. 17. This is similar to what is observed for single orifice. So, it can be deduced that the presence of second orifice at 1D or 2D spacing has negligible effect on the location of vena contracta of the first one. Also, the normalized centerline axial velocity variations in both double-orifice arrangements show little changes with inlet velocities. Figure 17a shows that one peak velocity exists in double orifice-1D-spacing which is caused by the first orifice. On the other hand, the axial velocity variation shown in Fig. 17b for double-orifice arrangement with 2D spacing indicates the presence of two local peaks with a trough in between.

The first local peak is associated with the first orifice plate while the second local peak is due to the presence of the second orifice and located at approximately x/D = 2.2 (i.e. at a distance of 0.2D downstream of the second orifice) which is closer to the second orifice in comparison with that downstream of the first one. The figure also shows negligible dependence of that location on the flow average velocity. This can be explained with the help of the streamlines plotted in Fig.15b that shows little contraction in the streamtube in the immediate neighborhood of the second orifice (upstream side) in comparison with that upstream of the first one. Accordingly, the turning point at the trough can be attributed to the contraction process that sets in as the jet-like flow approaches the entrance of the second orifice. Figure 17b also indicates that the second peak is slightly higher than the first one. Further downstream, the flow decelerates towards the reattachment zone and thereafter attains the mean flow velocity.

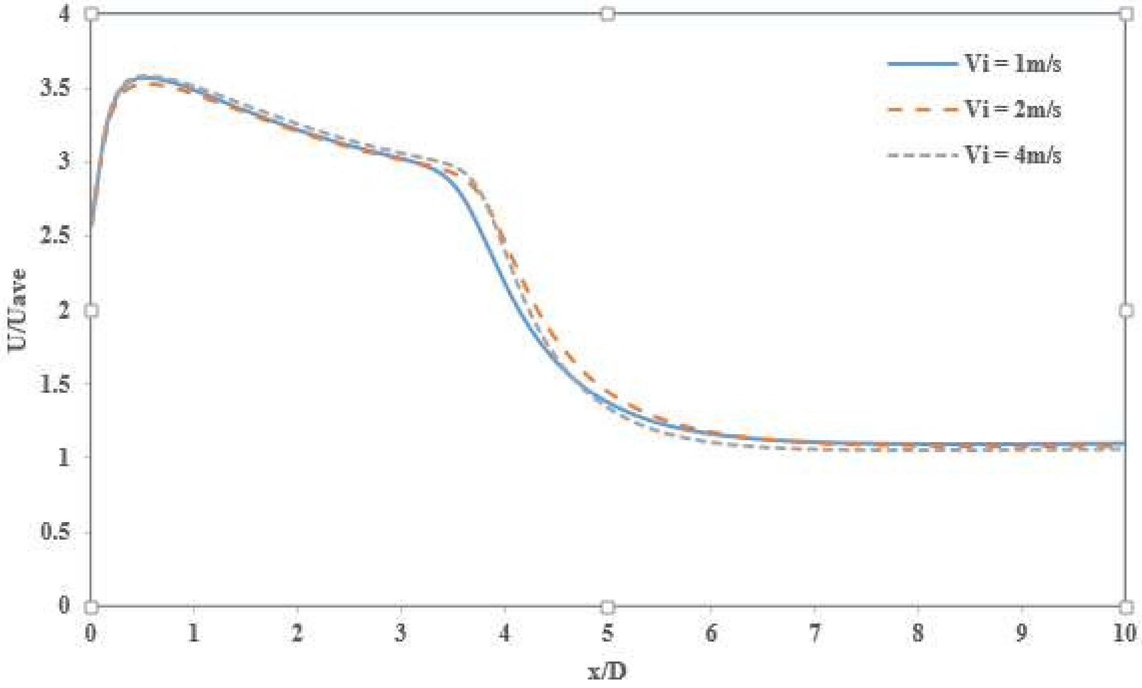

Figure 16 Centerline axial velocity plots for a single orifice with D_r = 0.63 at inlet velocities 1, 2 and 4m/s

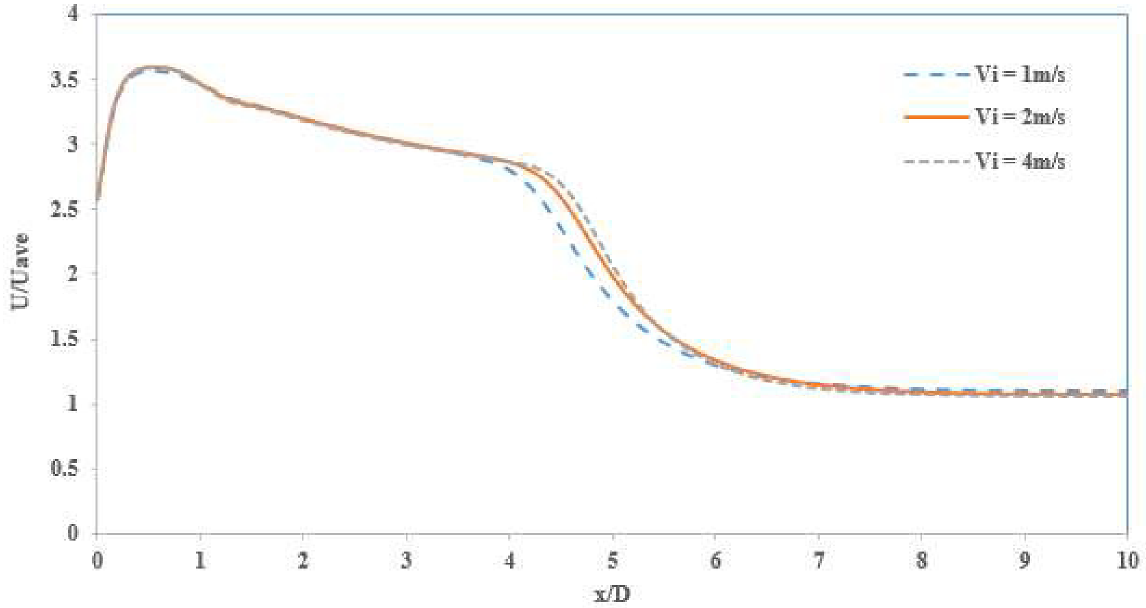

(a)

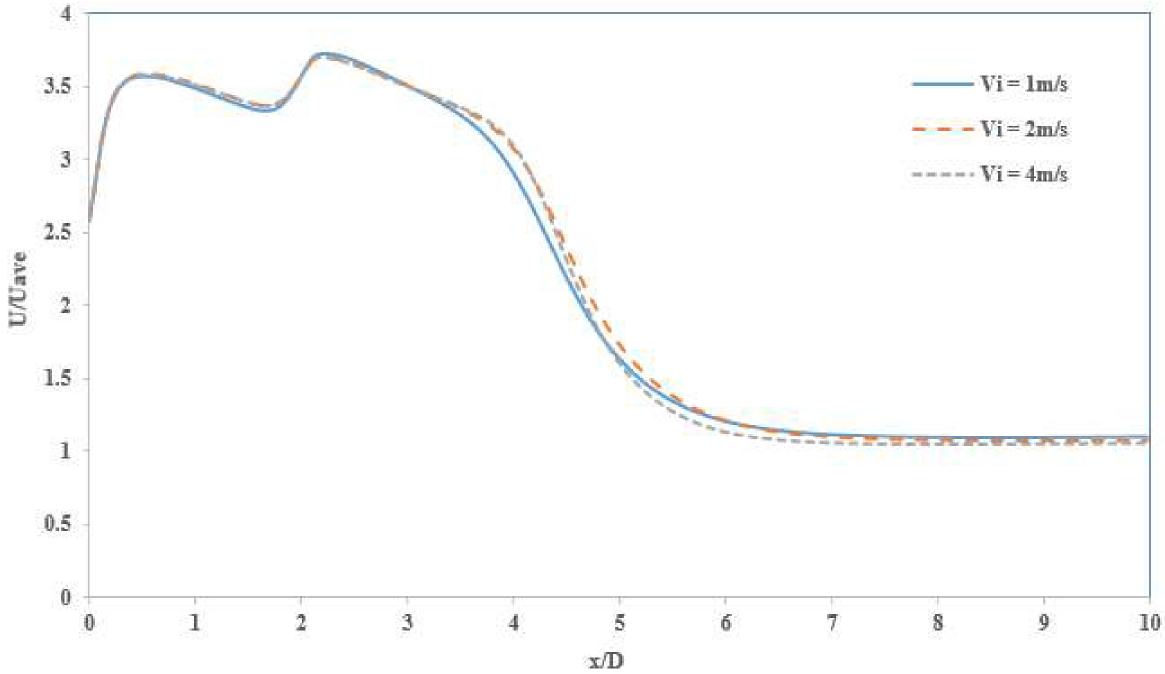

(b)

Figure 17 Normalized Centerline axial velocity plots of D_r = 0.63 at inlet velocities 1, 2 and 4m/s for (a) Double orifice-1D-spacing (b) Double orifice-2D-spacing

Figure 18 shows the plot comparing the downstream normalized centerline velocity of different configurations of single orifice, double orifices with 1D and 2D spacing for D_r = 0.63 and V_i = 2m/s. It can be seen that the peak velocity associated with the single orifice and the first orifice of double-orifice arrangement exists in the same location but with slightly higher velocity in double-orifice cases. The normalized axial velocity profile for double orifice with 1D spacing shows a trend of steep slope similar in magnitude to that of single orifice flow. But the steep slope extends further by approximately x = 0.5D beyond that of single orifice before it changes to higher negative slope. This is attributed to the presence of the second orifice that helped to maintain the jet-like flow over longer distance thereby delaying the sharp drop in velocity signifying the approach of the reattachment zone.

In the case of double orifice flow with 2D spacing, a second peak occurs downstream the second orifice due to the contraction process and presence of vena contracta. A comparison among the velocity magnitudes in the immediate region downstream the second orifice in two orifices configuration and that of single orifice shows that the double orifice with 2D spacing has the highest velocity while that of 1D spacing has the lowest velocity. The flow structure and velocity magnitudes downstream of the second orifice are very important in the study of solid particle erosion in orifice flows.

The centerline axial velocity profiles shown in Fig.19 indicate that highest and least maximum velocities are associated with orifice plates with smallest and largest diameter ratios respectively. This is quite expected since the stream tube contraction occurring in orifices with smaller D_r is much larger than that occurring in large D_r orifices. The trend is such that orifice sizes of 0.5, 0.63 and 0.77 give approximate maximum normalized axial velocities of 6.0, 3.73 and 2.32 respectively. The effect of varying diameter ratios on axial velocity distribution for double orifices with 1D and 2D spacing follows the same trend as that presented in the case $D_r = 0.63$ as shown in Fig.20. It is clear from the figure that the centerline axial velocity decreases as the diameter ratio increases. It is also evident from the profiles that the negative axial velocity gradient after the peak increases with decreasing diameter ratio. Also, the position at which the flow re-attains its mean axial velocity downstream the orifice/s is approximately at x = 8D for all configurations and all diameter ratios considered.

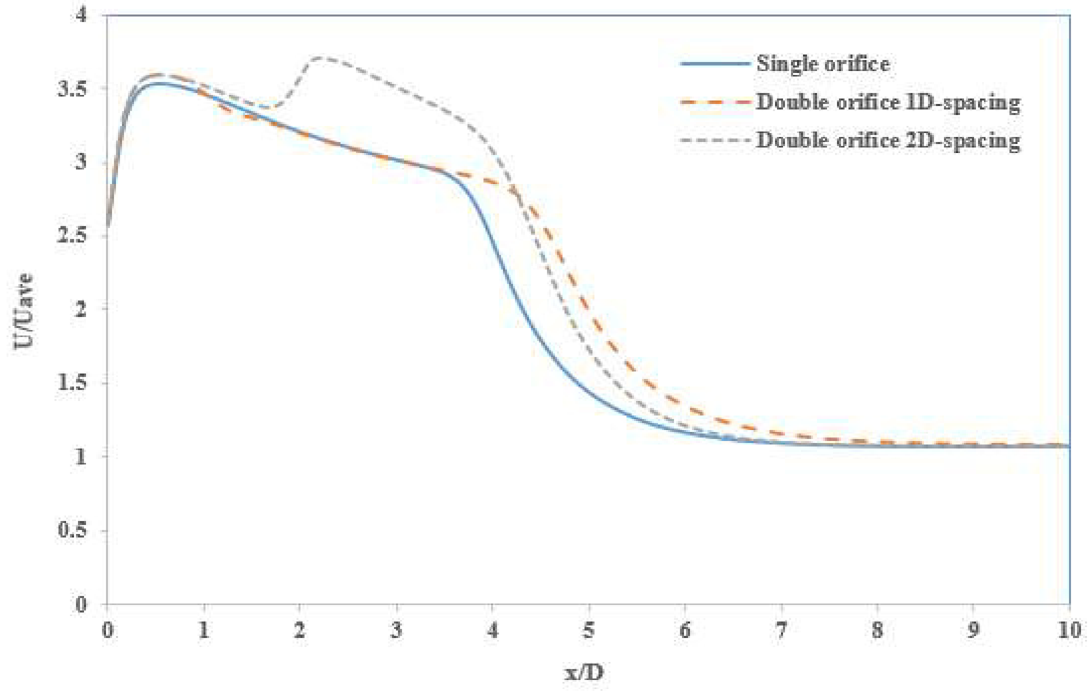

Figure 18 Comparison of centerline axial velocity for different configurations of single orifice, double orifice with 1D and 2D spacing for $D_r = 0.63$ and $V_i = 2m/s$

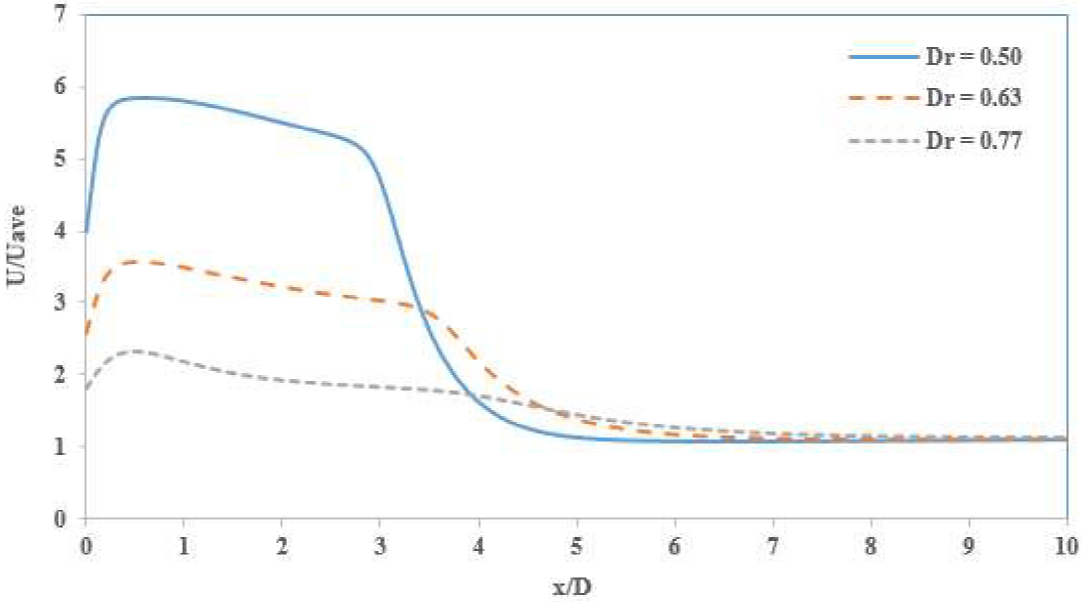

Figure 19 Comparison of centerline axial velocity plots for a single orifice with D_r = 0.5 0.63 and 0.77 and V_i = 2m/s

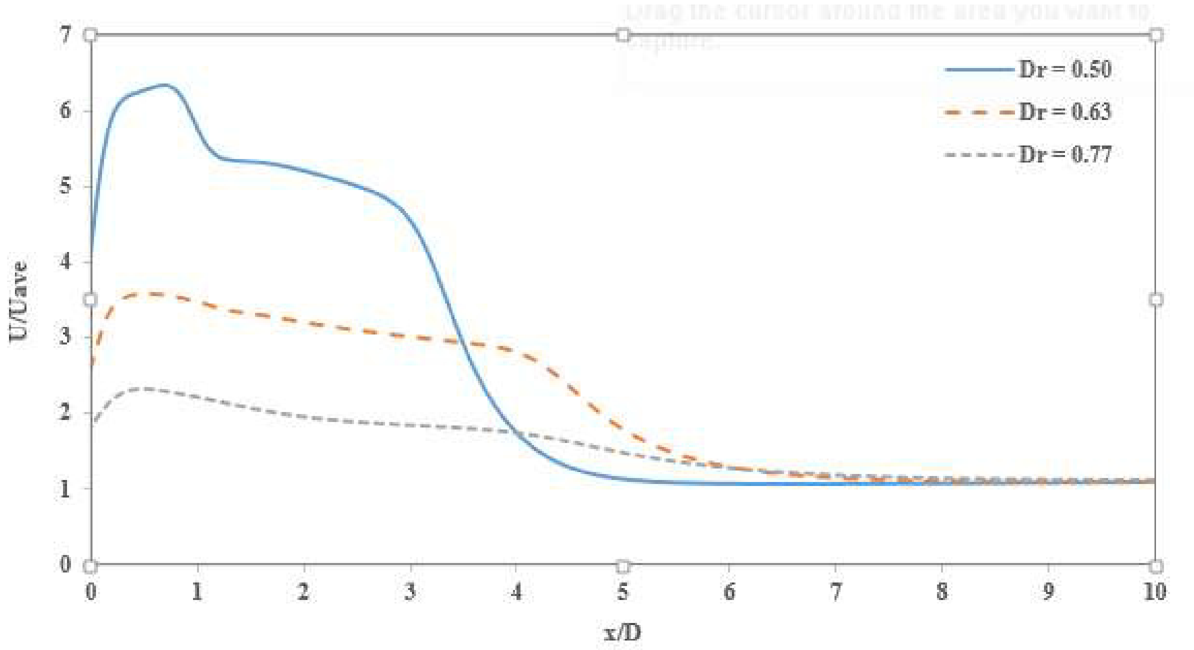

(a)

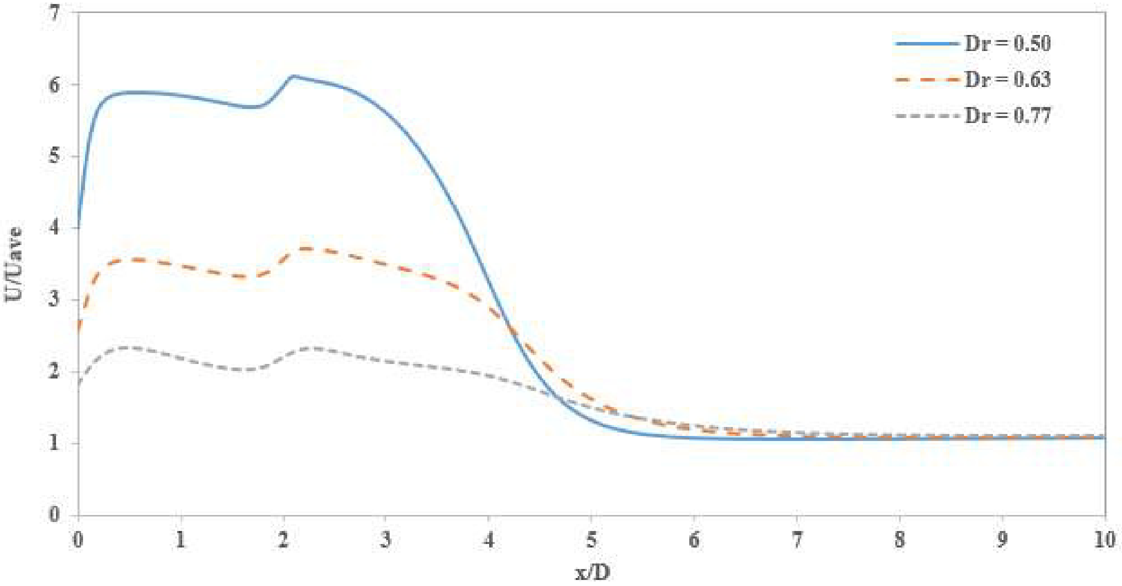

(b)

Figure 20 Comparison of centerline axial velocity plots of different D_r = 0.5, 0.63 and 0.77 for (a) double orifice with 1D-spacing (b) double orifice with 2D-spacing, case of V_i = 2m/s

4.3 Pressure Drop

Another important property characterizing flow through an orifice is the pressure drop. It is known that the pressure variation in an orifice flow depends on the following;

- fluid properties, namely, density and dynamic viscosity (ρ, μ)
- flow average velocity, U_{av}
- orifice diameter ratio, D_r
- pipe size, D, and surface roughness, ε
- axial distance, x
- orifice spacing for double orifice arrangement, S

Mathematically, this can be expressed as,

$$\Delta p = f\left(\rho, \mu, U_{av}, D, D_r, \varepsilon, x, S\right) \tag{4-1}$$

Based on Buckingham Π-theorem, the relation between the above variables can be written in dimensionless form as,

$$\frac{\Delta P}{\frac{1}{2}\rho U_{av}^{2}} = f\left(R_e, D_r, \frac{\varepsilon}{D}, \frac{x}{D}, \frac{S}{D}\right) \tag{4-2}$$

The term on the left hand side is known as pressure coefficient (C_p). This study investigates the effect of all independent variables $\left(\mathrm{Re},\ D_r,\ x/D \text{ and } S/D\right)$ on the pressure coefficient except for the relative roughness (ε/D) since the pipe surface is assumed smooth.

In this section, the effects of varying inlet flow velocity (V_i = 1 m/s, 2 m/s, 4 m/s), geometry of orifice plates (D_r = 0.5, 0.63, and 0.77) on the pressure drop in the three different geometries of single orifice and double orifice with 1D and 2D spacing is considered in some detail. A typical static pressure variation has a linear portion in the far upstream and far downstream zones, both having equal negative gradient in the downstream section. The pressure drop caused by the orifice results from the abrupt change in the flow passage cross-sectional area causing high level of turbulence and thus creating considerable hydraulic losses. This pressure drop can be obtained from the computed (or measured) static pressure variation by extrapolating the far upstream and far downstream linear pressure variations towards the orifice plate. The difference in pressure values at the upstream and downstream sides of the orifice plate (x=0) gives the pressure drop caused by the orifice as can be seen in Fig. 21.

The value of Δp given in Eq. (4-1) represents the difference in pressure between any given location and a reference pressure. The selection of the reference pressure differs from one study to another. For example, Ahmed et al. [17] chose the outflow pressure (p_{out}) as the reference pressure in their analysis. The value of reference pressure can also be taken as pressure value (p_{5d}) at an axial distance of 5-orifice diameters upstream the orifice plate as used by Manmatha & Sukanta [32]. The reference pressure adopted in this study is the static pressure (P_{5D}) at axial distance of 5D upstream the orifice plate (i.e. x= –5D). Accordingly, the pressure further upstream with values higher than P_{5D} has positive values while pressure downstream of that location have negative values. In this study, the origin is selected at the orifice plate which makes the upstream and downstream regions have negative and positive axial locations respectively.

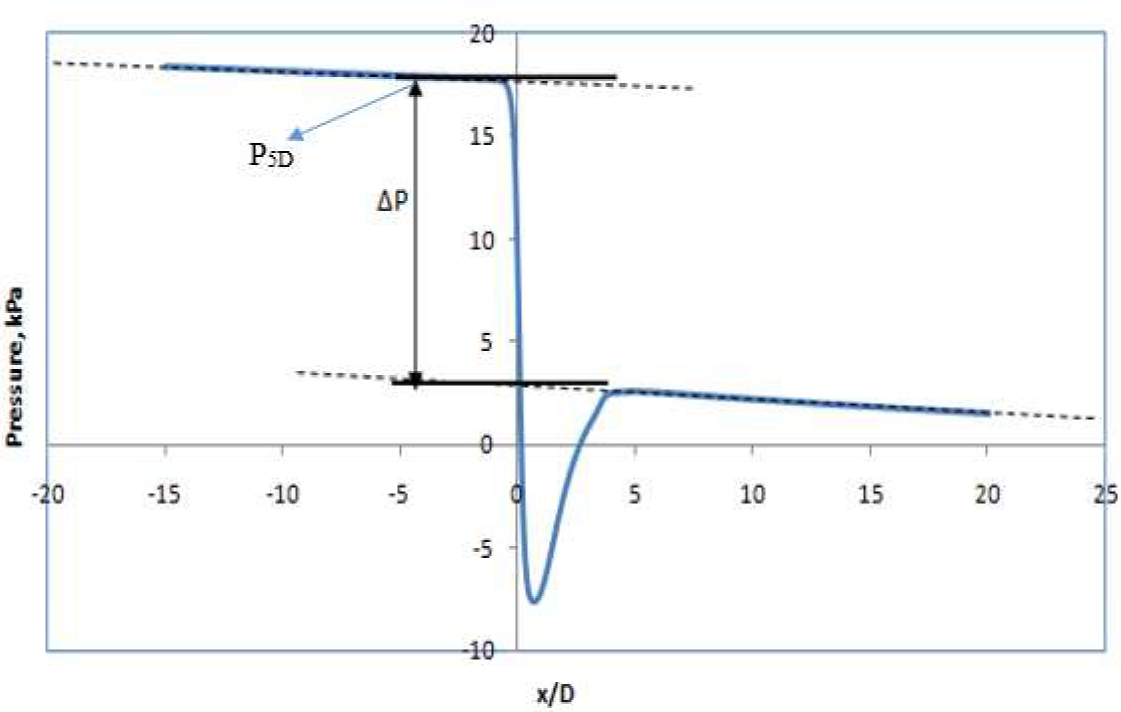

Figure 21 Illustration of determination of ΔP from static pressure values

4.3.1 Pressure Variation in Single Orifice Flow

The wall surface pressure distributions for single orifice flow at an inlet velocity = 2 m/s through a pipe of internal diameter 25.4 mm containing orifices of diameter ratios, D_r = 0.5, 0.63, 0.77 are shown in Fig. 22. The pressure profile shows a steady decrease in pressure as the flow approaches the orifice plate followed by a large drop over a short distance from a location around 1D upstream till it attains a minimum value in the downstream section. The magnitude and location of the minimum pressure attained varies with diameter ratio of orifices. As expected, orifices with smaller diameter ratio produce the lower minimum pressure compared to larger diameter ratios. Likewise, the axial pressure drop across orifices decreases with increasing diameter ratio. A simple explanation of this is based on the application of the one-dimensional energy equation for steady incompressible.

This results in lower pressures at the plane of the vena contracta as D_r decreases. Further downstream of the location of minimum pressure, there is a sharp rise in magnitude of pressure over a distance of around 4D till it attains a peak value in the downstream section. This is due to the diffuser shape of the stream tube starting from a minimum jet flow area at the vena contracta to a larger flow area downstream. The downstream peak pressure value is located in the reattachment region where flow expansion is most prominent. Downstream the point of peak pressure value, the pressure continues to decrease having negative pressure gradient towards the exit section where the flow re-attains its fully-developed velocity profile possessing a linear negative pressure gradient.

The variation of pressure coefficient (C_p) with normalized axial distance at different inlet velocities for an orifice with D_r = 0.63 is shown in Fig. 23. It is evident from the negligible difference among the three profiles that variation of C_p has little dependence on inlet velocity and invariably little dependence on Reynolds number. Also, it can be observed that the minimum pressure for the inlet velocities considered occurred around x = 0.5D downstream the orifice, which coincides with the region where the vena contracta exists. Figure 24 shows a plot of pressure coefficient, C_{pe} (based on exit pressure, p_e, as a reference pressure), in the downstream section for the three orifice diameters ratios considered for the case of V_i = 2m/s.

The variations of C_{pe} for the three diameter ratios are similar but differs quantitatively up to x = 5D. The minimum values of C_{pe} for the diameter ratios considered exist at the vena contracta section at approximate locations of x/D = 0.26, 0.5 and 0.8, for orifices with D_r = 0.77, 0.63, and 0.5, respectively. The pressure then increases until reaching a downstream peak pressure value at approximately x = 5D in the reattachment zone followed by a steady linear negative pressure gradient towards the exit section. The most remarkable decrease in C_{pe} was produced by the orifice with D_r = 0.5 while the least by the one with D_r = 0.77.

4.3.2 Pressure Variation in Double Orifice Flow

The pressure variation for double orifice configurations is similar to that of the single orifice in the upstream section. The pressure distribution along the pipe axis possesses a small negative gradient followed by a large negative gradient until reaching the minimum pressure at the vena contracta. The pressure variation for double orifice with 1Dspacingis plotted in Figure 25a for orifice plates with three different diameter ratios (D_r = 0.5, 0.63 and 0.77) for the case of V_i=2m/s.

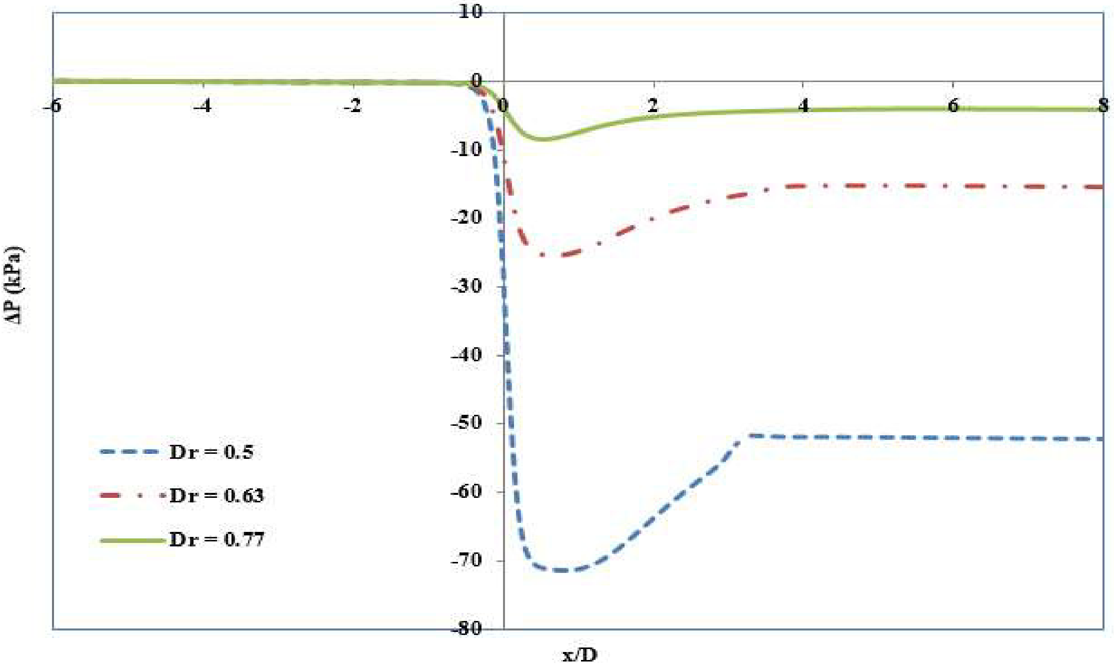

Figure 22 Variation of static pressure variation with normalized axial distance as a function of diameter ratio for a single orifice flow at V_i = 2m/s

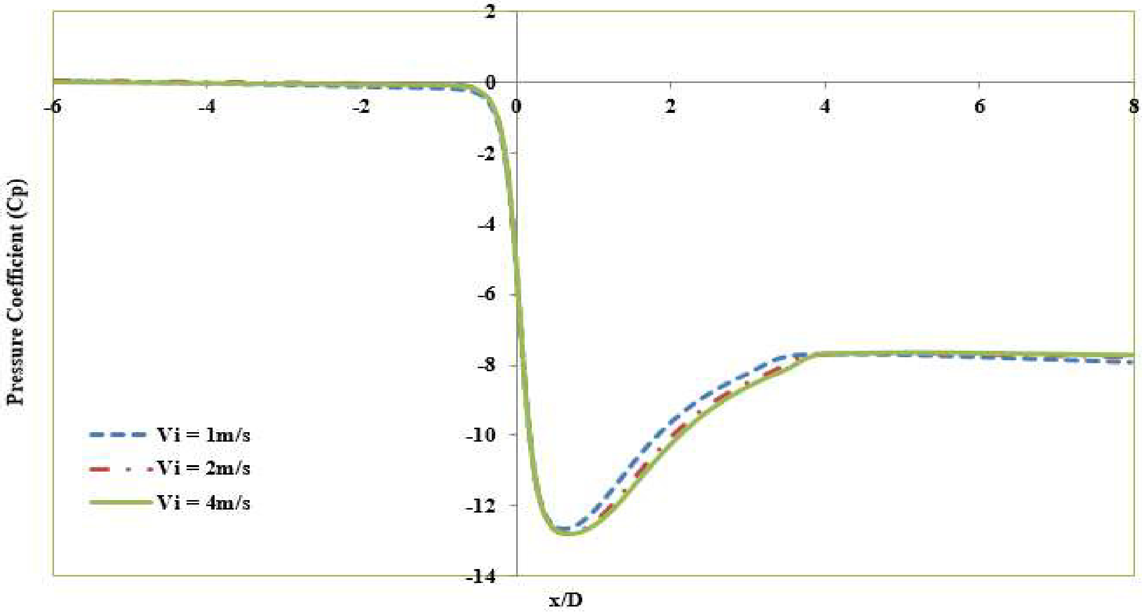

Figure 23 Variation of C_p with normalized axial distance as a function of inlet velocity for a single orifice flow with D_r = 0.63

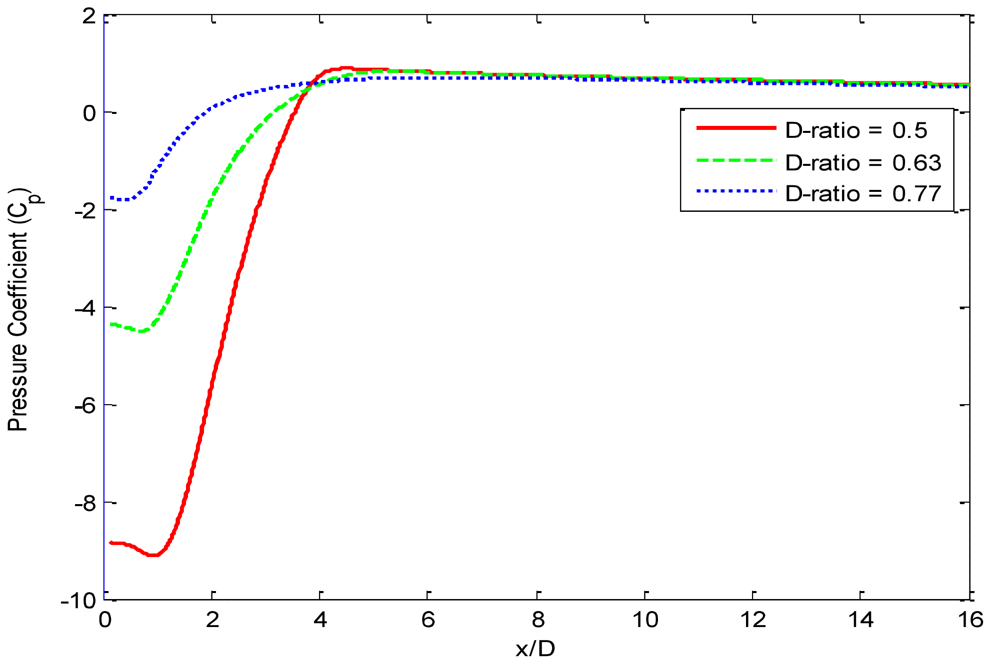

Figure 24 Variation of C_p with downstream normalized axial distance as a function of diameter ratio for single orifice flow at V_i = 2m/s

It is clear from the pressure distribution that there is only one location of minimum pressure with a magnitude depending on the orifice diameter ratio. This agrees very well with the streamlines plotted in Figure 15a indicating the presence of one vena contracta downstream of the first orifice and the absence of such phenomenon downstream of the second one.

Figure 25a also indicates a positive pressure gradient across the location of the second orifice for all of the three diameter ratios. A simple comparison between Figures 22 and 25a shows a higher pressure gradient $\left(\partial p / \partial x\right)$ downstream of the vena contracta in the case of double orifice with 1D spacing compared to that of a single orifice. Another interesting phenomenon, in the case of 1D spacing, is the existence of a positive pressure gradient across the second orifice for the three diameter ratios of D_r=0.5, 0.63 and 0.77 (Figure 25a). This can be explained based on the variation of the flow velocity along the pipe axis plotted in Figure 20a for the same cases. The figure indicates a flow deceleration across the plane of the second orifice with a higher rate for the orifice having D_r=0.5 and much lower rates for the other two. Such flow deceleration will definitely cause a positive pressure gradient in the downstream direction.

Figure 25b shows the pressure distribution for double orifice arrangement with 2D spacing for the same three orifices (D_r= 0.5, 0.63 and 0.77).These pressure distributions are totally different from those of 1D spacing presented (Figure 25a) due to the presence of two vena contract as (one downstream of each orifice) creating two points of local minimum pressure. In addition, the total pressure drop caused by the two orifices is much higher in the case of 2D spacing than that of 1D spacing. One can also observe the negative pressure gradient across the second orifice plane due to the flow acceleration manifested by the velocity distribution along the pipe centerline plotted in Figure 20b. This is contrary to flow behavior across the orifice plane in the case of 1D spacing. Accordingly, the flow structure through the double-orifice arrangement is strongly dependent on the orifice spacing which affects not only the velocity and pressure distributions but also the total pressure drop. The effect of orifice geometry on the total pressure drop is very clear in Figure 25a and 25b where orifices with smaller diameter ratios result in much higher pressure drop.

Another interesting phenomenon is found when comparing the values of the pressure drop, Δp, between far upstream and far downstream ($x=-5D$ and $x=8D$) of the orifice plate for the two cases of double orifice with 1D spacing and D_r=0.63 (Figure 25a) and a single orifice having the same diameter ratio (Figure 22) considering the same inlet velocity, V_i=2 m/s. The obtained pressure drop in the case of double orifice was 12 kPa while reaching 15 kPa in the case of a single orifice.

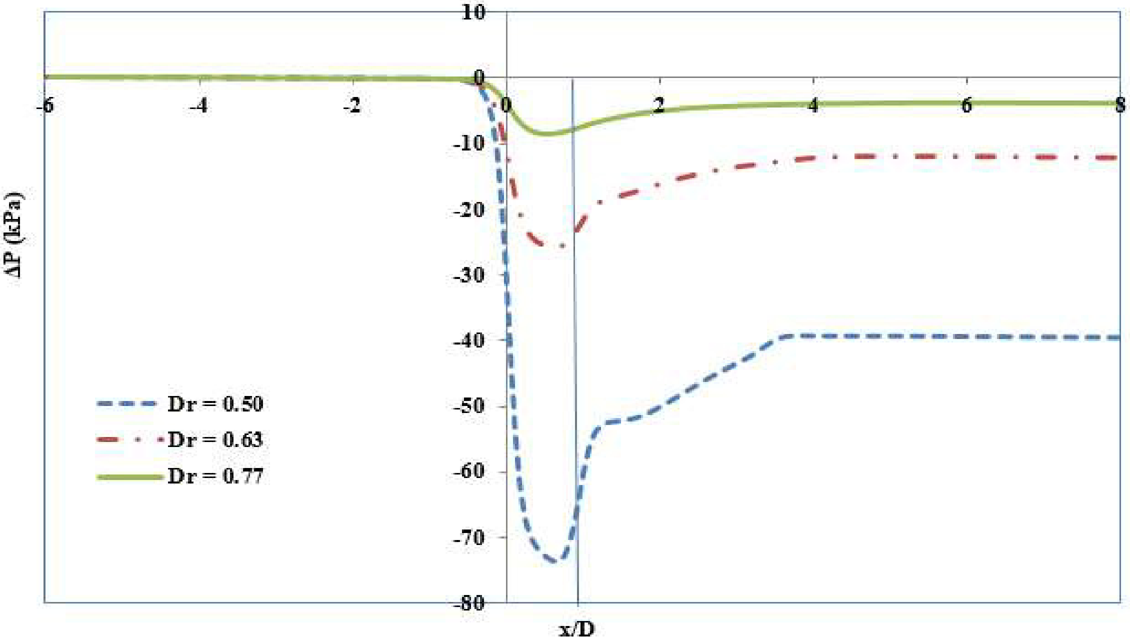

(a)

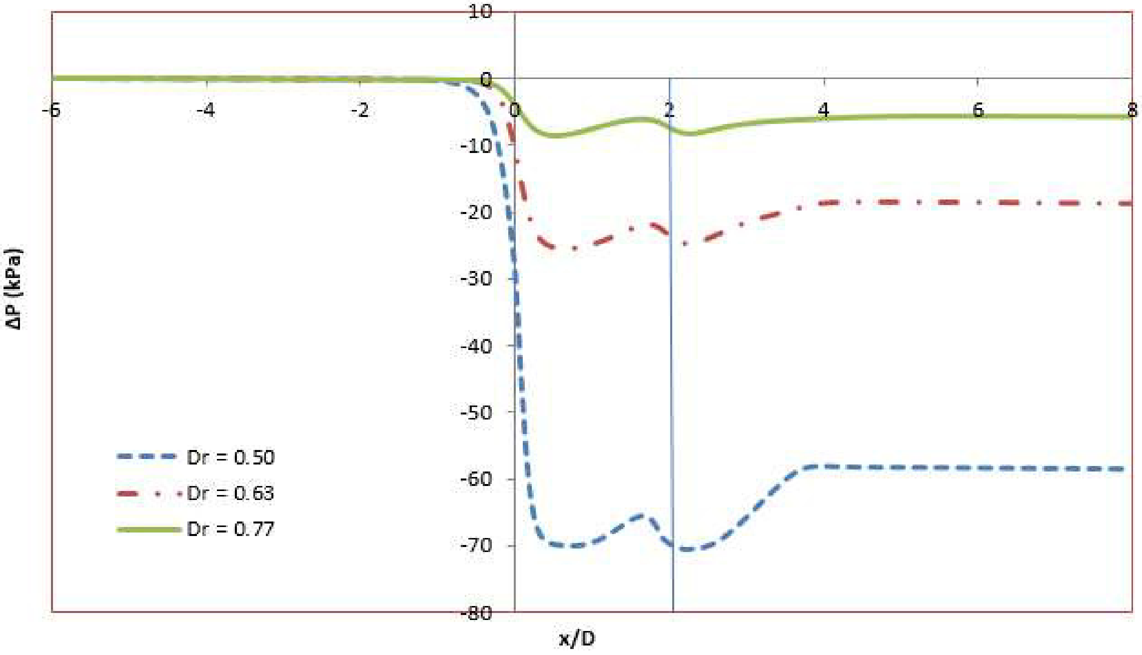

(b)

Figure 25 Variation of static pressure variation with normalized axial distance as a function of diameter ratio at V_i = 2m/s for (a) double orifice-1D-spacing (b) double orifice-2D-spacing

In this case, the indicated pressure drop is also a measure of the total hydraulic losses. This means that a double-orifice arrangement (1D spacing) results in total hydraulic losses about 20% less than that of a single orifice even though the first one has two constrictions while the second one has only one constriction. The same phenomenon prevails in the case of $D_r=0.5$where the pressure drop is 40 kPa in the case of double-orifice (1D spacing) while reaching 52 kPa in the case of a single orifice.

This indicates that the hydraulic losses in this double orifice arrangement are 23% less than that of a single orifice. The case of $D_r=0.77$ did not show a contrary result where the double orifice 1D-spacing gave a 12.5% reduction in pressure drop relative to the single orifice configuration. In order to verify the existence of this phenomenon, pressure measurements were taken for the two arrangements with $D_r=0.63$ but for a velocity of 0.555 m/s (corresponding to $Re=1.4x10^4$). Figure 26 shows the pressure variation for the two cases of a single orifice and a double orifice with 1D spacing. This figure clearly indicates the presence of the above phenomenon and also validates the accuracy of the computational model.

In an attempt to give a more rigorous explanation for the root cause of this phenomenon, a detailed investigation of the flow structure in the entire domain was conducted. The investigation starts with the analysis of the flow structure carried out by Shan et al. [10] in which they reported minimum turbulence intensities in the acceleration region upstream of the vena contracta where there is low chance of formation of vortex structures.

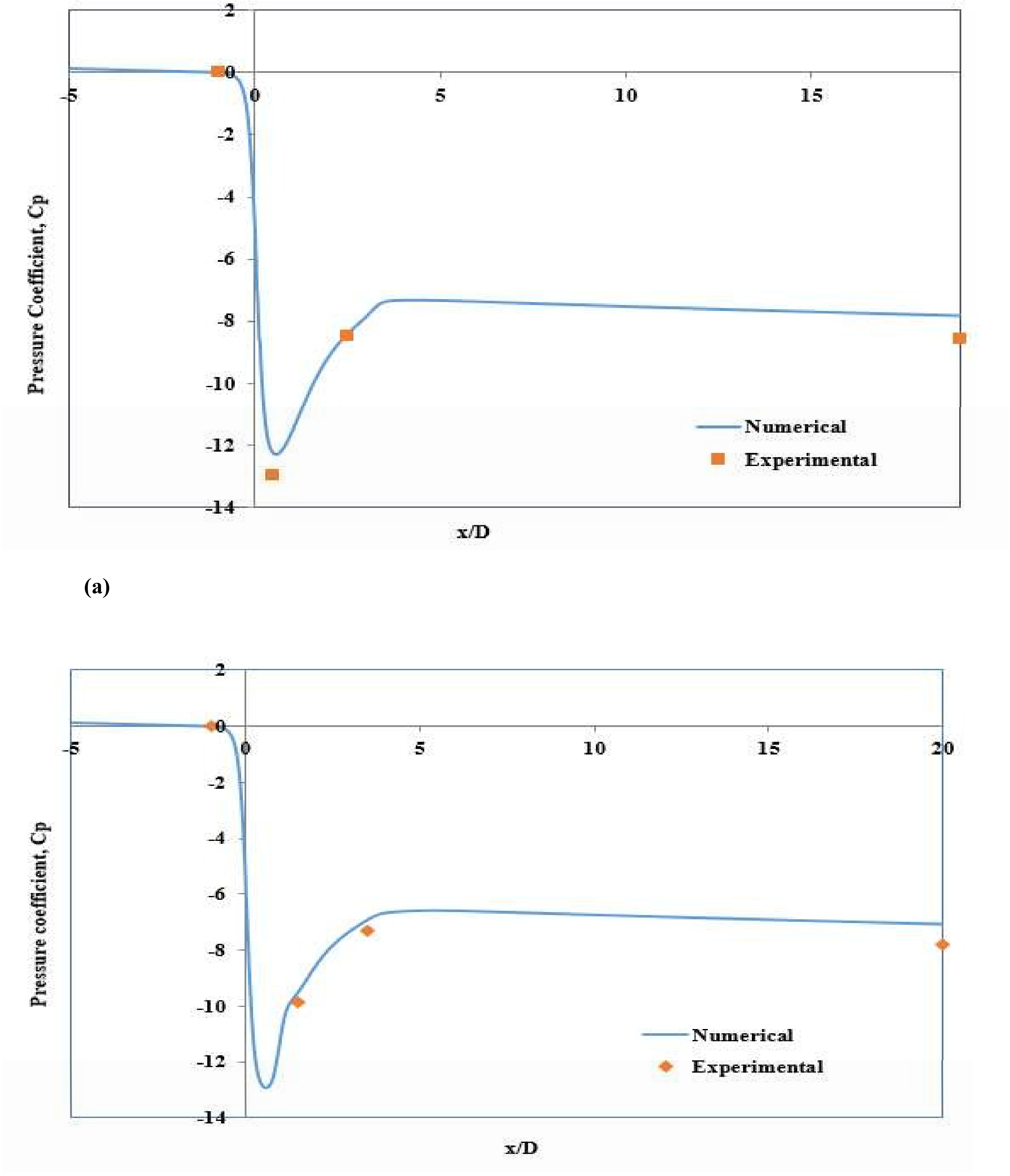

(a)

(b)

Figure 26 Comparison between computational and experimental variation of the pressure coefficient for the case of D_r=0.63, V_i=0.555 m/s; a) single orifice, and b) double orifice with 1D spacing

They also reported the presence of a shear layer that originates from the corners of the orifice throat and develops in the streamwise direction occupying the region between the core region and the recirculation zone as shown in Fig. 27. This shear layer contains vortex structures characterizing strong velocity fluctuations.

According to Shan et al.[10], the region of the shear layer between the orifice and the vena contracta constitutes vortex parings which contribute to the growth of the shear layer and as the flow moves beyond the vena contracta vortex tripling event sets in forming smaller three dimensional vortex structures rotating haphazardly. They also established the dependence of turbulence intensity and Reynolds shear stress on the unsteady vortex structures. It is believed that this vortex structures and interactions are responsible for the high turbulence intensity and Reynolds shear stress as these are more prominent and have high values in the shear layer region. Accordingly, the region between the vena contracta and reattachment zone contains vortex tripling structures causing peak vortex interactions and invariably peak turbulence intensity and Reynolds stress as reported by Shan et al. [10]. The placement of second orifice at 1D downstream the first one creates a shorter deceleration zone downstream of the second orifice causing a decrease in the resulting pressure drop (see Figures 13 and 15). Further studies are needed to establish a relationship between the orifice spacing and the total pressure drop.

The effect of flow velocity on the normalized pressure variation along the pipe axis is shown in Figure 28 for an orifice of diameter ratio D_r=0.63 and for average velocities of 1, 2 and 4 m/s considering the double-orifice arrangement with 1D and 2D spacing. The change of flow velocity reflects the change of Reynolds number, Re, in Eq. (4.2).

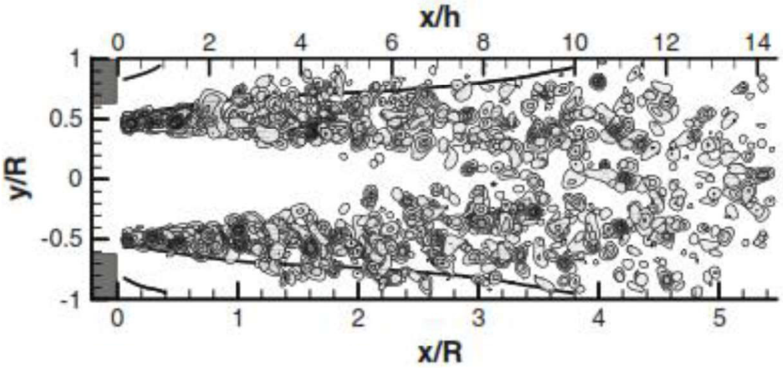

Figure 27 Schematic sketch showing the shear layer extending from the orifice edge to the reattachment zone (adapted from Shan et al.[10])

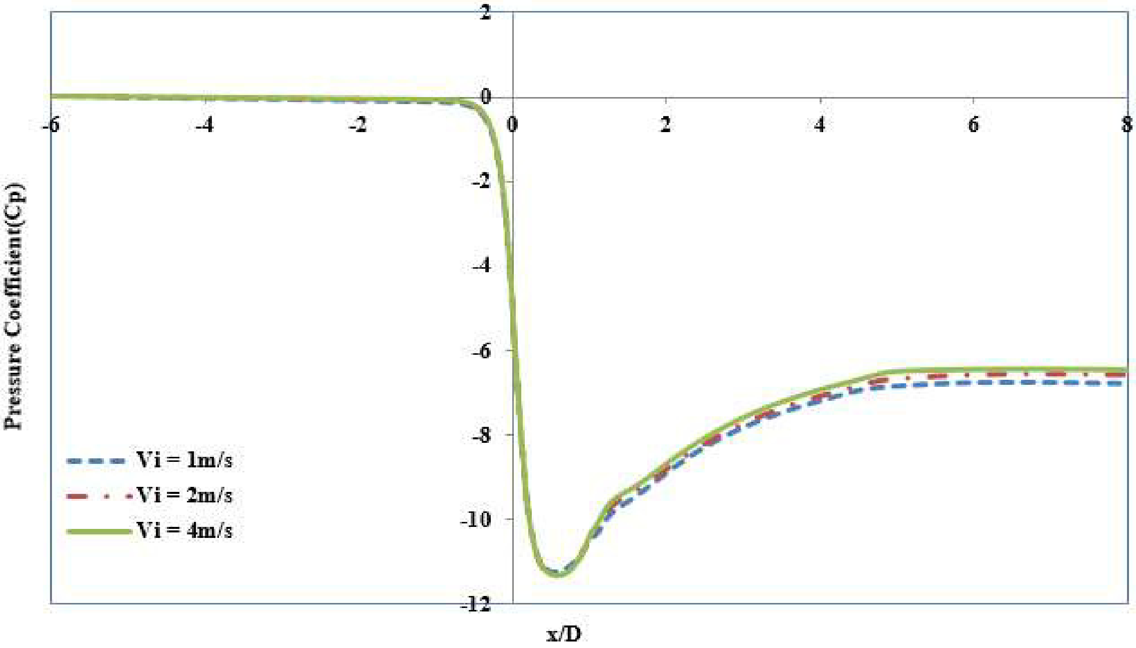

(a)

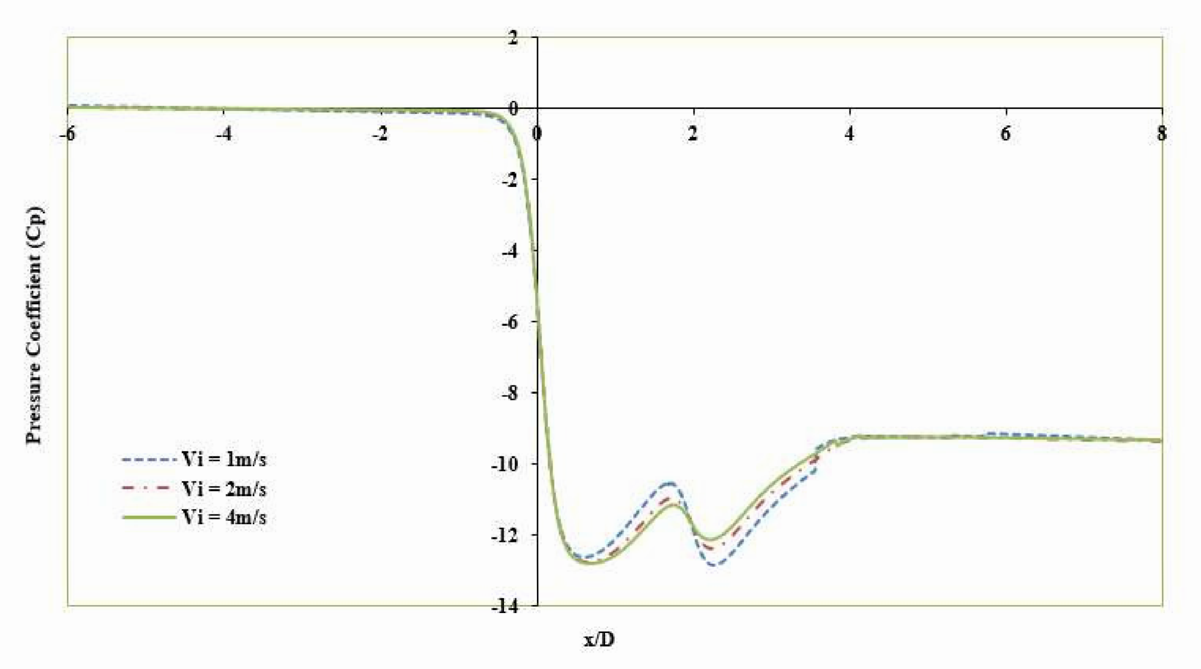

(b)

Figure 28 Variation of C_p with normalized axial distance as a function of inlet velocity for Double Orifice with $D_r = 0.63$ for (a) 1D spacing (b) 2D spacing

Figure 28a indicates insignificant effect of Re on the variation of the pressure coefficient, C_p, from the upstream boundary up to the vena contracta where the minimum pressure is attained in the case of 1D spacing.

Downstream of the vena contracta, the effect of Re is small and characterized by slightly higher pressure recovery at higher velocities. The situation in the case of 2D spacing is almost the same (no effect of Re on C_p variation) from the upstream boundary up to the first local minimum pressure occurring at the first vena contracta located downstream of the first orifice. The second local minimum pressure occurs at the second vena contracta located downstream of the second orifice and characterized by a pressure higher than that occurring at the first vena contracta. The value of C_p far downstream is almost the same for all velocities, however, the pressure drop in the case of 2D spacing is much higher than that for the 1D spacing as can be seen in Fig.28.

Figure 29 presents the effect of orifice geometry on pressure drop across single- and double-orifice arrangements for the case of D_r = 0.63. It can be seen that the minimum pressure value and position for single orifice, double orifice-1D spacing and first trough of double orifice-2D spacing are approximately the same. It is also observed that double orifice with 1D spacing gave the least pressure drop while double orifice with 2D spacing yielded the highest pressure drop. There is an approximate reduction of 23% in local pressure drop when a second orifice is placed at 1D downstream of the first compared with a single orifice. Similar trends were observed for other diameter ratios.

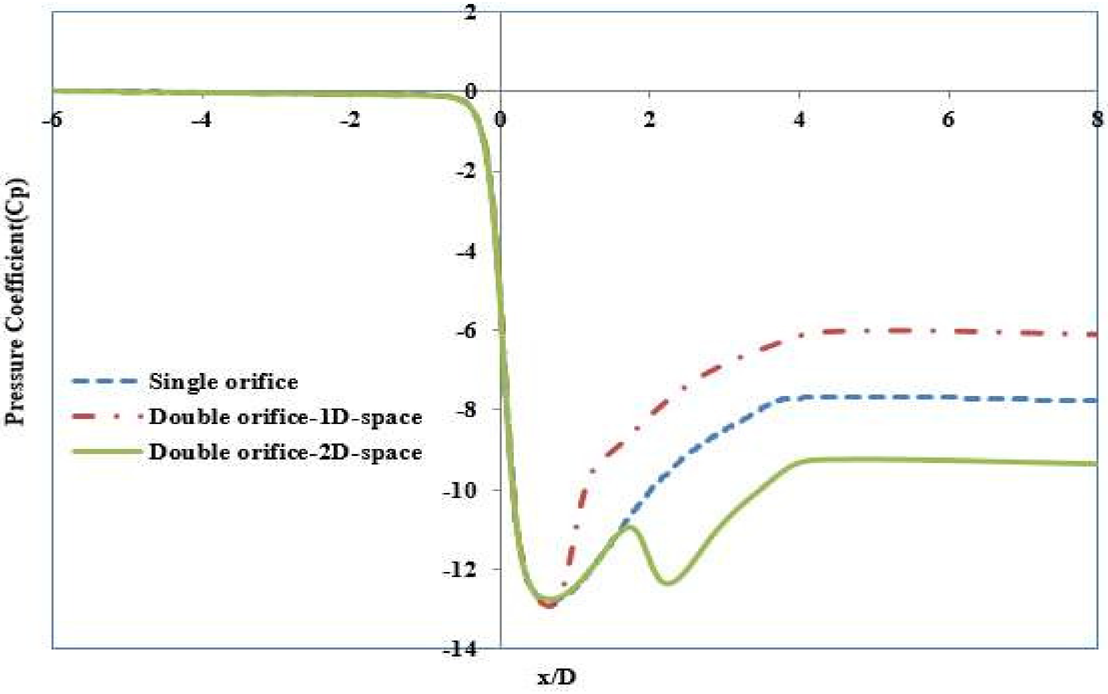

Figure 29 Variation of C_p with downstream normalized axial distance as a function of orifice geometry for D_r =0.63 and V_i = 2m/s

CHAPTER 5

EROSION IN SINGLE AND DOUBLE-ORIFICE ARRANGEMENTS

The solid particle erosion resulting from the use of double-orifice arrangement is different from that resulting from a single orifice. Effects of parameters such as flow inlet velocity, orifice diameter ratio, orifice spacing and solid particle size on erosion rates and critical erosion locations were investigated for different configurations. The solution procedure involves calculation of the flow field through one- or two-orifice arrangements, introduction of solid particles to predict their trajectories, obtain particle impact data to be used in prediction of erosion and penetration rates using semi-empirical models. The flow inlet velocity considered are 1, 2 and 4m/s, the orifice diameter ratios are 0.5, 0.63 and 0.77 while the particle diameters range from 50μm to 400μm. The pipe which is made of carbon-steel has an internal diameter of 1-inch, fluid employed is water at 20°C and the solid particles content is 2% by weight and is unchanged in all calculations.

It is well known that erosion patterns and rates are strongly dependent on the flow field characteristics (flow velocity and flow field geometry) in addition to the characteristics of the solid particles and the impacted surface. In this study, the erosion prediction was obtained using two computational models in addition to erosion empirical correlations. The first is the continuous phase model used for predicting the flow velocity field and the second is the Lagrangian particle-tracking model used for the determination of particle trajectories and particle impact data. The Lagrangian particle-tracking model is based on a one-way flow-to-particle coupling approach that can be used in case of low particle intensity. For a single-orifice configuration, the flow in the upstream side accelerates as it approaches the orifice opening by contraction process due to change in flow area as presented in Fig. 13 forming a nozzle-shaped stream tube. The shape of this stream tube is strongly dependent on the orifice diameter ratio. Due to the sharp curvature of the streamlines upstream of the orifice, the area contraction of the stream tube continues until reaching the minimum area at the vena contracta on the downstream side of the orifice at which the velocity reaches its maximum and the pressure reaches its minimum.

The recirculation region formed adjacent to the orifice in the downstream is driven by the high velocity in the core region and characterized by low velocity at its center. In theory, the fluid in this region keeps circulating and never gets entrained to the main stream. Downstream the vena contracta, the flow forms a diffuser-shaped stream tube in which the flow decelerates and reattaches to the confining wall further downstream as shown in Fig. 13.

In the double-orifice arrangement, the detailed features of the flow field were found to have a strong dependence not only on the orifice diameter ratio but also on the orifice spacing. On the other hand, the dimensionless pressure variations were found to have little dependence on the flow Reynolds number. One important feature of relevance to the erosion process is the recirculating flow region in the spacing between the two orifices that is characterized by low velocity in the outer wall region and a jet-like flow in the core region (Figure 15). Moreover, the recirculation and reattachment regions downstream of the second orifice differ from those downstream of a single orifice (Figures 13 and 15).

The computational details of the flow field characteristics and its dependence on various parameters were presented and discussed in Chapter 4.

The determination of erosion rates involves the use of erosion models in determining the motion of solid particles. The particles are tracked from the location of their release at the pipe inlet till they are discharged through the exit section. Figure 30 presents the particles' trajectories in the three configurations considered (single orifice, double orifice with 1D spacing, double orifice with 2D spacing) for case of $D_r = 0.63$, $V_i = 2$ m/s and $D_p = 100\mu m$. Studies by Nemitallah et al. [15] showed that larger percentage of particles make several impingements on pipe and orifice walls while a very few makes little or no contact with the walls. The figure representing single orifice flow shows the possible impingement on the wall by few particles in the recirculation zone and the deflection of the majority further downstream to the wall in the reattachment zone.

It can be observed that no particles impacted the pipe wall in the spacing between the two orifices in the double-orifice arrangement with 1D-spacing as shown in Figure 30b.On the other hand, the particle trajectories in the case of 2D spacing shown in Figure 30c indicates the presence of a small number of particles in the recirculating zone near the pipe wall. Some of these particles have impingements on the wall at low speeds and very small impact angles while some others are trapped and keep circulating in the recirculation zone without being entrained to the main stream. The particle trajectories downstream the second orifices in both double-orifice configurations have some similarity to that of single orifice flow. However, the location of the reattachment zone downstream of the second orifice differs from one case to another and that will cause a difference in the erosion pattern. The particle trajectories shown in Figures 30b and 30c indicate the presence of particle impacts with different intensity in the flow recirculation and reattachment zones downstream of the second orifice in both double-orifice configurations.

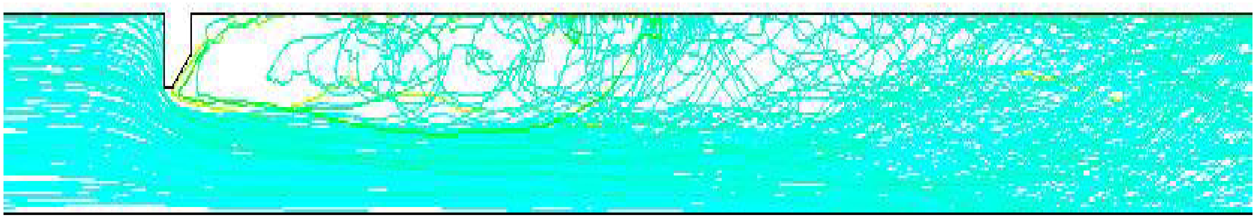

a) Single Orifice

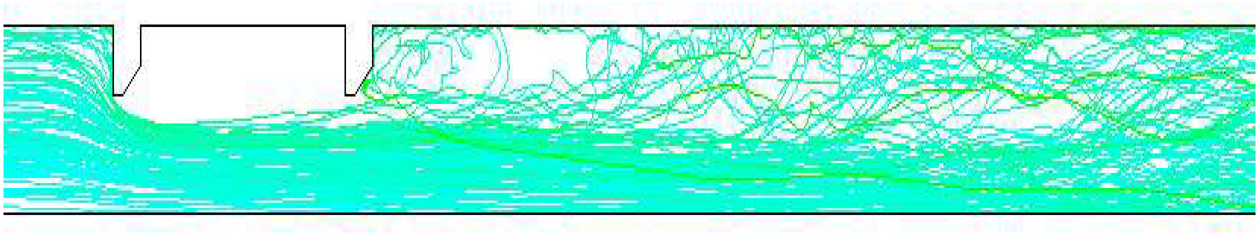

b) Double-orifice with 1D spacing

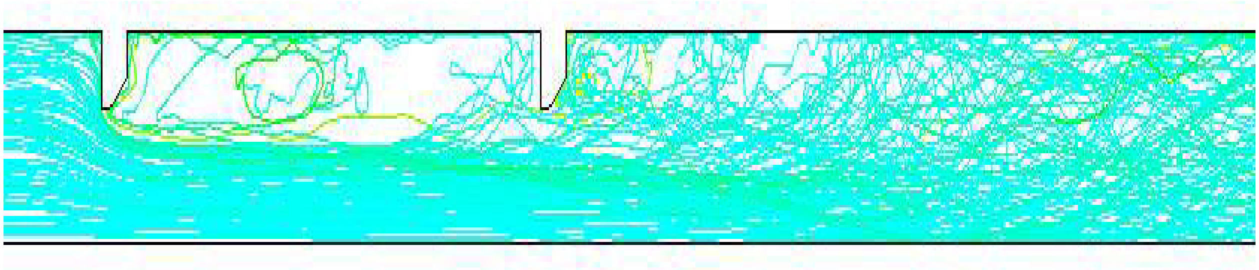

c) Double-orifice with 2D spacing

Figure 30 Solid particle trajectories for case Dr= 0.63, Dp= 100µm and Vi = 2m/s for the three configurations; a) Single Orifice, b) Double-orifice with 1D spacing, and c) Double-orifice with 2D spacing

The calculation of the local erosion rate on the pipe wall per unit mass of particles is based on Eqs. (3-16) and (3-17) that takes into consideration the effects of particle impact velocity, impact angle, type of solid particle and solid surface properties. The cumulative effect of erosion per unit surface area is termed the erosion rate it is measured by the amount of material removed per unit wall area per unit time. The discussion in this study is focused on erosion rates downstream a single orifice and downstream the second orifice in the double-orifice arrangement considering the effects of inlet flow velocity, solid particle size, orifice diameter ratio and orifice spacing.

The local erosion rate in the downstream side of a single orifice for the case $D_r = 0.63$, $V_i = 2$m/s, and solid particle diameter, $D_p = 100\mu$m, is shown in Fig.31a. It can be seen that the rate of erosion increases steeply from the leeward face of the orifice and attains a first local maximum value of approximately 6.48×10^{-7} kg/m^{2}s at a distance of x = 0.8D before descending sharply. A second local erosion peak of 1.96×10^{-6} kg/m^{2}s occurs at x = 5.5D further downstream. Far downstream (x>15D), the erosion rate becomes very small (less than 2.05×10^{-7} kg/m^{2}s). The first erosion peak is located in the primary recirculation zone despite the prevailing low flow velocity (Fig.13). To explain this phenomenon, the variation of the particle concentration and turbulence kinetic energy (TKE) in the near-wall region were plotted in Figure 32.

The figure shows high particle concentration coupled with high TKE in the first peak region. Both effects lead to higher rate of particles impacting the pipe surface in that region, thus creating the first peak. The second erosion peak occurs in the reattachment zone which is characterized by streamlines with large curvature and higher velocity near the pipe wall (compared to the low velocities in the recirculation zone).This large curvature causes a deviation between the particle trajectory and the flow streamlines due to the difference in inertial forces between fluid and solid particles. This deviation causes a high rate of solid particle impingement and accordingly higher rate of erosion in the reattachment zone.

Figure 31b & 31c shows the variation of erosion rate on the pipe wall downstream the second orifice in the double-orifice arrangement with 1D and 2D spacing respectively. For the case of 1D spacing, Figure 31b shows an erosion rate profile downstream of the second orifice similar in trend to that of a single orifice (i.e. having two local peaks and a crest in between) but differs quantitatively. The figure also shows that the location of the first erosion peak in the recirculation zone is closer to the second orifice compared with its location in the single orifice configuration. This is mainly because of the shorter recirculation zone downstream the second orifice compared to that in the single orifice configuration (Figure 15). The higher rate of erosion in this zone is attributed to the increased particle concentration and TKE as in the case of single-orifice arrangement.

It is also clear from Figures 31a & b that the maximum erosion rate (occurring in the reattachment zone) is much lower (about 40% less) in the double-orifice arrangement with 1D spacing than that of a single orifice. The first and second erosion peaks are located at approximately at distances of 0.96D and 5D downstream the second orifice, respectively. In the case of 2D spacing, the two erosion peaks are located at distances of 0.5D and 4D downstream of the second orifice, however, the maximum erosion rate is about 25% higher than the case of a single orifice. The trough between the two peaks represents erosion in the region between the recirculation and reattachment zones with magnitude similar to erosion rate downstream the second peak. Subsequent discussions will be on dependence of erosion rates in the three configurations on parameters such as inlet flow velocity, particle sizes, orifice diameter ratio and orifice configurations.

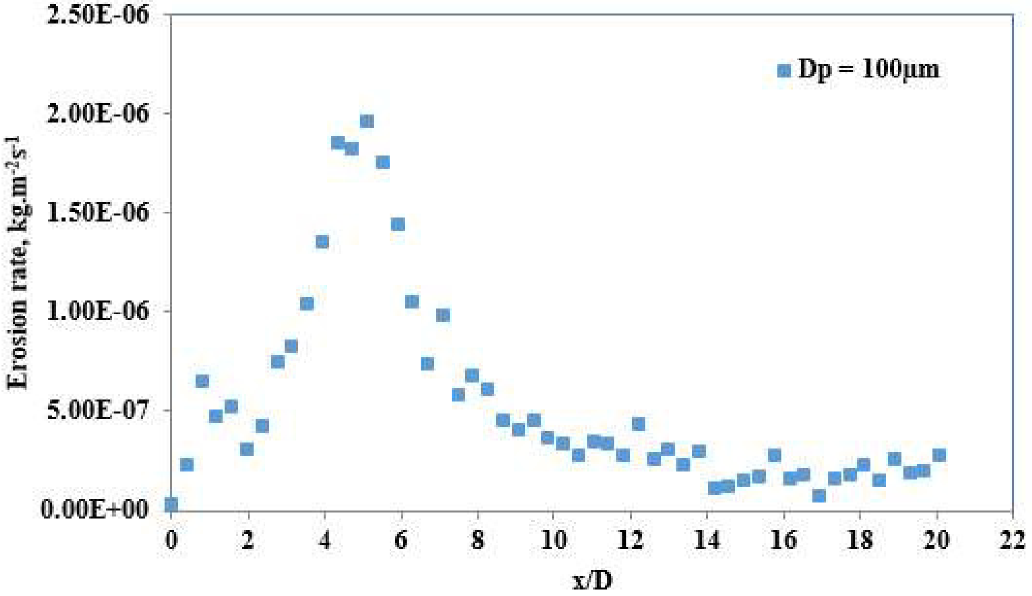

(a)

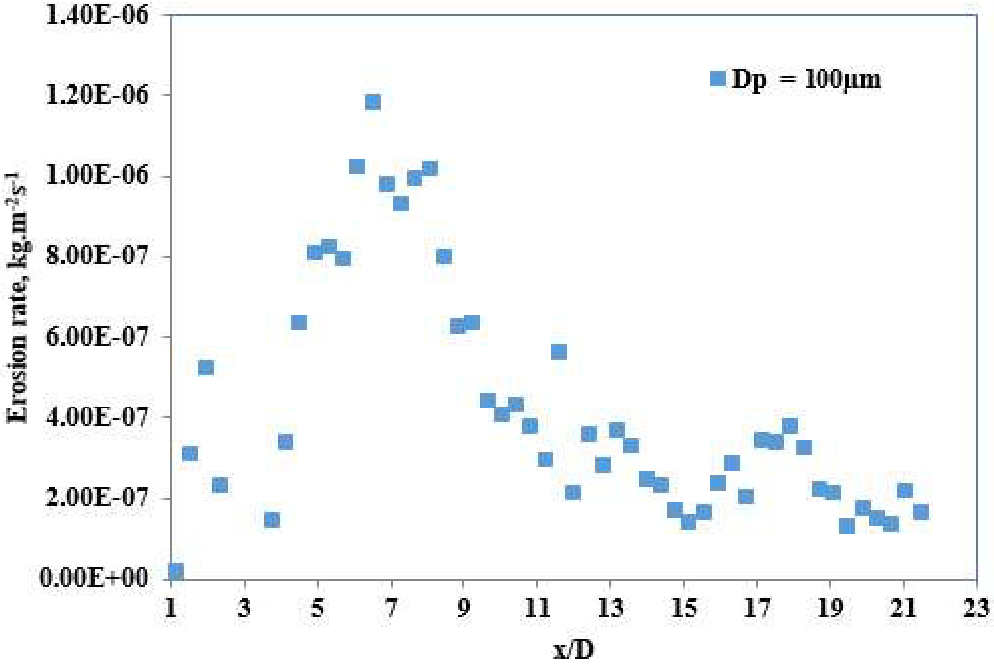

(b)

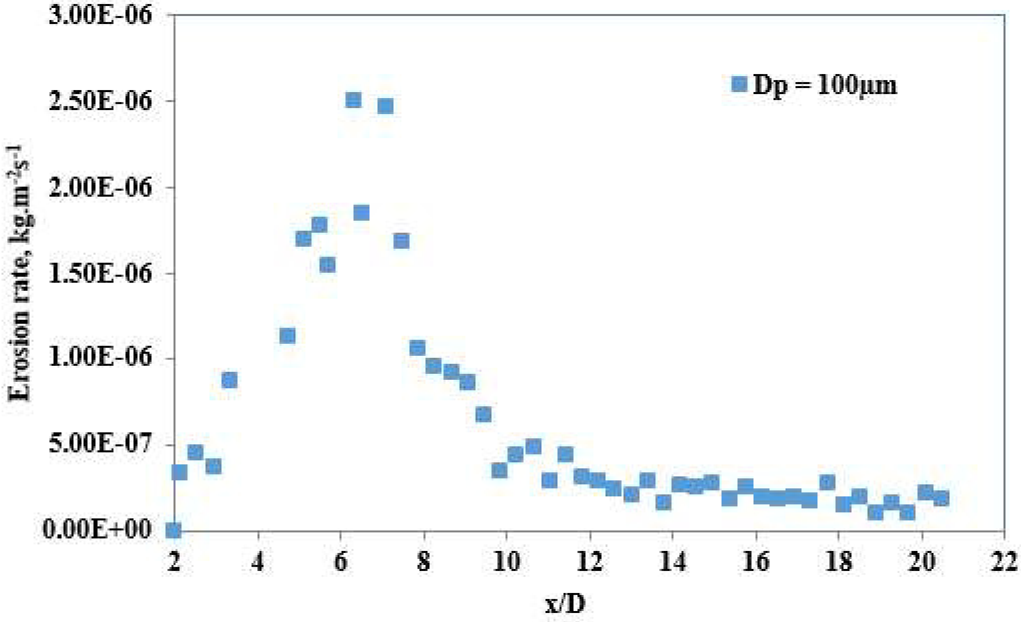

(c)

Figure 31 Erosion rates downstream orifice for case of Dr = 0.63, Vi = 2 m/s and Dp = 100µm; a) Single orifice, b) Double orifice-1D-separation, and c) Double orifice-2D-separation

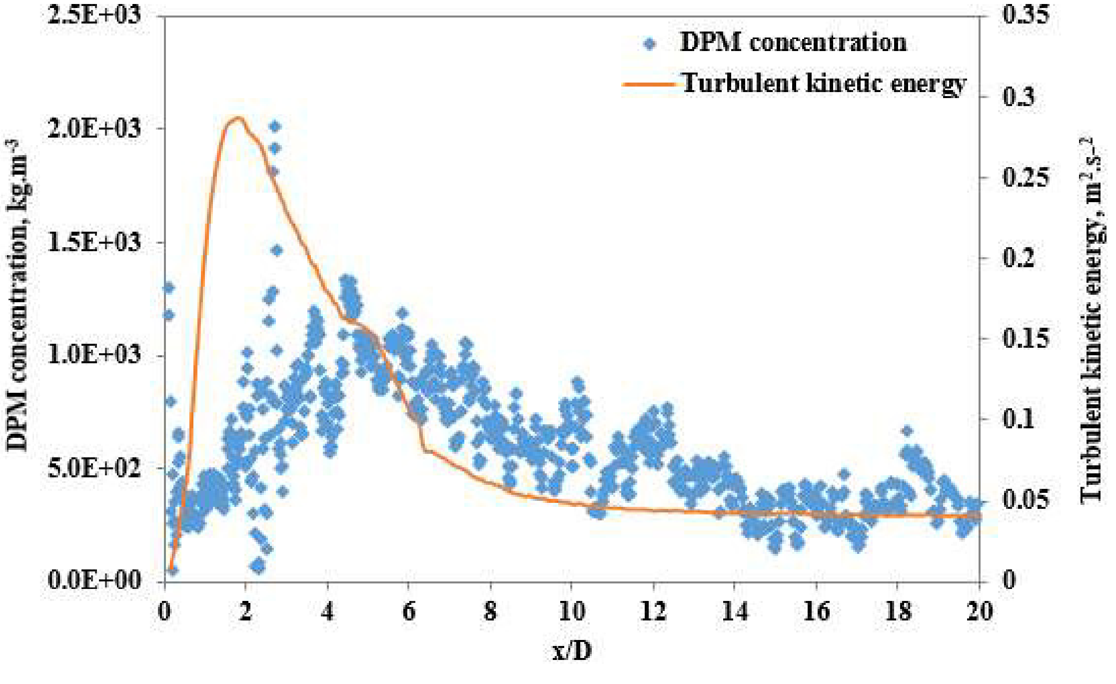

Figure 32 Downstream profile of solid particle concentration and turbulent kinetic energy for single orifice; case of D_r = 0.63, V_i = 2 m/s and D_p = 100µm

5.1 Effects of Flow Velocity on Erosion Rates

Figure 33a shows the effect of flow inlet velocity on erosion rate for the case of $D_r = 0.63$, $D_p = 100\mu m$ at flow velocities V_i = 1m/s, 2m/s and 4m/s in single orifice arrangement. It is observed that the profile of erosion rate has the same features of two peaks at all velocities (as described earlier in the case of V_i = 2 m/s) but the erosion rate varies. The magnitude of erosion rate over the whole length downstream orifice increases as the velocity increases with the maximum occurring in the reattachment zone. The figure indicates insignificant erosion occurring at the low velocity of 1 m/s. The erosion becomes appreciable as the flow velocity increases to 2 m/s reaching $2x10^{-6}$ kg/m^{2}s while significant increase occurs at a velocity of 4 m/s reaching $1.25x10^{-5}$ kg/m^{2}s.

In the case of double-orifice arrangement, the rate of erosion in the space between the two orifices is negligibly small and that explains the absence of that region in the present discussion. Figure 33b shows the erosion rate downstream of the second orifice for the same three flow velocities in the case of 1D orifice spacing. The variation of the erosion rate is qualitatively similar to that occurring downstream of a single orifice but at reduced values. The maximum erosion rate at a velocity of 4 m/s reached approximately $9.25x10^{-6}$ kg/m^{2}s which is 25% less than that for a single orifice. However, the 2D spacing resulted in a maximum erosion rate at a velocity of 4 m/s approximately the same as that occurred in the case of a single orifice (Figure 33c). The changes in the maximum erosion rate for the same inlet flow velocity in different orifice configurations may be attributed to changes in the streamline curvature in the reattachment zone resulting in different particle impact angles.

The particle impact velocity in the reattachment region may not slightly be different in different orifice configurations. Figures 33a,b,c also indicate higher erosion rate in the recirculation zone downstream of the second orifice (or first orifice in single orifice configuration) with the increase in the inlet flow velocity. This is attributed to the increase in turbulent kinetic energy with increasing inlet velocity which leads to significant rise in frequency of particle impingement.

Figures 34 show the effect of inlet flow velocity on the maximum erosion rate for the three different configurations of single orifice, double-orifice with 1D and 2D spacing for the three diameter ratios of 0.5, 0.63 and 0.77 and solid particle size of 100μm. Figure 34a shows the effect of flow velocity on the maximum erosion rate in the three orifice arrangements keeping the diameter ratio (D_r=0.5) unchanged. Similarly, Figures 34b and 34c show the same effect for diameter ratios of 0.63 and 0.77, respectively. It is clear from the figures that the maximum erosion rate increases as the flow inlet velocity increases for all orifice diameter ratios. On the other hand, there is little difference between the maximum erosion rate observed in single orifice and double-orifice with 2D spacing.

However, the case of double-orifice with 1D spacing showed a remarkable reduction in maximum erosion rate. The results indicated an average reduction by 32%, 28% and 24.5% in the maximum erosion rate (compared to single orifice configuration) in the case of double-orifice with 1D spacing for the three diameter ratios of 0.5, 0.63 and 0.77, respectively. This implies that this configuration (1D spacing) results not only in less hydraulic losses (as discussed in Chapter 4) but also less erosion in comparison with the single orifice configuration.

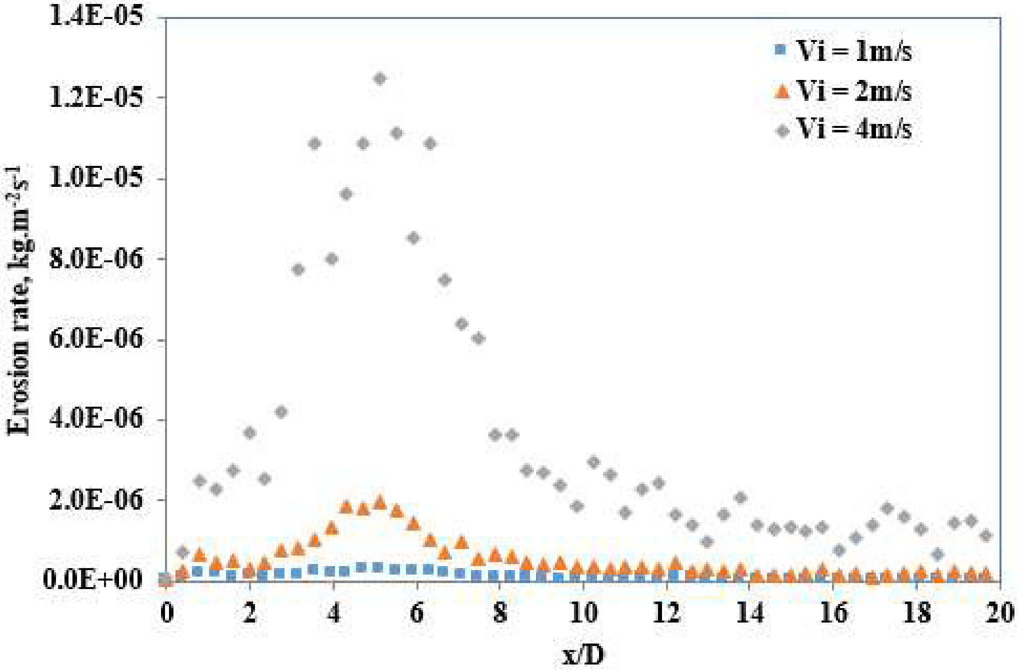

Erosion rate, kg.m^{-2}s^{-1}
1.4E-05
1.2E-05
1.0E-05
8.0E-06
6.0E-06
4.0E-06
2.0E-06
0.0E+00
0
2
4
6
8
10
12
14
16
18
20
x/D
Vi = 1m/s
Vi = 2m/s
Vi = 4m/s

(a)

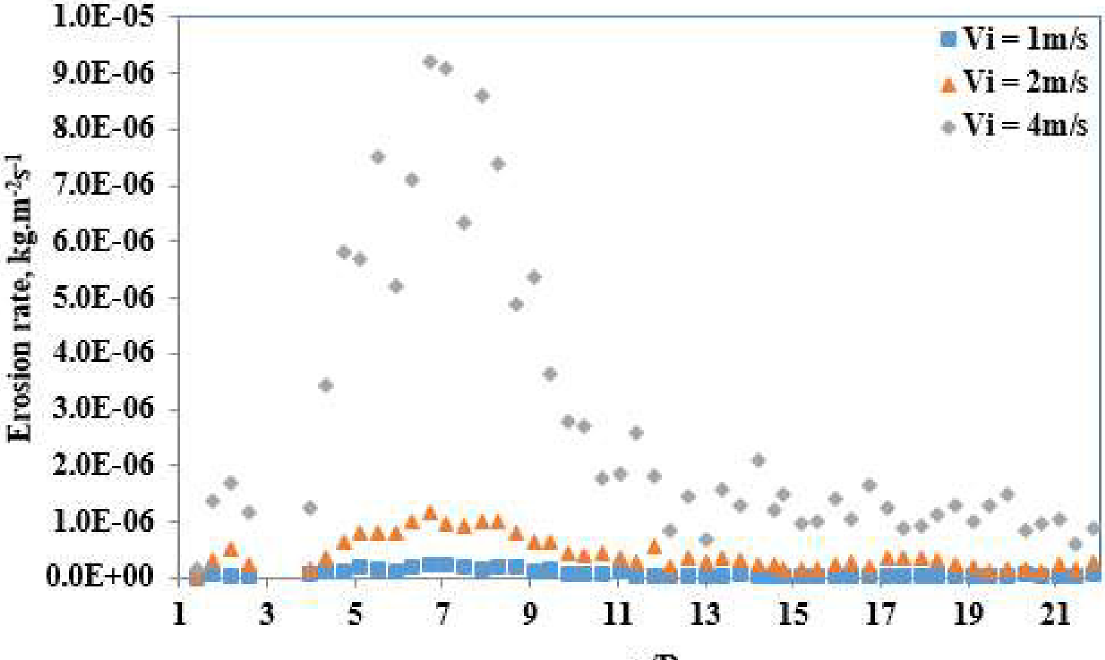

Erosion rate, kg.m^{-2}s^{-1}
1.0E-05
9.0E-06
8.0E-06
7.0E-06
6.0E-06
5.0E-06
4.0E-06
3.0E-06
2.0E-06
1.0E-06
0.0E+00
1
3
5
7
9
11
13
15
17
19
21
x/D
Vi = 1m/s
Vi = 2m/s
Vi = 4m/s

(b)

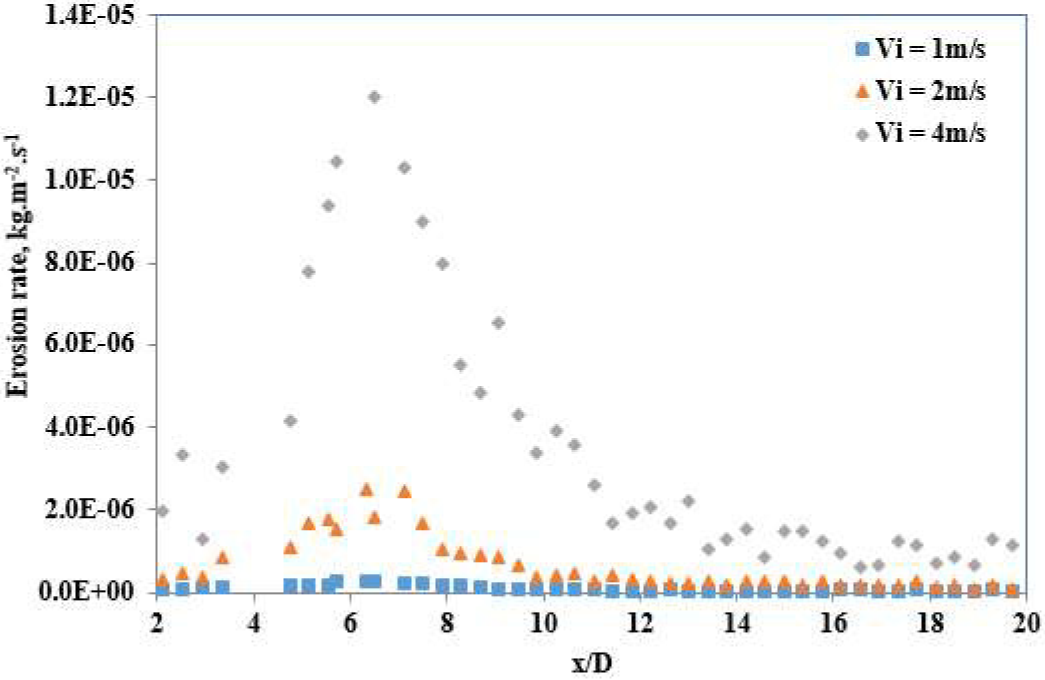

(c)

Figure 33 Effect of flow velocity on erosion rate downstream the orifice for the case of $D_r = 0.63$ and $D_p = 100\mu m$; a) Single orifice, b) Double orifice with 1D spacing, and c) Double orifice with 2D spacing

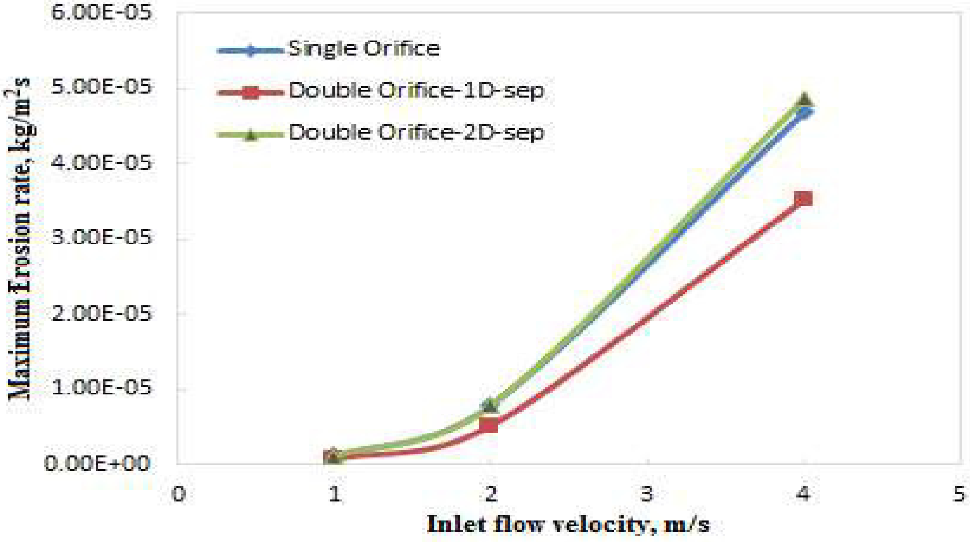

(a)

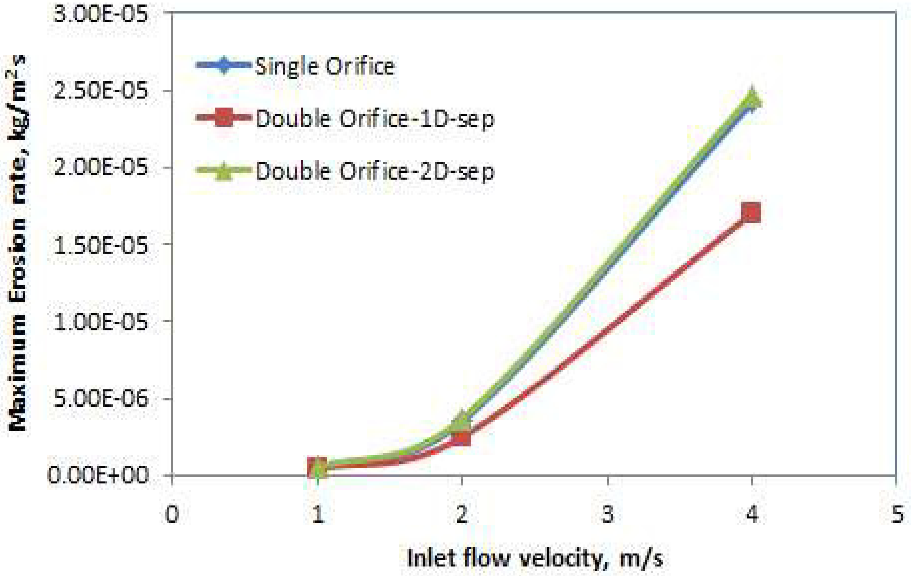

(b)

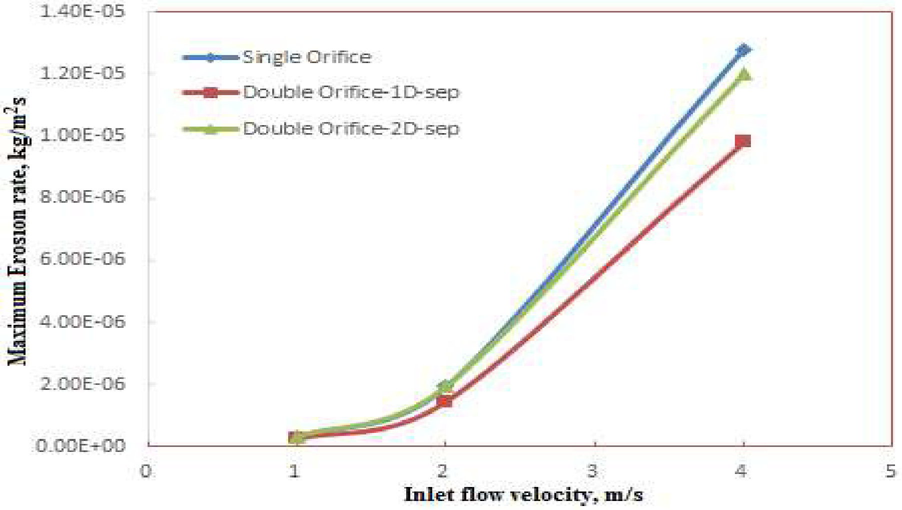

(c)

Figure 34 Comparison of the effects of inlet flow velocity on maximum erosion rate in the orifice configurations considering a solid particle size D_p=100µm and orifice diameter ratios of a) D_r=0.5, b) D_r=0.63 and c) D_r=0.77

5.2 Effects of Solid Particle Size on Erosion Rates

One of the important factors to be considered in the study of erosion in pipes is the effect of solid particle size. This study investigates solid particles sizes in the range 50µm - 400µm while keeping the solid particle content unchanged (2% by weight). The variation of erosion rate with particle diameters in single orifice flow is illustrated in Fig.35a for $D_r = 0.63$, and $V_i = 2$m/s. It can be seen that the maximum local erosion rate decreases with increasing particle size resulting in highest erosion rate for particles of diameter 50µm and lowest rate for 400µm particles. This erosion rate-particle diameter relationship was also observed for $V_i = 1$m/s and 4m/s. It should be pointed out that the number of particles with smaller diameter is much higher than that for large particles based on 2% loading by weight. For example, the number of 50µm particles is 512 times the number of 400µm particles.

Accordingly, the number of particle impingements is much higher in the case of small particles. Also, the particle size has a strong influence on its trajectory, impact location, impact angle and impact velocity as discussed in the works by [29]–[31]. On the other hand, erosion in the recirculation zone is dependent on the turbulence kinetic energy (TKE) and particle concentration. However, TKE is independent of particle size based on the assumption of low particle loading and one-way interaction. Therefore, the reduction in erosion rate with increasing particle size in the recirculation zone is highly dependent on particle concentration.

The variation of erosion rate with particle size and the characteristics of the erosion pattern downstream the second orifice in double-orifice configuration are similar to that of a single orifice as shown in Figs.35b & 35c. Features of erosion variation such as peak erosion rates at the recirculation and reattachment zones are similar qualitatively for all particle sizes considered. The erosion rate in the recirculation zone increases as D_p decreases. This relation can be attributed to the large surface area to size ratio of particles with smaller diameters which makes their motion more aligned with the fluid flow(i.e. the ratio of drag force to inertia force is high for smaller particles). Likewise the rate of erosion in the reattachment zone increases with decreasing particle size. Although the deviation of particle trajectory from fluid streamline increases with increasing particle diameter, the highly turbulent nature of the flow in the reattachment zone accounts for the relatively high impingement rate by smaller particles.

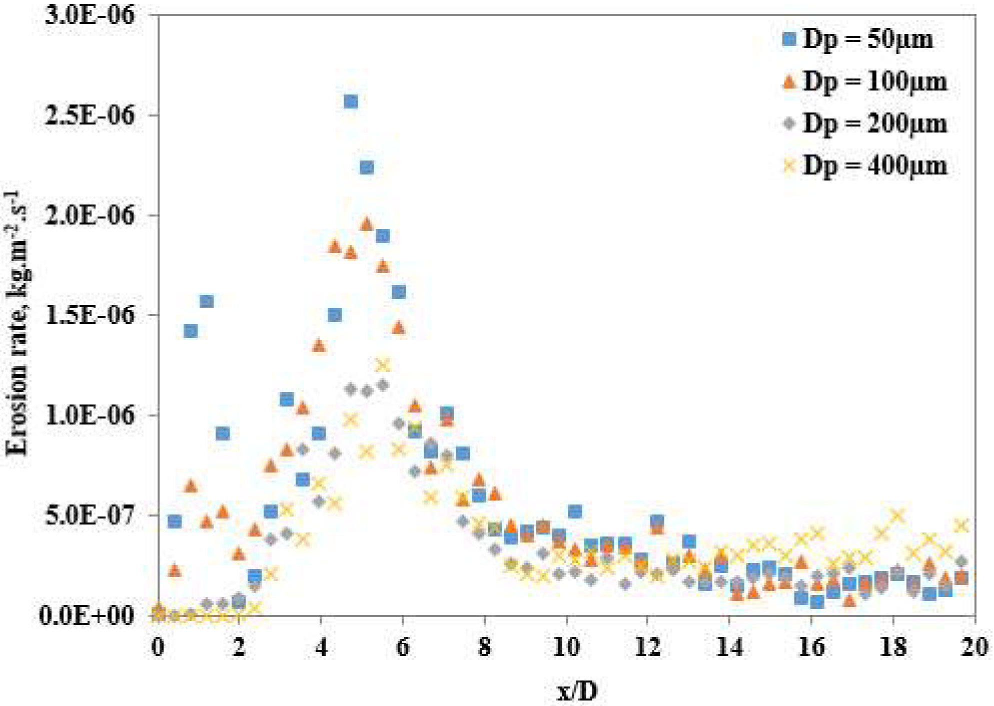

(a)

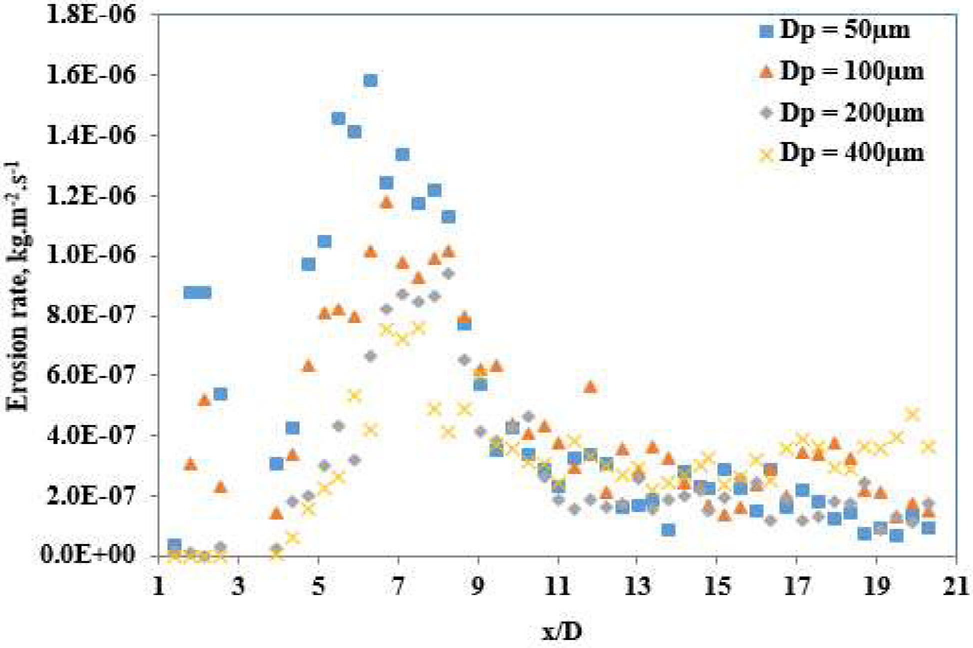

(b)

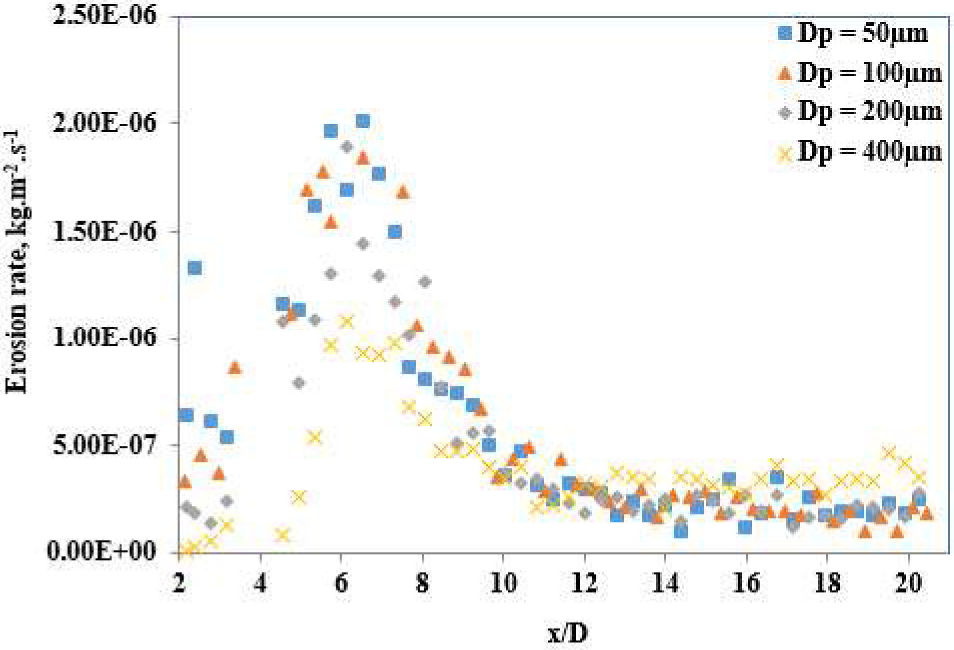

(c)

Figure 35 Effect of particle size on the erosion rate downstream of the orifice for the case of D_r = 0.63, Vi = 2 m/s; a) Single orifice, b) Double-orifice with 1D spacing, and c) Double-orifice with 2D spacing

5.3 Effects of Orifice Diameter Ratio on Erosion Rates

Erosion rates are greatly influenced by the orifice geometry. Figure 36a shows the downstream wall erosion rate profile for a single orifice at V_i = 2m/s for the three diameter ratios of 0.5, 0.63 and 0.77 using solid particles of diameter D_p = 100μm. It can be seen that the erosion patterns for the different diameter ratios considered are relatively similar in terms of having two local peaks and average erosion rate in other flow regions. Although the particles volume introduced is the same for the diameter ratios considered at a certain inlet velocity and particle size, the erosion rates at the peak regions decreases as orifice D_r increases. This is because the particle concentration in the recirculation and reattachment zones varies increases with decreasing the diameter ratio.

The variation of first local erosion peak in the recirculation region with diameter ratio can be related to larger recirculation zone and higher velocities produced by smaller diameter ratio. Moreover, the maximum TKE in the recirculation zone varies as downstream velocity increases with decreasing diameter ratios at the same inlet flow velocity. Invariably, this leads to increased effective impacts by the particles thereby resulting in higher erosion rate for smaller diameter ratios. The second local erosion peak increases with decreasing diameter ratio because of the higher velocities in the downstream side of the orifice and also larger curvature of streamlines associated with smaller diameter ratios. This brings about more deviation of particle trajectories from the flow streamline thereby causing more impingements on the pipe wall.

The effects of varying diameter ratio on erosion rates downstream the second orifice in double orifices with 1D and 2D spacing are presented in Figs. 36b, c respectively. It can be seen that the erosion rate profiles are similar to that observed in case of single orifice.

The profiles have two peaks at the recirculation and reattachment zones but varies quantitatively amongst the three configurations. Also, the magnitude of peak erosion rates decreases with increasing orifice diameter ratio. This can be attributed to the bigger recirculation, more particle concentration and greater TKE in the recirculation zone and high curvature of streamlines related to smaller diameter ratios.

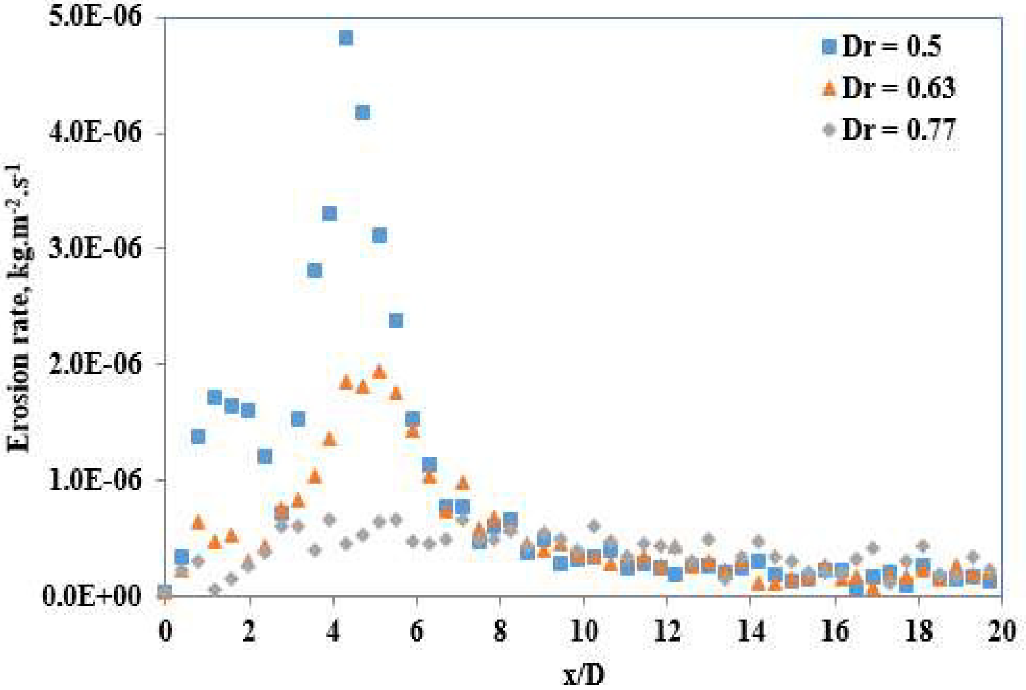

(a)

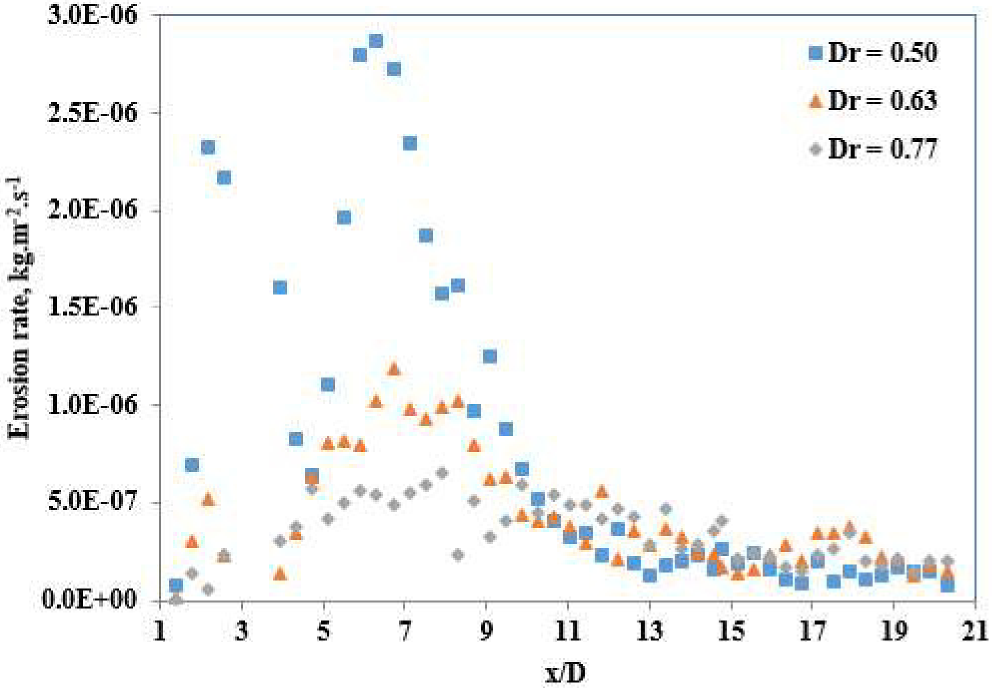

(b)

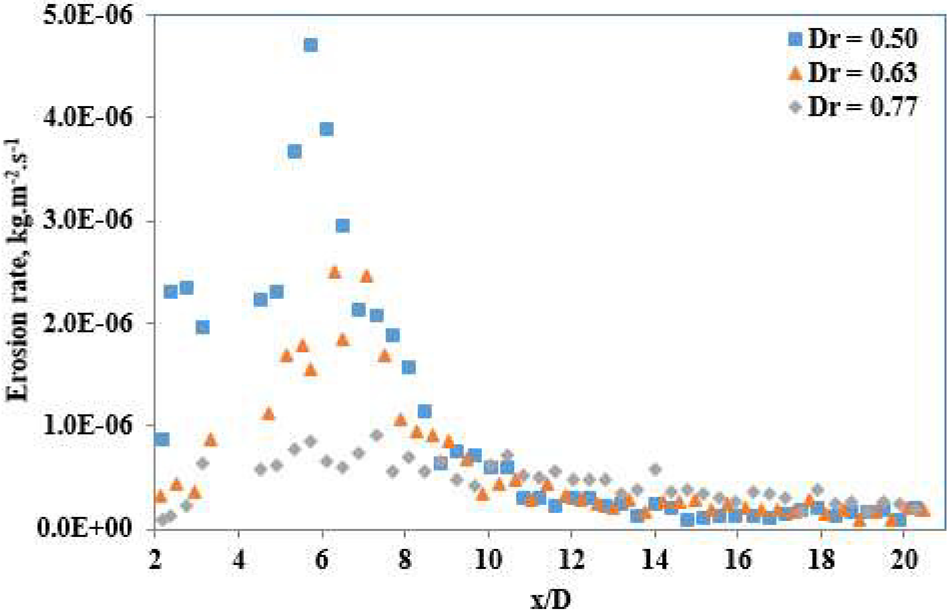

(c)

Figure 36 Effect of orifice diameter ratio on erosion pattern for an inlet velocity of 2 m/s and solid particles of diameter100μm; a) Single orifice, b) Double-orifice with 1D spacing, and c) Double-orifice with 2D spacing

5.4 Effects of Flow Velocity and Particle Size on Erosion Rates in the Spacing between the Two Orifices

Erosion rates on the wall region separating the two orifices in both double orifice configurations are presented in this section. Figures 37a, b shows the variation of erosion rate in this region with the increase of inlet velocity for the case of $D_r = 0.63$ and $D_p = 100\mu m$considering 1D and 2D spacing, respectively. It is observed that zero erosion rate was recorded for 1D separation at higher inlet velocities of 2 m/s and 4 m/s. in the case of V_i =1 m/s, erosion at a very small rate occurred on the pipe wall between the two orifices. This observation antagonizes our earlier submission that erosion rate increases with increasing inlet velocity. Although the magnitudes of velocity and TKE are high behind the first orifice, the particle concentration at this region decreases as velocity increases. The negligible presence of particles in this region at high velocities results to insignificant erosion. This is also evident in the particle trajectory plot colored by particle residence time for this case shown in Fig.30b, where there was negligible particle in this wall region. This may be due to increased curvature of streamlines associated with higher velocities which deflects the particles towards the centerline.

In the case of 2D spacing presented in Fig.37b,erosion occurred at the pipe wall for all velocities considered but the magnitude of erosion rate is much less than that occurred downstream of the second orifice. The 2D spacing allows the formation of a longer circulating flow cell behind the first orifice and as such, some particles are trapped therein. This region is also characterized with high velocity and invariably high TKE. The trend of erosion rate shows increasing erosion rate as the flow approaches the second orifice.

Figures 38a and 38b shows the effect of particle size on the erosion rate pattern in the spacing between the two orifices for the case of Vi= 2 m/s, Dr= 0.63 considering double-orifice arrangement with 1D and 2D spacing, respectively. The erosion rate profile for double orifice with 1D spacing (Fig.38a) shows that erosion occurred in the space between the two orifices only for smallest particles (50µm diameter) while larger particles (D_p=100µm, 200µm and 400µm) yielded zero erosion. This is attributed to the absence of large particles in the wall region as manifested by the solid particle trajectories shown in Fig.30b. Such absence is caused by the high inertia of such particles which gets entrained in the main stream (almost straight streamlines) through the orifice opening. The erosion rate pattern in the space between the two orifices in the case of 2D spacing (Fig.38b) depicts the occurrence of erosion for particle diameters of 50µm-200µm while particles with the largest diameter of 400µm caused insignificant erosion. It is also observed that for the smaller particle diameter range causing erosion, the erosion rate decreases as the particle diameter increases with more erosion occurring close to the second orifice. In general, the erosion in the spacing between the two orifices is negligibly small in comparison with erosion in the reattachment zone downstream of the second orifice.

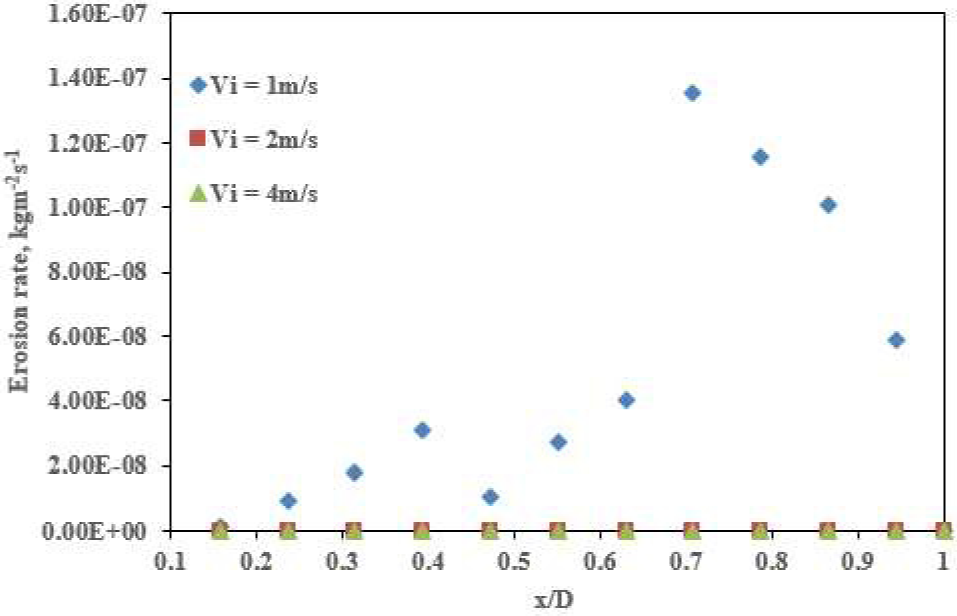

(a)

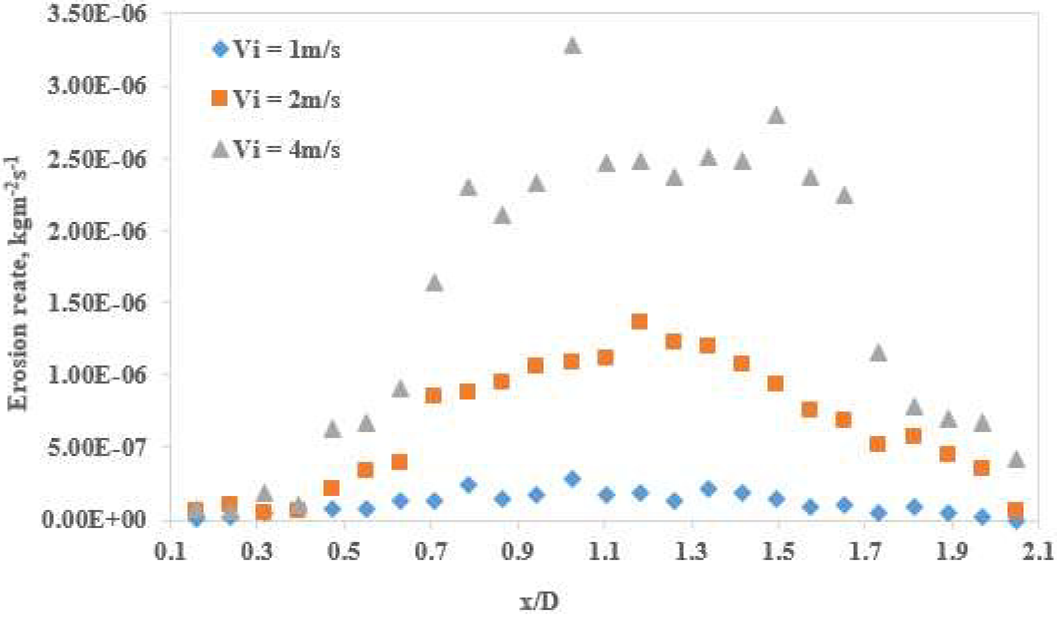

(b)

Figure 37 Effect of inlet flow velocity on the erosion rate pattern in the spacing between the two orifices for the case of Dr= 0.63, Dp= 100 µm; a) Double Orifice with 1D spacing, and b) Double Orifice with 2D spacing

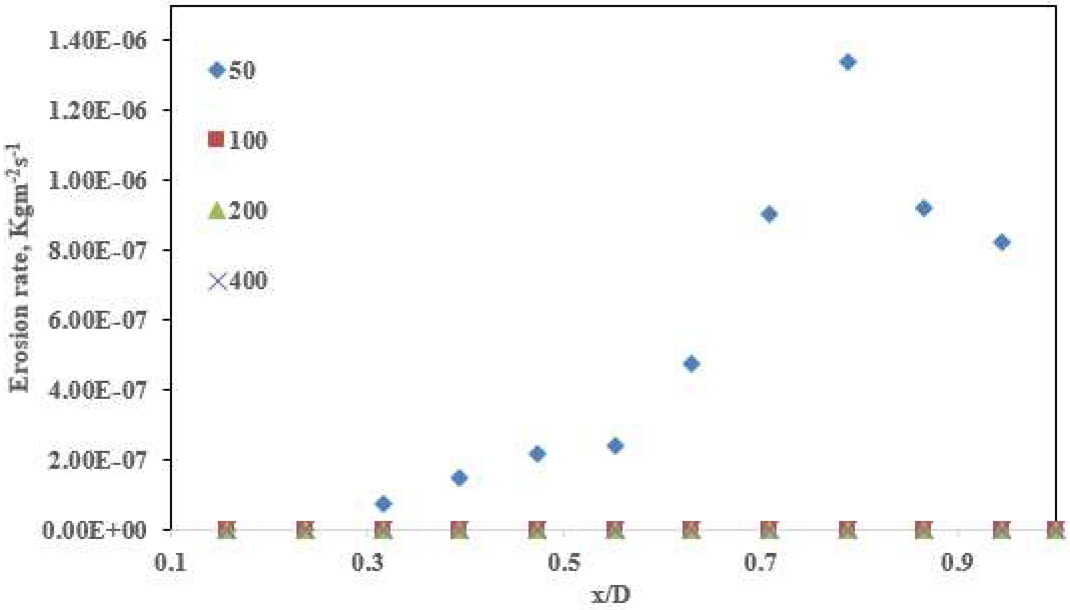

(a)

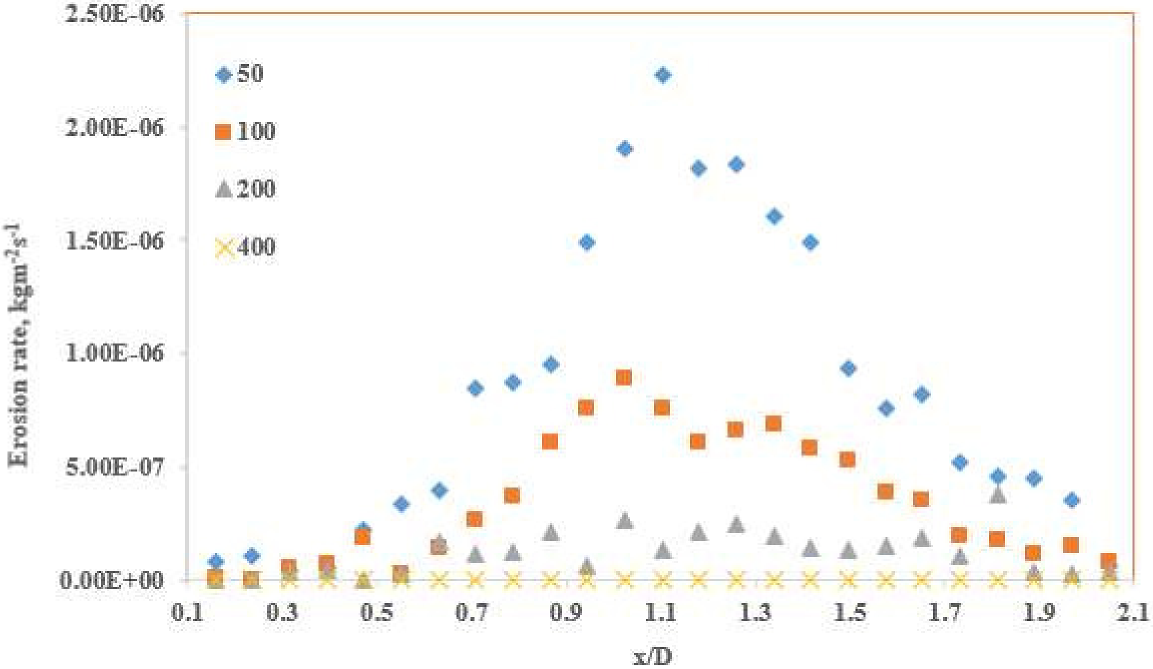

(b)

Figure 38 Effect of particle size on the erosion rate pattern in the spacing between the two orifices for the case of V_i= 2 m/s, D_r= 0.63; a) Double Orifice with 1D spacing, and b) Double Orifice with 2D spacing

CHAPTER 6

EXPERIMENTAL RESULTS

In this study, a Particle Image Velocimetery (PIV) system was used to investigate the flow field characteristics downstream of one or two bevel-edged orifice plates of diameter ratios, D_r= 0.5 and 0.63 and thickness of 3mm in a pipe with internal diameter of 25.4mm. The main objective is to investigate the flow field characteristics in order to enhance our understanding of the effect of different orifice arrangements on the flow regime. Such details are very important for studying other problems such as flow accelerated corrosion (FAC), solid particle erosion and many others. Experimental measurements using this PIV system were carried out for the velocity profiles for single-orifice and double-orifice configurations. The results obtained also served as a contribution for benchmarking the finite-volume computational model as well as the k-ε turbulence model.

The region of interest where the field characteristics were investigated are the downstream section of the orifice (of length 4D) as well as the spacing between the two orifices in the double-orifice arrangement considering 1D and 2D spacing. The orifices used in double-orifice configurations have exactly the same geometry. The part of the 4D downstream section covered by the optical width of laser light varies between 2D and 2.5D. This is due to limitation in the distance between the locations of laser and test section. Table 5 gives a summary of the parameters employed in the measurements and the velocity calculations are based on analysis sequence shown in Fig.3-15. An average of 4000 images was obtained at different frame rates depending on the Reynolds number.

Table 5 Summary of parameters used for the PIV measurement

Flow Properties	Reynolds number	2200−11200
Test piece	Pipe Internal diameter	25.4 mm
	Orifice size ($D_r = \frac{d}{D}$)	0.63, 0.5
	Test piece material	Acrylic
	Pipe external diameter	3.86 mm
	Continuous phase	Water
Seeding	Type	Polyamide
	Density	1.03
	Mean diameter	20
Light sheet	Type	Continuous wave (CW)
	Beam maximum output	4 W
	Wavelength	532 nm
	Beam diameter at aperture	3 nm
Camera	Type	Charge Coupled Device (CCD)
	Chip size/pixel size	1632 × 1200 pixels/11.5 μm
	Discretization	8 bit
	Lens focal length	60 mm
Capturing	f-number	2.8
	Viewing angle	Right angle
	Image magnification	0.217
	Measurement area pixel size	1152 × 480 pixels
	Real viewing area	61.70 × 25.70 mm^2
	Pulse separation	100−500 based on Re and D_r
	Maximum particle displacement	10 pixels
PIV Analysis	Interrogation area size, overlap ratio and number of iterations	32 × 32 pixels, 50% overlap, and 3 iterations

The PIV velocity vectors were obtained at approximately 340×50 points in axial and vertical directions of the downstream plane. Validation of results were carried out by comparing the numerical integration of elementary flow rates obtained from the velocity profiles at different axial distances with the measured value of volume flow rates at different Reynolds number as displayed in Table 6.

Table 6 Data employed and obtained from PIV measuring techniques

Calibration width = 53mm, Camera type = Speedsense 9040, Number of slides = 4000

Scale	Conversion to GPM	Measured Flow rate (m3/s)	Upstream Velocity (m/s)	Numerical flow rate (m3/s)	Uncertainty analysis (%)	Renolds no	frame rate (fps)	Exposure rate (μs)
11	0.6908	4.35781E-05	0.086003745	5.40E-05	2.38E+01	2184.49511	800	600
12	0.7536	4.75397E-05	0.093822267	5.89E-05	2.40E+01	2383.08558	900	550
15	0.942	5.94247E-05	0.117277834	7.36E-05	2.38E+01	2978.85697	1000	550
16	1.0048	6.33863E-05	0.125096356	7.90E-05	2.46E+01	3177.44744	1000	500
20	1.256	7.92329E-05	0.156370445	9.90E-05	2.50E+01	3971.8093	1300	430
22	1.3816	8.71562E-05	0.172007489	1.11E-04	2.74E+01	4368.99023	1500	420
27	1.6956	0.000106964	0.2111001	1.35E-04	2.59E+01	5361.94255	1800	370
30	1.884	0.000118849	0.234555667	1.50E-04	2.62E+01	5957.71395	2200	300
35	2.198	0.000138658	0.273648278	1.73E-04	2.50E+01	6950.66627	2200	250
40	2.512	0.000158466	0.31274089	1.99E-04	2.56E+01	7943.61859	2600	240
45	2.826	0.000178274	0.351833501	2.30E-04	2.90E+01	8936.57092	3000	200
51	3.2028	0.000202044	0.398744634	2.64E-04	3.08E+01	10128.1137	3400	160
60	3.768	0.000237699	0.469111334	3.29E-04	3.84E+01	11915.4279	3902	100

6.1 The Streamline Pattern

The streamline pattern for a representative flow rate at a Reynolds number of 8937 for a single orifice with diameter ratio D_r= 0.63 is shown in Fig.39. The figure shows a comparison between the streamlines obtained experimentally using the PIV technique (Figure 39a) and those obtained from the computational model using the finite-volume approximation utilizing FLUENT 12.1 (Figure 39b). The comparison shows a reasonably good agreement. Two important features of the flow field are clearly visible in the visualized streamline plot; the first is the primary recirculation zone on the downstream side of the orifice and the second is the location of the reattachment zone. Similar features were observed for other Reynolds numbers.

Shan et al. [10] reported a similar downstream streamline pattern but with an addition of secondary recirculation zone between the orifice and the primary recirculation zone in their experimental work using PIV system, however, their work was focused on a square-edged orifice which is slightly different from the orifice considered in this work. The additional features reported by Shan et al. [10] may be attributed partly due to the difference in orifice geometry and partly due to the fluorescent particles used as seeding particle which are capable of reflecting light at distinctive wavelength from that of the background and a more powerful laser light source (Nd-Yag) that produces light sheets with greater strength and intensity. Downstream streamline patterns with only primary recirculation and reattachment zones are widely reported in computation works like Shah et al. [8]. Figure 40 displays streamline pattern observed for single orifice flow with orifice diameter 0.5. The primary recirculation zone are bigger and longer in case of smaller D_r=0.5 as compared to D_r=0.63. Likewise, the reattachment point is situated farther downstream which makes the reattachment length longer for small diameter orifices.

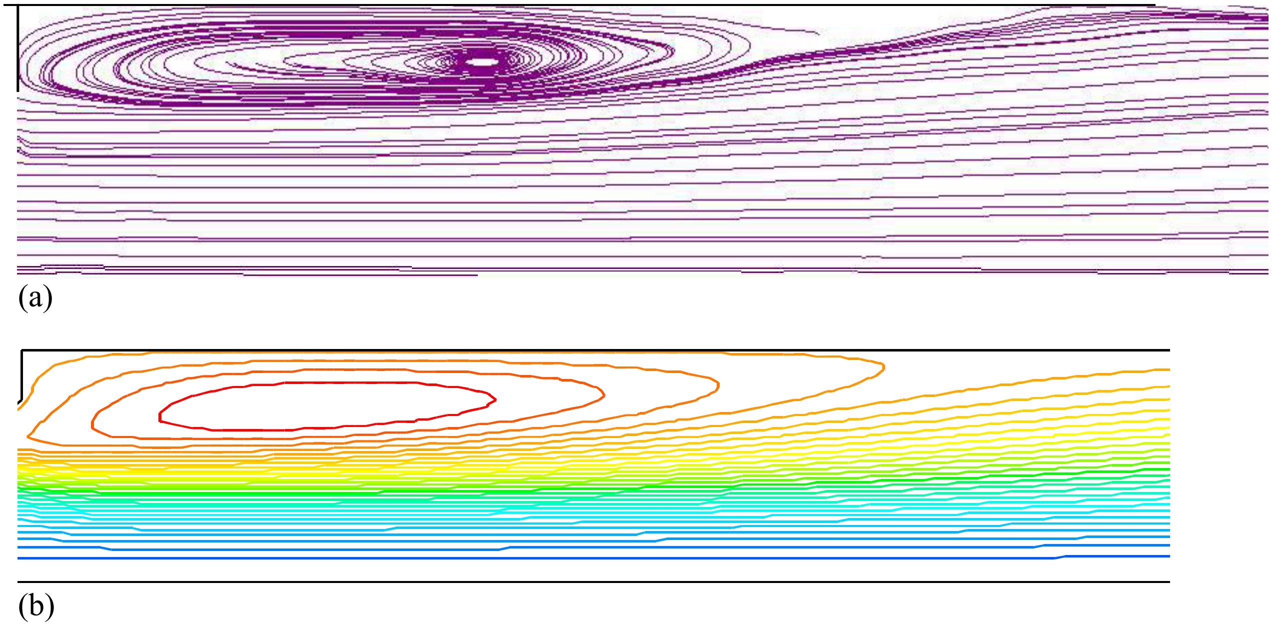

Figure 39 Streamline patterns downstream of a single orifice with D_r=0.63 at Re=8937; a) Experimental using PIV and b) Computational

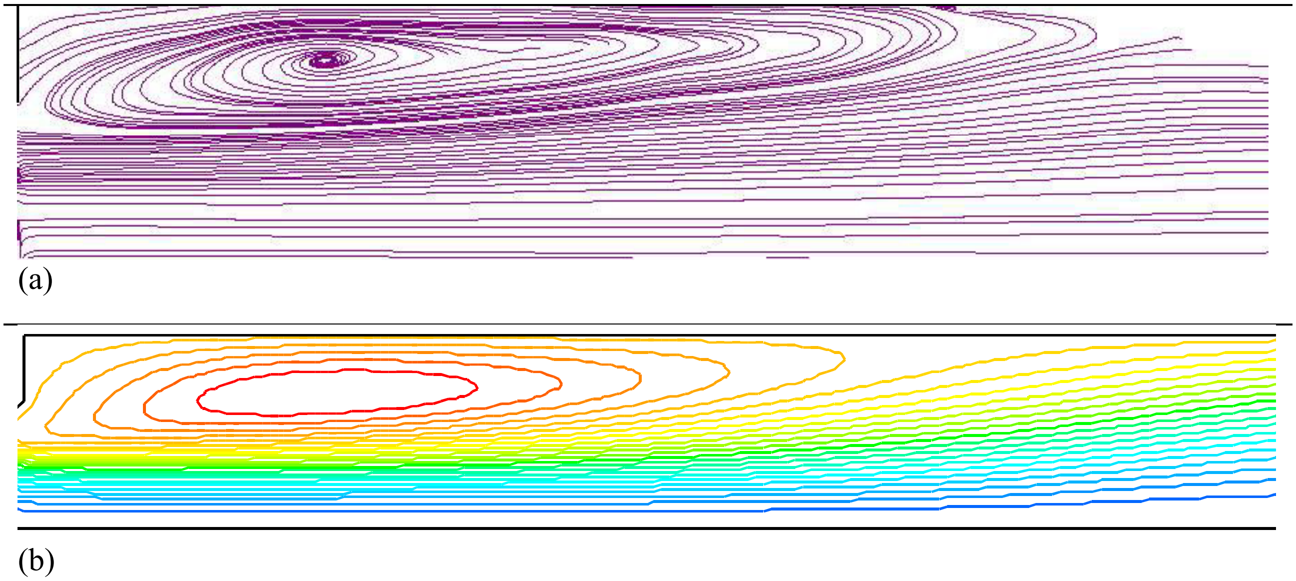

Figure 40 Streamline patterns downstream of a single orifice with D_r=0.5 at Re=4400; a) Experimental using PIV and b) Computational

The streamline patterns in the spacing between the two orifices in the double-orifice configuration with D_r=0.63 at flow Reynolds of 8937 are shown in Figure 41 for the case of 1D spacing and Figure 42 for the case of 2D spacing. It is clear from Figure 41 that the complete wall region in the orifice spacing is occupied by one recirculation (vortical) zone and the core has a jet-like flow. The center of the vortical motion is shifted closer to the second orifice. Also, the comparison between the visualized and computational patterns shows a reasonable agreement. On the other hand, the streamline pattern for the case of 2D spacing (Figure 42) has a different shape in comparison with that in the case of 1D spacing.

The primary recirculation zone has a different shape with its center shifted closer to the first orifice. The computational pattern has a small secondary recirculation zone located very close to the second orifice (Figure 42b) which does not appear in the PIV visualized pattern shown in Figure 42a. Moreover, the streamlines in the core region indicate a flow deceleration zone (diffuser-shaped streamtube) downstream of the vena contracta followed by flow acceleration zone in the neighborhood (upstream) of the second orifice (nozzle-shaped streamtube). Although the secondary recirculation zone is invisible in the PIV visualized streamlines, the general shapes of the two patterns (Figure 42a,b) are in reasonable agreement.

The streamline pattern downstream of the second orifice in the case of double-orifice arrangement for the same case of D_r=0.63 at Re=8937 is shown in Figure 43 for the case of 1D spacing and in Figure 44 for the case of 2D spacing. Figure 43 shows similar qualitative features of the recirculation and reattachment zones to that obtained in the case of a single orifice (see Figure 39) but with a smaller recirculation zone and a shorter distance between the orifice and the reattachment zone. Figure 44 shows the streamline pattern downstream of the second orifice for double-orifice arrangement with 2D spacing indicating a much longer recirculation zone in comparison with 1D spacing (Figure 43). It is important to mention that the longer recirculation zone downstream of a single orifice, or downstream of the second orifice in the double-orifice arrangement, indicates a longer shear layer extending from the orifice edge to the reattachment zone as reported by Shan et al. [10]. This layer contains vortex tripling structures causing peak vortex interactions and invariably peak turbulence intensity and Reynolds stress.

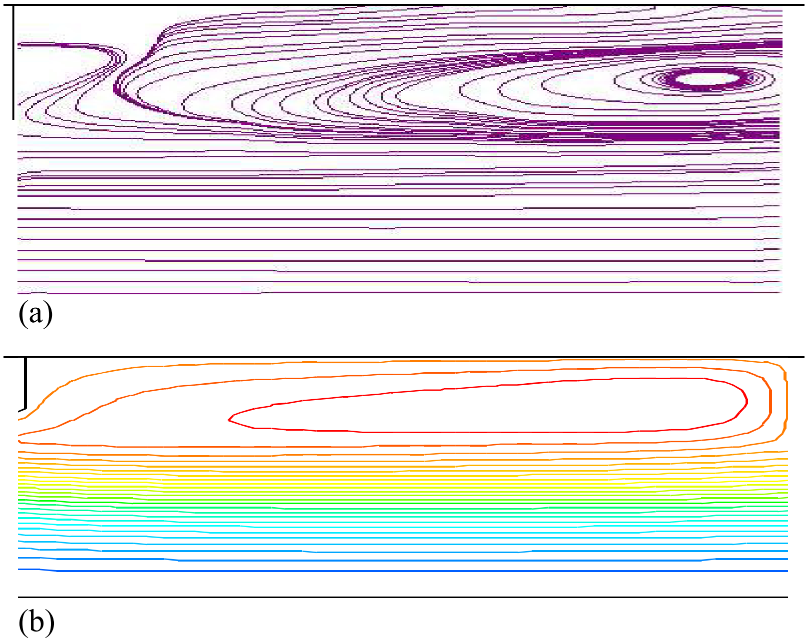

Figure 41 Comparison between the streamline patterns in the spacing between the two orifices in the double-orifice arrangement with 1D-spacing for the case of D_r=0.63 at Re=8937; a) Experimental using PIV and b) computational

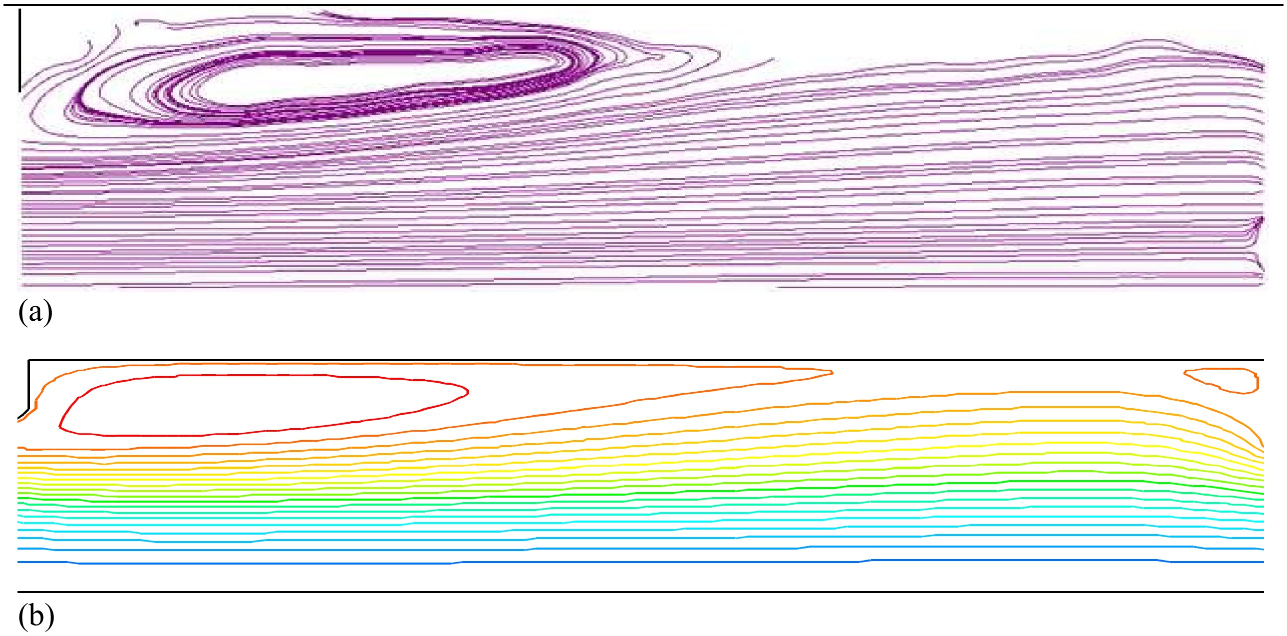

Figure 42 Comparison between the streamline patterns in the spacing between the two orifices in the double-orifice arrangement with 2D-spacing for the case of D_r=0.63 at Re=8937; a) Experimental using PIV and b) Computational

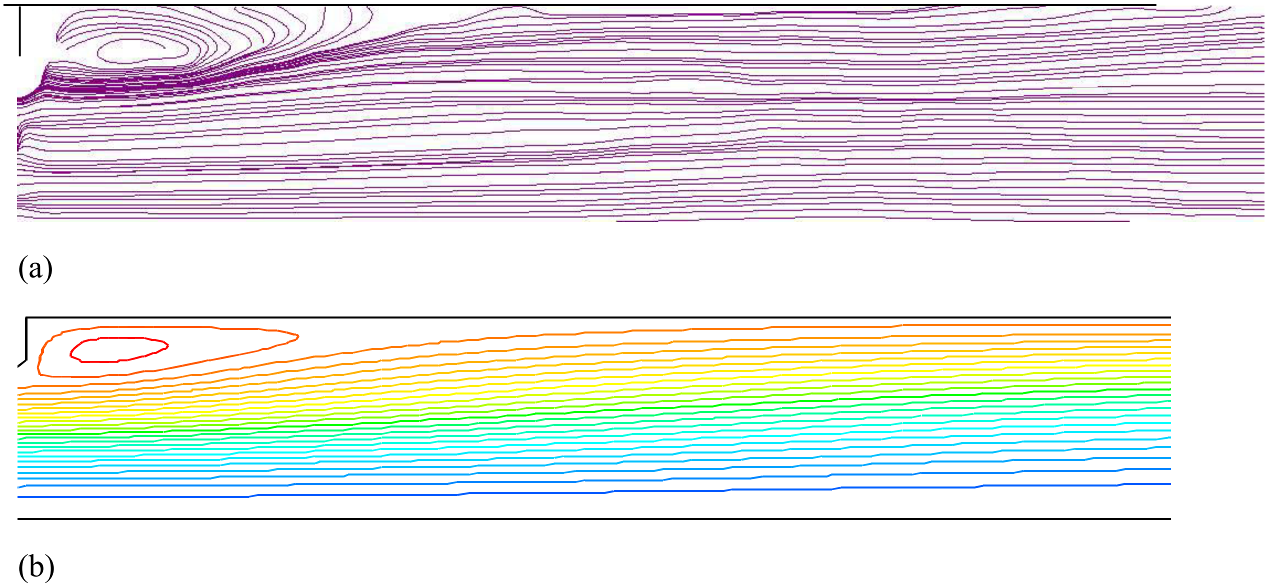

Figure 43 Comparison between the streamline patterns downstream of the second orifice in the double-orifice arrangement with 1D-spacing for the case of D_r=0.63 at Re=8937;a) Experimental using PIV and b) Computational

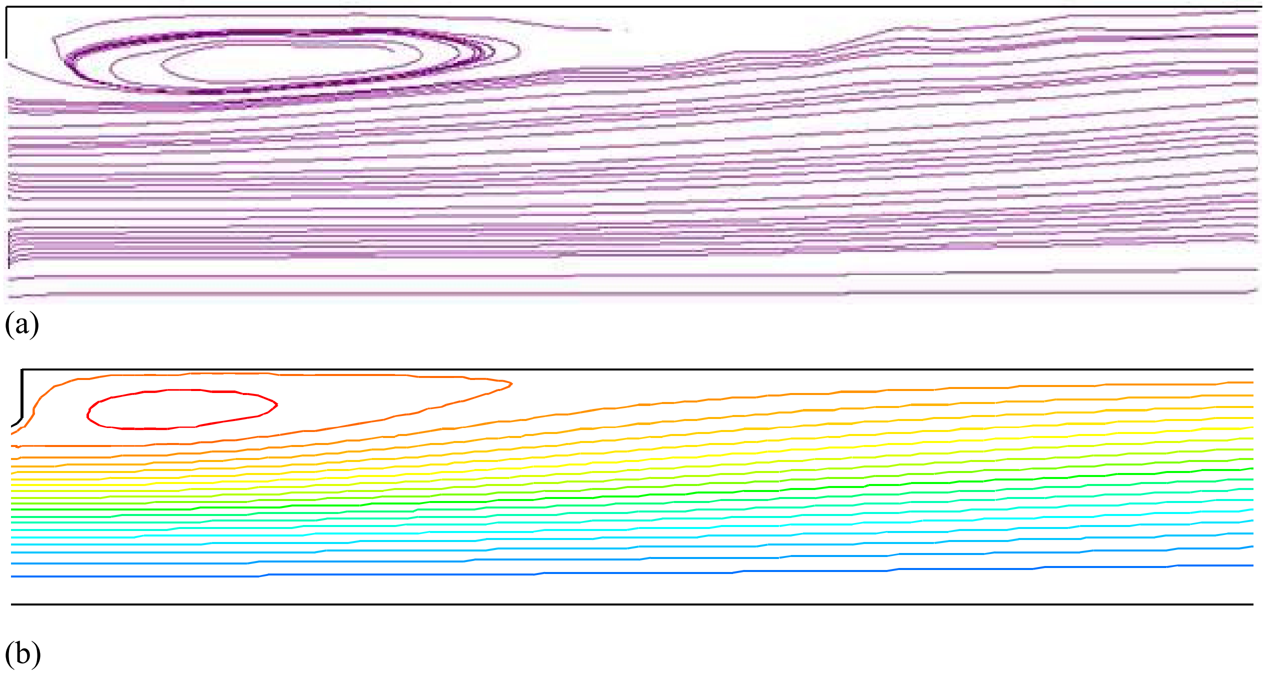

Figure 44 Comparison between the streamline patterns downstream of the second orifice in the double-orifice arrangement with 2D-spacing for the case of D_r=0.63 at Re=8937; a) Experimental using PIV and b) Computational

6.2 Velocity Profiles

The axial velocity profiles measured at three different sections downstream of the orifice plate (x=0.5D, 0.8D and 1.2D) for a single orifice with D_r=0.63 are displayed in Fig.45 with the ordinate and abscissa representing normalized mean axial velocity and normalized radial distance respectively. The velocity profile at the first axial location (x=0.5D) shows maximum velocity at the centerline with an almost uniform velocity distribution in the region $0 \le x \le 0.2D$ (the core region). This is followed by a rapid decrease of the velocity until reaching flow reversal near the wall. This flow reversal occurs in the primary recirculation zone in the wall region downstream of the orifice plate (see Figure 39). The maximum velocity gradient occurs at approximately r/D=0.27 which is within the shear layer.

The velocity profile at the second axial location (x=0.8D) indicates lower centerline axial velocity compared with that at x=0.5D and also smaller region of flow reversal. This indicates that the second axial location is downstream of the vena contracta. The axial velocity profile further downstream at x=1.2D shows a further decrease in reverse flow region, reduction in the velocity gradient at orifice height which implies lower shear stress in the shear layer, a smaller maximum velocity at the centerline which signifies deceleration in the flow in the streamwise direction and gradual disappearance of the flat portion of the profile close to the centerline. This shows that the flow is gradually assuming the pipe flow characteristics as it moves away from the orifice plate.

The axial velocity profiles for flow regime in single orifice with D_r=0.5 at the same axial location are shown in Fig.46. Although the profiles are qualitatively similar to those presented in Figure 45, the core region characterized by uniform velocity distribution at x=0.5D is much smaller ($0 \le x \le 0.12D$ instead of $0 \le x \le 0.2D$) and the maximum velocity gradient (in the shear layer) is much higher. In addition, the region of flow reversal near the wall is larger reflecting a larger recirculation zone and the maximum velocity at the centerline is much higher.

Figure 47a presents the relationship between the measured axial velocity at the vena contracta and the mean inlet velocity for the case of a single orifice with D_r=0.63. A line fitting of these data points gives a linear relationship in the form $U_{\max} = 3.548 V_i - 0.052$ for the Reynolds number range $2200 \le Re \le 11200$. Shan et al. [10] established a similar relationship in the form $U_{\max} = 4.1 V_i - 0.13$ for an orifice of diameter ratio D_r=0.62 in the Reynolds number range $2.5\times10^4 \le Re \le 5.5\times10^4$.

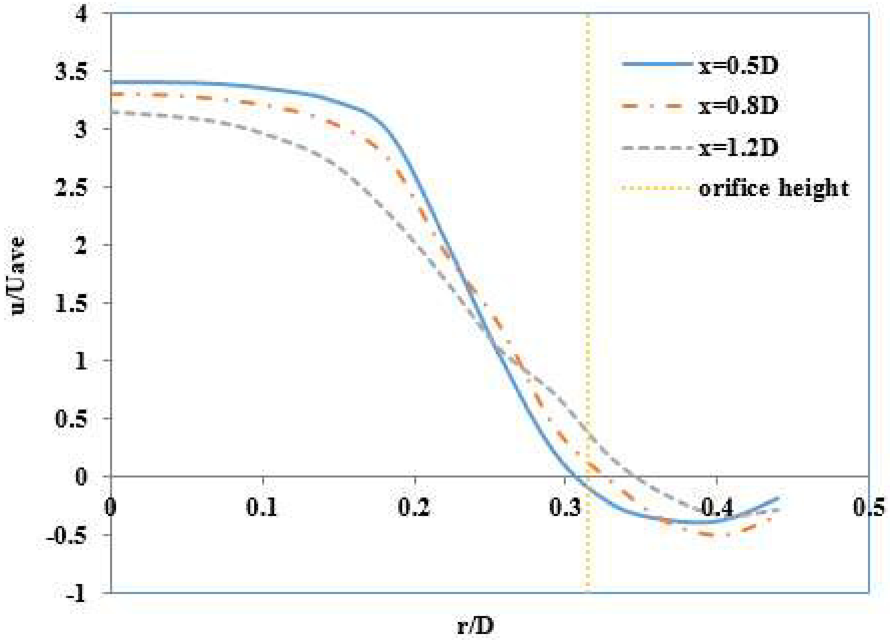

Figure 45 Radial profiles of mean axial velocity at axial locations x/D=0.5, 0.8 and 1.2 downstream of a single orifice for the case of Dr=0.63 and Re=8937

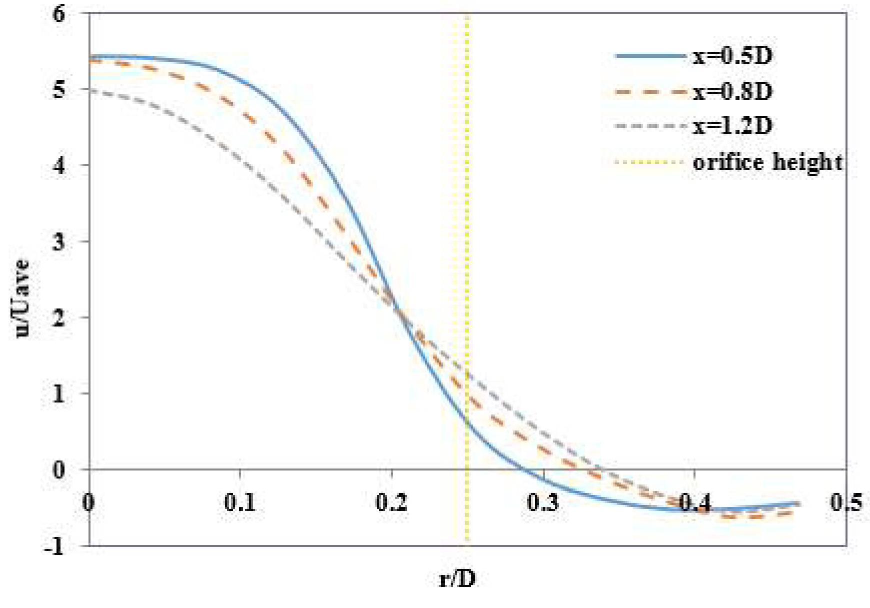

Figure 46 Radial profiles of mean axial velocity at axial locations x/D=0.5, 0.8 and 1.2 downstream of a single orifice for the case of Dr=0.5 and Re=4400

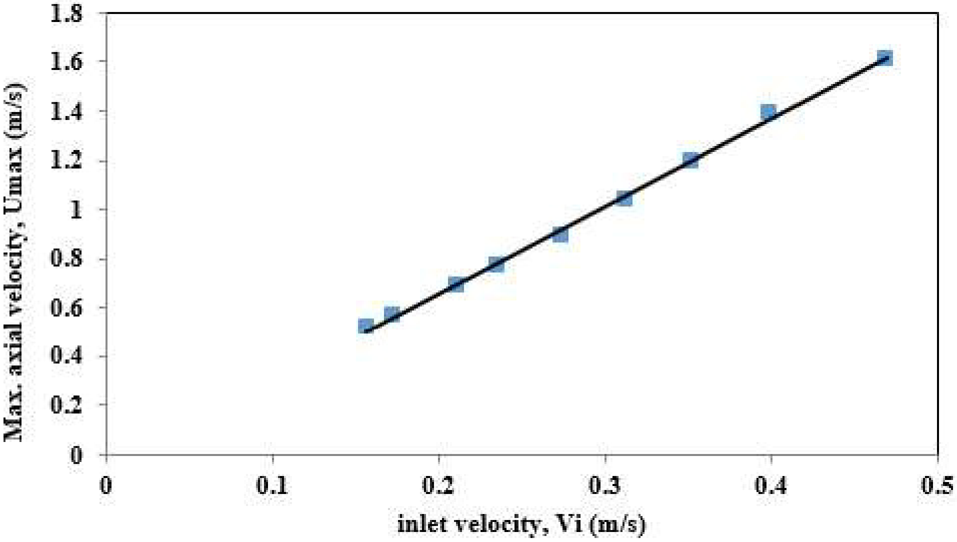

(a)

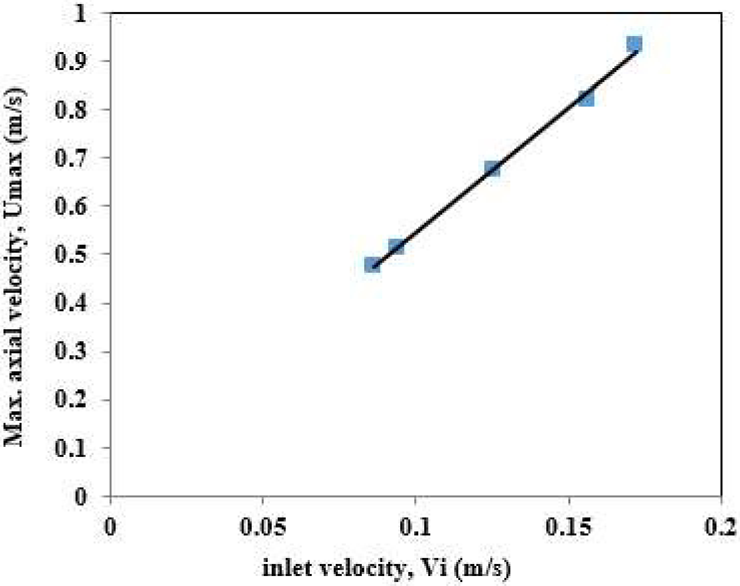

(b)

Figure 47 Variation of maximum axial velocity with inlet velocity for a single orifice, a) D_r=0.63, b) D_r=0.5

Similar data were obtained for D_r=0.5 (as shown in Fig.47b) and fitted to the equation $U_{\max} = 5.192V_i - 0.026$ for the Reynolds number range $2200 \le Re \le 4500$. Further experimental studies involving other orifice sizes and wider range of Reynolds number are required to serve as verification for these relationships that provide basis for a more general correlation that includes orifice diameter ratio and a wider range of Reynolds number.

The velocity profiles measured using PIV at different axial locations (x=0.3, 0.5, and 0.8) in the spacing between the two orifices for the case of double-orifice configuration with 1D spacing and D_r=0.63 are shown in Fig. 48. It is clear from the figure that the centerline velocity is almost constant at the three locations indicating insignificant deceleration in the streamwise direction. Also, the velocity distribution is almost uniform in the core region ($0 \le r \le 0.18D$) characterizing the jet-like flow. On the other hand, the flow reversal near the wall is characterized by higher velocity as x increases while the radial location of the point of vanishing axial velocity is unchanged (approximately at $r = 0.37D$). The measured axial velocity profiles at the same stations (x=0.3, 0.5, and 0.8) in the orifice spacing of double-orifice arrangement with 2D spacing for the case of D_r=0.63 and Re=8937 are shown in Figure 49.

A comparison between the velocity distributions in the core region ($r \le 0.2\,D$) in Figures 48 and 49 indicates insignificant changes in the velocity profiles at the three axial locations. However, the velocity distributions near the wall in the case of 2D spacing are different from those of 1D spacing resulting from the changes in the shape and size of the primary recirculation zone. Also, the reverse flow velocity near the wall ($0.37D \le r \le 0.5\,D$) in the case of 2D spacing is much less than that in the case of 1D spacing as can be seen in Figures 48 and 49. Based on the understanding of the flow structure downstream of a single orifice presented by Shan et al. [10], it is believed that the 2D spacing allows the nearly natural formation of the circulatory vortical flow behind the first orifice and thus creating longer shear layers hence giving room for flow deceleration before reaching the second orifice.

This explanation is manifested by a simple comparison between the velocity profiles in the farthest downstream location, at x=0.8D, for the two case of 1D spacing (Figure 48) and 2D spacing (Figure 49). The two velocity profiles indicate lower velocities near the centerline and higher velocities in the intermediate region (between the core and wall regions).

Figure 50 shows a comparison between the axial velocity profiles in the downstream section of a single orifice and those downstream the second orifice in both cases of double-orifice configurations with 1D and 2D spacing at axial locations x/D = 0.5, 0.8 and 1.2. It should be mentioned that in this figure x is measured from the orifice plate in the single orifice configuration and is measured from the second orifice in the double-orifice configuration. It can be seen that the magnitude of the maximum axial velocity (centerline velocity) decreases as the flow progresses further downstream for all configurations. The double-orifice configuration with 1D spacing has the least centerline axial velocity while that with 2D spacing produces the highest maximum axial velocity. The reason for this is that the second orifice placed at 1D spacing produces negligible streamline contraction effect on flow passing through its opening (either on the upstream or downstream sides of the orifice plate) when compared to the case of 2D spacing.

Moreover, the double-orifice with 1D spacing results in the least decrease in the centerline axial velocity in the region $0.5D \le x \le 1.2D$.In conclusion, the spacing between the two orifices determines the extent of flow deceleration that takes place downstream of the vena contracta of the first orifice. It also affects the length of the shear layer extending from the second orifice to the reattachment zone; thus affecting the hydraulic losses.

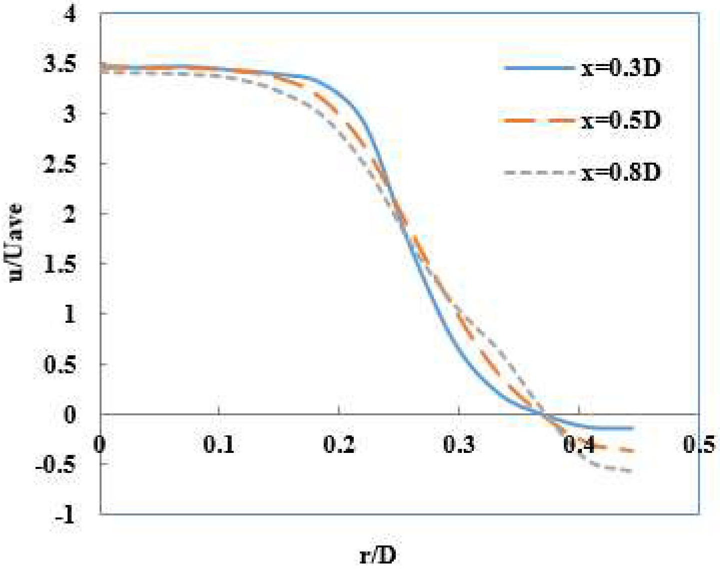

Figure 48 Radial profiles of mean axial velocity at axial locations x/D=0.3, 0.5 and 0.8 in the orifice spacing of double-orifice arrangement with 1D spacing for the case of D_r=0.63 and Re=8937

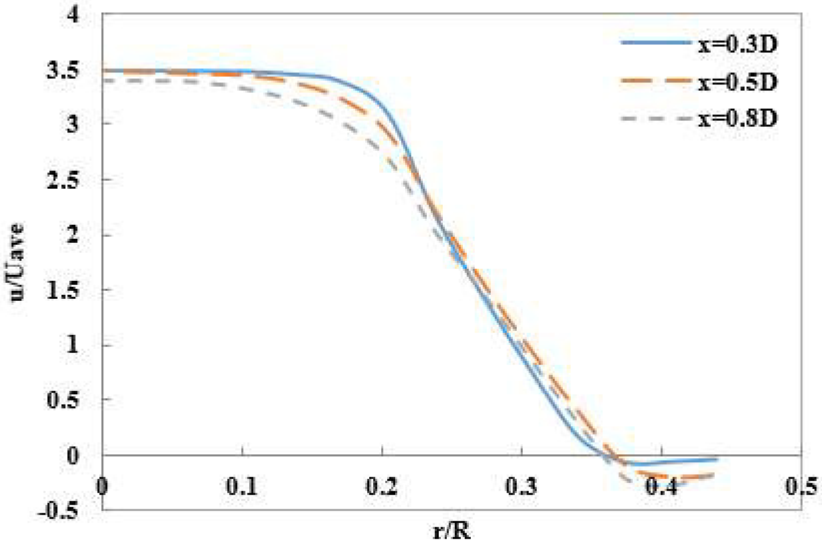

Figure 49 Radial profiles of mean axial velocity at axial locations x/D=0.3, 0.5 and 0.8 in the orifice spacing of double-orifice arrangement with 2D spacing for the case of D_r=0.63 and Re=8937

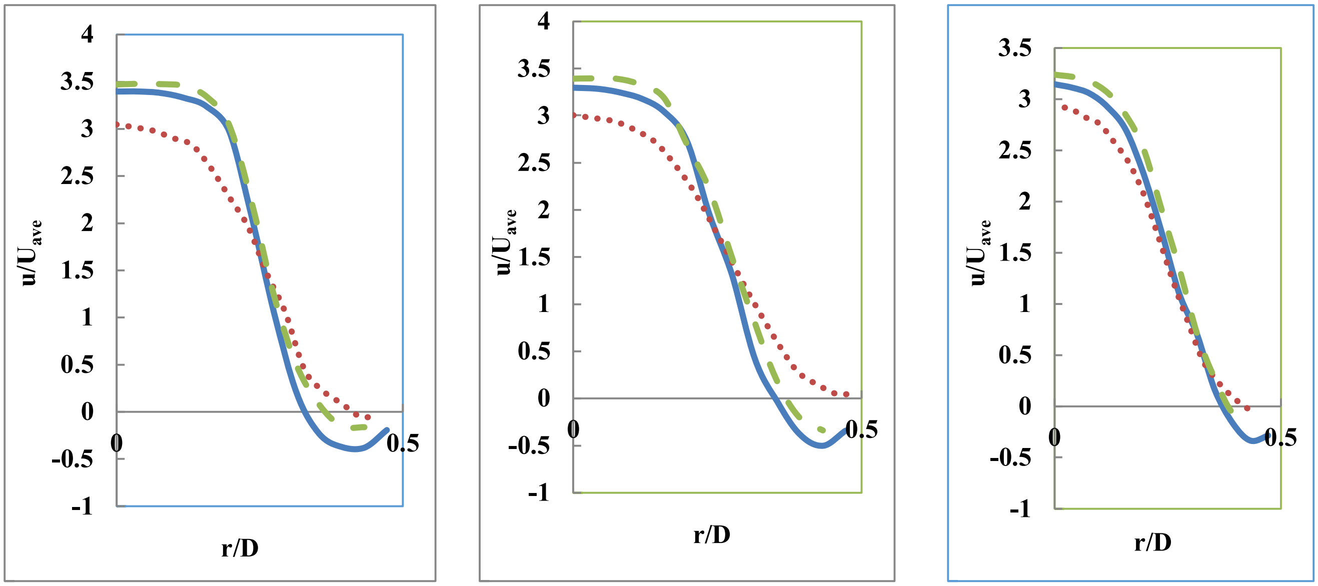

x=0.5D **x=0.8D** **x=1.2D**

Figure 50 Comparison between mean axial velocity profiles for the three configurations at axial locations x/D=0.5, 0.8 and 1.2; ---------single-orifice, ... double-orifice-1Dspace,- - - -double-orifice-2Dspace

6.3 Comparison with Computational Velocity Profiles

This section presents a comparison between velocity profiles obtained by 2D/2C PIV system and computational results obtained through k-ε eddy viscosity model (EVM) applied to a similar flow domain. Figure 6-13 shows such comparison in the plots of normalized axial velocity against normalized radial distance at different downstream locations for single orifice configuration with D_r=0.63.The axial velocity and radial distance are normalized with mean flow velocity and pipe diameter respectively. It can be observed that the shape of the two profiles is the same but with a constant difference. The volumetric flow rate calculated using numerical integration based on the measured axial velocity profile was found to differ from the actual flow rate (measured by the flowmeter) by approximately 23.5%. On the other hand, the volumetric flow rate obtained by numerical integration of the axial velocity profile obtained from the computational model was found to differ by only 0.74% from the measured flow rate.

The difference between in the computational and experimental velocity profiles is attributed to the error introduced by optical distortion due to the surface curvature of the pipe. The pipe is made by drilling a cylindrical hole in a prism of rectangular cross section that makes the pipe outer surfaces to be flat. This helped in reducing the error to an extent but a better approach is to insert the pipe through a rectangular basin filled with same fluid as implemented by many previous studies like Shan et al. [10] and Lindken & Merzkirch [67].

Moreover, the absence of a timer box which should serve as synchronization unit to generate trigger pulses for the camera and laser light source contributed to part of the error. Also, the use of a more advanced PIV technique like stereo-PIV and using fluorescent particles as seeding particles can improve the accuracy of the PIV measurements especially in regions close to the pipe wall. Shan et al. [10] also suggested that the discrepancy can also be due to the poor estimation of vortex structures introduced by the orifice in the shear layer region by the Reynolds Averaged Navier-Stokes (RANS) model adopted in the computational analysis. In addition, the PRESTO k-ε model can give an approximate valid representation of flow through an orifice. The submission of previous studies on orifice flows by Shah et al. [8] also gives credence to the accuracy of the k-ε model.

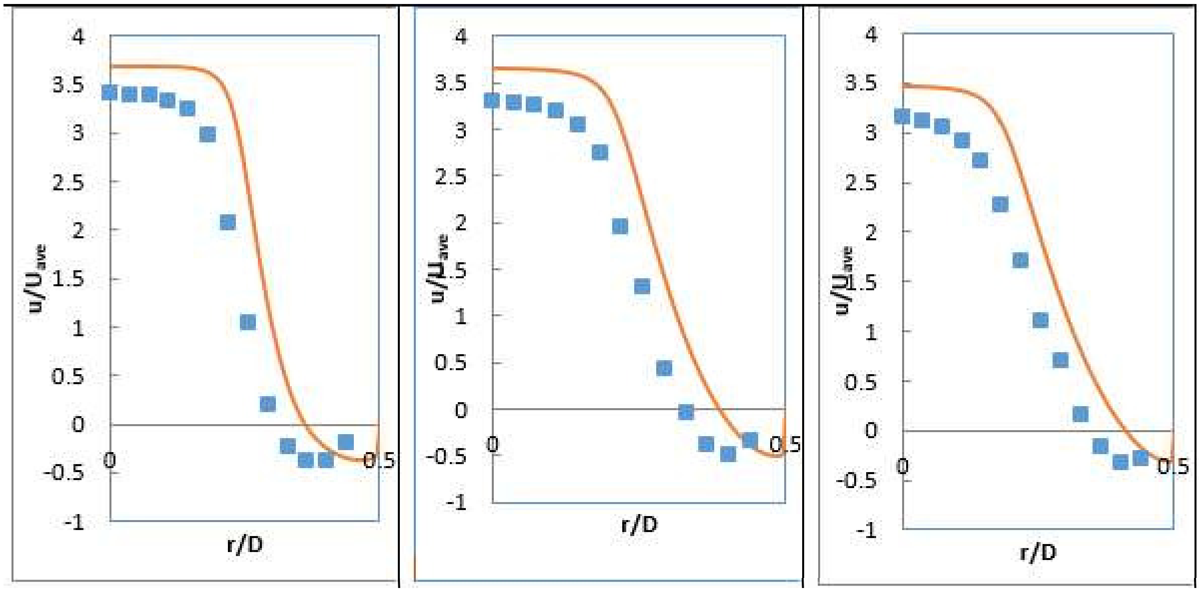

x=0.5D x=0.8D x=1.2D

Figure 51 Comparison between experimental and numerical axial velocity profiles at locations x/D=0.5, 0.8 and 1.2 for the case of a single orifice with D_r=0.63 and Re=8937 (□ Experimental, ____Numerical)

CHAPTER 7

CONCLUSION

The flow structure and erosion characteristics in multiple orifice system have been investigated by considering the effects of flow inlet velocity, orifice geometry, orifice spacing and solid particle size on the resulting flow and erosion patterns. The inlet flow velocities considered are 1m/s, 2m/s, and 4m/s, orifice spacing of one and two pipe diameters, orifice diameter ratios of 0.5, 0.63 and 0.77, and particle size ranging from 50 to 400µm. Numerical simulations for single and multiple orifices configurations were carried out using the PRESTO, realizable k-ε turbulence model to solve the governing equations.

The flow characteristics downstream the multiple orifice arrangement is similar qualitatively to that downstream single orifice in terms of the existence of recirculation zone, reattachment zone and shear layer region. Certain differences such as the nature of flow upstream the second orifice in double orifice configurations which has a jet-like flow in the core region surrounded by donut-shaped vortical flow in the wall region influencing the downstream velocity field and pressure recovery region. The double orifice arrangement spacing produces a peak velocity that is slightly higher than single orifice with corresponding orifice size but at a similar location. The double orifice with two pipe diameter spacing produces a second peak velocity downstream the second orifice. The pressure distribution across the three configurations are similar but the least and highest pressure drop were recorded in the double orifice configurations with one and two pipe diameter spacing respectively.

The effect of solid particle size in addition to above parameters on the erosion pattern was investigated for carbon steel pipe of one inch diameter. The Lagrangian particle-tracking model was incorporated with the stated turbulence flow model to predict the particle trajectories. A 2% by weight sand particle loading was maintained for all the cases considered. In all considered configurations, the critical regions observed to be most prone to erosion are the recirculation and reattachment zones. The erosion rate recorded in the orifice spacing in double orifice configurations is negligibly small for large particle sizes $\left(D_p \geq 100\ \mu m\right)$.

Also, the double orifice configuration with one pipe diameter spacing experienced the least erosion rate. In general, the erosion rate increases with increasing inlet flow velocity, decreasing particle sizes and decreasing diameter ratios for the three configurations considered. Flow visualization and measurement were also carried for the three orifice configurations for the case of $D_r=0.63$ in the Reynolds number range 4400-11200 using the PIV measuring system. There is a fair agreement between the axial velocity profiles in the region $0.5 \leq \frac{x}{D} \leq 1.2$ and pressure distributions downstream the first orifice obtained experimentally and numerically.

CHAPTER 8

RECOMMENDATIONS

The present study showed that there are many aspects of orifice flow, especially for multiple-orifice configuration that requires detailed investigation. For example, the effect of orifice spacing on the flow structures downstream of the second orifice focusing on the characteristics of the shear layer that extends from the orifice plate until reaching the reattachment zone requires comprehensive investigation. The effect of orifice spacing on the erosion pattern and total erosion rate downstream of the second orifice is also important and requires further investigation. The case of higher percentage of solid particle content which results in two-way coupling between the continuous and discrete phases requires a thorough computational as well as experimental studies. Another interesting area of research is the case of two-phase (liquid and gas) flow through single or multiple orifice arrangements. The presence of cavitation at the vena contracta and its effect on the flow structure and resulting pressure drop in single and double-orifice arrangements is another challenging problem that is worth consideration.

Nomenclature

$\bar{a}$	flow acceleration
A	area of interrogation area
A_c	flow area at vena contracta
A_i	material impingement area
C_d	coefficient of discharge
d	orifice diameter
$\bar{d}$	image plane
$\bar{D}$	object plane
D	pipe diameter
D_{diff}	diffraction limiting diameter
D_p	particle diameter
D_r	diameter ratio
E_{lc}	local erosion rate
f	focal length
$f_\#$	f-number of camera
F_s	particle shape coefficient
F_θ	impact angle function
F_{pg}	buoyancy force
F_{sl}	Saffman lift force
F_{vm}	virtual mass force

g	acceleration due to gravity
I	image intensity of first exposure
I'	image intensity of second exposure
k	turbulence kinetic energy
M	magnification
n	empirical coefficient
N	number of multiplication per correlation
P	static pressure
P_n	rate of local penetration
Q	empirical constant for local erosion rate
R_c	correlation of particle image
R_D	convolution of matching pairs' mean velocity
R_F	fluctuating noise component of cross correlation
Re	Reynolds number based on inlet velocity
Re_p	particle's Reynolds number
R_{II}	cross correlation
$\bar{r}$	position vector
$\dot{s}$	solid particle rate
$\bar{s}$	image separation vector
t	time
Δt	time interval between two successive exposure

Δt_8	particle duration to travel 8 pixels
$\overline{u_\iota}$	fluctuating velocity component
$\overline{U_\iota}$	component of average velocity
U_{max}	flow maximum velocity
$\overline{U_\iota}$	lag velocity
u_p	particle velocity
V	particle impingement speed
V_i	inlet flow velocity
w	interrogation area width
$\bar{x}$	particle coordinate (image domain)
$\bar{X}$	particle coordinate (real domain)
Δx	peak displacement
x_i	space coordinate

Greek symbols

ε	dissipation rate
α	angle of impact
β	area ratio
β_c	contraction coefficient
γ	cutting wear coefficient

δ_{ij}	kronecker delta
δ_m	minimum light sheet thickness
ρ	density
ρ_m	density of target material
σ	deformation wear coefficient
σ_k	effective prandtl number for kinetic energy
σ_k	effective prandtl number for dissipation
μ	dynamic viscosity
μ_t	turbulence viscosity
μ_{eff}	effective viscosity
λ	wavelength of light
Θ	correlation function

Abbreviations

2D2C PIV	two dimensional two components PIV
ANSI	American National Standard Institute
BSP	British Standard Pipe
CCD	Charged Couple Device
CFD	Computational Fluid Dynamics

CW	Continuous Wave
DPM	Discrete Phase Model
FAC	Flow Accelerated Corrosion
FOV	Field of View
HWA	Hot Wire Anemometry
IA	Interrogation Area
IBM	Immersed Boundary Method
ISO	International Organization for Standardization
LDA	Laser Doppler Anemometry
LDIE	Liquid Droplet Impingement Erosion
LED	Light Emitting Diode
MTC	Mass Transfer Coefficient
PCC	Phantom Camera Control
PRESTO	Pressure Staggering Option
PIV	Particle Image Velocimetry
RSM	Reynolds Stress Model
SNR	Signal-to-noise-ratio

References

[1] K. Doblhoff-Dier, K. Kudlaty, M. Wiesinger, and M. Gröschl, “Time resolved measurement of pulsating flow using orifices,” *Flow Meas. Instrum.*, vol. 22, no. 2, pp. 97–103, Apr. 2011.

[2] F. Peters and T. F. Groß, “Flow rate measurement by an orifice in a slowly reciprocating gas flow,” *Flow Meas. Instrum.*, vol. 22, no. 1, pp. 81–85, Mar. 2011.

[3] T. Gronych, M. Jeřáb, L. Peksa, J. Wild, F. Staněk, and M. Vičar, “Experimental study of gas flow through a multi-opening orifice,” *Vacuum*, vol. 86, no. 11, pp. 1759–1763, May 2012.

[4] V. K. Singh and T. John Tharakan, “Numerical simulations for multi-hole orifice flow meter,” *Flow Meas. Instrum.*, vol. 45, pp. 375–383, Oct. 2015.

[5] C. Alimonti, G. Falcone, and O. Bello, “Two-phase flow characteristics in multiple orifice valves,” *Exp. Therm. Fluid Sci.*, vol. 34, no. 8, pp. 1324–1333, Nov. 2010.

[6] W. Haimin, X. Shujuan, S. Qingyi, Z. Caimin, L. Hao, and C. Eryun, “Experiment study on pressure drop of a multistage letdown orifice tube,” *Nucl. Eng. Des.*, vol. 265, pp. 633–638, Dec. 2013.

[7] D. Chisolm, “Two-Phase Flow in Heat Exchangers and Pipelines,” *Heat Transf. Eng.*, vol. 6, no. 2, pp. 48–57, Jul. 2007.

[8] M. S. Shah, J. B. Joshi, A. S. Kalsi, C. S. R. Prasad, and D. S. Shukla, “Analysis of flow through an orifice meter: CFD simulation,” *Chem. Eng. Sci.*, vol. 71, pp.

300–309, 2012.

[9] R. E. DeOtte, Jr, G. L. Morrison, D. L. Panak, and G. H. Nail, "3-D laser doppler anemometry measurements af the axisymmetric flow field near an orifice.pdf," *Flow Meas. Instrum.*, vol. 2, pp. 115–123, 1991.

[10] F. Shan, A. Fujishiro, T. Tsuneyoshi, and Y. Tsuji, "Particle image velocimetry measurements of flow field behind a circular square-edged orifice in a round pipe," *Exp. Fluids*, vol. 54, no. 6, p. 1553, Jun. 2013.

[11] J. Westerweel, A. A. Draad, J. G. T. van der Hoeven, and J. van Oord, "Measurement of fully-developed turbulent pipe flow with digital particle image velocimetry," *Exp. Fluids*, vol. 20, no. 3, pp. 165–177, Jan. 1996.

[12] E. J. Stamhuis, "Basics and principles of particle image velocimetry (PIV) for mapping biogenic and biologically relevant flows," *Aquat. Ecol.*, vol. 40, no. 4, pp. 463–479, 2006.

[13] M. Raffel, C. E. Willert, S. T. Wereley, and J. Kompenhans, "Particle Image Velocimetry," *Curr. Sci.*, vol. 79, no. 1, pp. 51–60, 2007.

[14] H. P. Rani, T. Divya, R. R. Sahaya, V. Kain, and D. K. Barua, "Numerical investigation of energy and Reynolds stress distribution for a turbulent flow in an orifice," *Eng. Fail. Anal.*, vol. 34, pp. 451–463, Dec. 2013.

[15] M. A. Nemitallah, R. Ben-Mansour, M. a. Habib, W. H. Ahmed, I. H. Toor, Z. M. Gasem, and H. M. Badr, "Solid Particle Erosion Downstream of an Orifice," *J. Fluids Eng.*, vol. 137, no. 2, p. 021302, 2014.

[16] K. M. Hwang, C. K. Lee, and C. R. Choi, “A Study on the Cause Analysis for the Wall Thinning and Leakage in Small Bore Piping Downstream of Orifice,” *World J. Nucl. Sci. Technol.*, vol. 04, no. 01, pp. 1–6, Dec. 2014.

[17] W. H. Ahmed, M. M. Bello, M. El Nakla, and A. Al Sarkhi, “Flow and mass transfer downstream of an orifice under flow accelerated corrosion conditions,” *Nucl. Eng. Des.*, vol. 252, pp. 52–67, 2012.

[18] J. Xiong, X. Cheng, and Y. Yang, “Numerical investigation on mass transfer enhancement downstream of an orifice,” *Int. J. Heat Mass Transf.*, vol. 68, pp. 366–374, Jan. 2014.

[19] M. K. Bull and N. G. Agarwal, “Characteristics of flow separation due to an orifice plate in fully-developed turbulent flow-pipe.” 1983.

[20] X. Yaer, K. Shimizu, H. Matsumoto, T. Kitsudo, and T. Momono, “Erosive wear characteristics of spheroidal carbides cast iron,” *Wear*, vol. 264, no. 11–12, pp. 947–957, May 2008.

[21] D. Aquaro and E. Fontani, “Erosion of Ductile and Brittle Materials,” *Meccanica*, vol. 36, no. 6, pp. 651–661.

[22] K. Shimizu, Y. Xinba, and S. Araya, “Solid particle erosion and mechanical properties of stainless steels at elevated temperature,” *Wear*, vol. 271, no. 9–10, pp. 1357–1364, Jul. 2011.

[23] M. Rochester and J. Brunton, *Erosion, Wear, and Interfaces with Corrosion*. 100 Barr Harbor Drive, PO Box C700, West Conshohocken, PA 19428-2959: ASTM

International, 1974.

[24] R. J. K. Wood, T. F. Jones, J. Ganeshalingam, and N. J. Miles, "Comparison of predicted and experimental erosion estimates in slurry ducts," *Wear*, vol. 256, no. 9–10, pp. 937–947, May 2004.

[25] J. G. A. Bitter, "A study of erosion phenomenon part I," *Wear*, vol. 6, pp. 5–21, 1963.

[26] J. G. A. Bitter, "A Study of Erosion Phenomenon Part II," *wear*, vol. 6, pp. 169–190, 1963.

[27] S. A. Shirazi, J. R. Shadley, B. S. McLaury, and E. F. Rybicki, "A Procedure to Predict Solid Particle Erosion in Elbows and Tees," *J. Press. Vessel Technol.*, vol. 117, no. 1, p. 45, Feb. 1995.

[28] D. O. Njobuenwu and M. Fairweather, "Modelling of pipe bend erosion by dilute particle suspensions," *Comput. Chem. Eng.*, vol. 42, pp. 235–247, Jul. 2012.

[29] M. A. Habib, H. M. Badr, R. Ben-Mansour, and M. E. Kabir, "Erosion rate correlations of a pipe protruded in an abrupt pipe contraction," *Int. J. Impact Eng.*, vol. 34, no. 8, pp. 1350–1369, Aug. 2007.

[30] H. M. Badr, M. A. Habib, R. Ben-Mansour, and S. A. M. Said, "Numerical investigation of erosion threshold velocity in a pipe with sudden contraction," *Comput. Fluids*, vol. 34, no. 6, pp. 721–742, Jul. 2005.

[31] H. M. Badr, M. A. Habib, R. Ben-Mansour, S. A. M. Said, and S. S. Al-Anizi, "Erosion in the tube entrance region of an air-cooled heat exchanger," *Int. J.*

Impact Eng., vol. 32, no. 9, pp. 1440–1463, Sep. 2006.

[32] M. K. Roul and S. K. Dash, “Single-Phase and Two-Phase Flow Through Thin and Thick Orifices in Horizontal Pipes,” *J. Fluids Eng.*, vol. 134, no. 9, p. 91301, 2012.

[33] C. L. Hollingshead, M. C. Johnson, S. L. Barfuss, and R. E. Spall, “Discharge coefficient performance of Venturi, standard concentric orifice plate, V-cone and wedge flow meters at low Reynolds numbers,” *J. Pet. Sci. Eng.*, vol. 78, no. 3–4, pp. 559–566, 2011.

[34] S. Eiamsa-ard, A. Ridluan, P. Somravysin, P. Promvonge, and N. Chok, “Numerical investigation of turbulent flow through a circular orifice,” *KMITL Sci.J.*, vol. 8, no. 1, pp. pp. 44–50, 2008.

[35] S. Dabiri, W. a. Sirignano, and D. D. Joseph, “Cavitation in an orifice flow,” *Phys. Fluids*, vol. 19, no. 7, p. 072112, 2007.

[36] S. V Patankar, *Numerical heat transfer and fluid flow*. New York: Hemisphere Publishing Corporation, 1980.

[37] F. Nygard and H. I. Andersson, “Numerical simmulation of turbulent pipe flow through an abrupt axysimmetric constriction,” *Flow, Turbul. Combust.*, vol. 91, no. 1, pp. 1–8, 2013.

[38] A. Nilsson, J. Revstedt, E. Heiberg, F. Ståhlberg, and K. M. Bloch, “Volumetric velocity measurements in restricted geometries using spiral sampling: a phantom study.,” *Magn Reson Mater Phy*, 2014.

[39] N. Arun, S. Malavarayan, and M. Kaushik, “CFD ANALYSIS ON DISCHARGE CO-EFFICIENT DURING NON-NEWTONIAN FLOWS THROUGH ORIFICE METER,” *Int. J. Eng. Sci. Tchnology*, vol. 2, no. 7, pp. 3151–3164, Jan. 2010.

[40] T. A. Jankowski, E. N. Schmierer, F. C. Prenger, and S. P. Ashworth, “A Series Pressure Drop Representation for Flow Through Orifice Tubes,” *J. Fluids Eng.*, vol. 130, no. 5, p. 051204, May 2008.

[41] K. Ramamurthi and K. Nandakumar, “Characteristics of flow through small sharp-edged cylindrical orifices,” *Flow Meas. Instrum.*, vol. 10, no. 3, pp. 133–143, 1999.

[42] G. L. Morrison, R. E. DeOtte, M. Moen, K. R. Hall, and J. C. Hostle, “Beta ratio, swirl and Reynolds number dependence of wall pressurein orifice flowmeters,” *Flow Meas. Instrum.*, vol. 1, pp. 269–277, 1990.

[43] E. Muñoz-Díaz, F. J. Solorio-Ordaz, and G. Ascanio, “A numerical study of an orifice flowmeter,” *Flow Meas. Instrum.*, vol. 26, pp. 85–92, 2012.

[44] W. M. Dempster and B. Arebi, “Experimental characteristics of steam bubble growth at orifices in sub-cooled liquid,” *Int. Commun. Heat Mass Transf.*, vol. 28, no. 4, pp. 467–477, May 2001.

[45] L. C. B. S. Reis, J. A. Carvalho, M. A. R. Nascimento, L. O. Rodrigues, F. L. G. Dias, and P. M. Sobrinho, “Numerical modeling of flow through an industrial burner orifice,” *Appl. Therm. Eng.*, vol. 67, no. 1–2, pp. 201–213, Jun. 2014.

[46] S. Shaaban, “Optimization of orifice meter’s energy consumption,” *Chem. Eng.*

Res. Des., vol. 92, no. 6, pp. 1005–1015, Jun. 2014.

[47] F. Shan, A. Fujishiro, T. Tsuneyoshi, and Y. Tsuji, “Effects of flow field on the wall mass transfer rate behind a circular orifice in a round pipe,” *Int. J. Heat Mass Transf.*, vol. 73, pp. 542–550, 2014.

[48] R. J. K. Wood and T. F. Jones, “Investigations of sand–water induced erosive wear of AISI 304L stainless steel pipes by pilot-scale and laboratory-scale testing,” *Wear*, vol. 255, no. 1–6, pp. 206–218, Aug. 2003.

[49] B. Bozzini, M. E. Ricotti, M. Boniardi, and C. Mele, “Evaluation of erosion–corrosion in multiphase flow via CFD and experimental analysis,” *Wear*, vol. 255, no. 1–6, pp. 237–245, Aug. 2003.

[50] T. H. Shih, W. W. Liou, A. Shabbir, Z. Yang, and J. Zhu, “A New k- ε Eddy-Viscosity Model for igh Reynolds Number Turbulent Flows-Model Development and Validation,” *Comput. Fluids*, vol. 24, no. 3, pp. 227–238, 1995.

[51] W. C. Reynolds, “Fundamentals of turbulence for turbulence modelling and simulation.” pp. March 16–17, 1987, 1987.

[52] Z. H. Lin, “Two-phase flow measurements with sharp-edged orifices,” *Int. J. Multiph. Flow*, vol. 8, no. 6, pp. 683–693, Dec. 1982.

[53] M. T. Benchaita, P. Griffith, and E. Rabinowicz, “Erosion of Metallic Plate by Solid Particles Entrained in a Liquid Jet,” *J. Eng. Ind.*, vol. 105, no. 3, p. 215, Aug. 1983.

[54] J. Postlethwaite and S. Nesic, “Erosion in Disturbed Liquid/Particle Pipe Flow:

Effects of Flow Geometry and Particle Surface Roughness," *Corrosion*, vol. 49, no. 10, pp. 850–857, Oct. 1993.

[55] S. A. Morsi and A. J. Alexander, "An investigation of particle trajectories in two-phase flow systems," *J. Fluid Mech.*, vol. 55, no. 02, p. 193, Mar. 2006.

[56] B. S. McLaury, *Predicting Solid Particle Erosion Resulting from Turbulent Fluctuations in Oilfield Geometries*. 1996.

[57] J. K. Edwards, B. S. McLaury, and S. A. Shirazi, "Evaluation of Alternative Pipe Bend Fittings in Erosive Service," in *Proceedings of ASME Fluids Engineering Summer Meeting*, 2000, pp. FEDSM2000–11245.

[58] X. Chen, B. S. McLaury, and S. A. Shirazi, "Application and experimental validation of a computational fluid dynamics (CFD)-based erosion prediction model in elbows and plugged tees," *Comput. Fluids*, vol. 33, no. 10, pp. 1251–1272, Dec. 2004.

[59] F.-C. Li and K. Hishida, *Characterization of Flow, Particles and Interfaces*, vol. 37. Elsevier, 2009.

[60] R. J. Adrian, "Twenty years of particle image velocimetry," *Exp. Fluids*, vol. 39, no. 2, pp. 159–169, Jul. 2005.

[61] K. D. Hinsch and H. Hinrichs, "Three-Dimensional Particle Velocimetry," in *Three-Dimensional Velocity and Vorticity Measuring and Image Analysis Techniques*, vol. 4, T. Dracos, Ed. Dordrecht: Springer Netherlands, 1996, pp. 129–152.

[62] A. Melling, “Tracer particles and seeding for particle image velocimetry,” *Meas. Sci. Technol.*, vol. 8, no. 12, pp. 1406–1416, 1997.

[63] J. Westerweel, “Fundamentals of digital particle image velocimetry,” *Meas. Sci. Technol.*, vol. 8, no. 12, pp. 1379–1392, Dec. 1997.

[64] C. E. Willert, D. M. Mitchell, and J. Soria, “An assessment of high-power light-emitting diodes for high frame rate schlieren imaging,” *Exp. Fluids*, vol. 53, no. 2, pp. 413–421, Apr. 2012.

[65] Y. Agrawal, L. Talbot, and K. Gong, “Laser anemometer study of flow development in curved circular pipes,” *Journal of Fluid Mechanics*, 12-Apr-2006. [Online]. Available: http://journals.cambridge.org/abstract_S0022112078000762. [Accessed: 25-Nov-2015].

[66] M. L. Lowe and P. H. Kutt, “Refraction through cylindrical tubes,” *Exp. Fluids*, vol. 13, no. 5, Sep. 1992.

[67] R. Lindken and W. Merzkirch, “A novel PIV technique for measurements in multiphase flows and its application to two-phase bubbly flows,” *Exp. Fluids*, vol. 33, no. 6, pp. 814–825, Dec. 2002.

Vitae

Name : ARAOYE, ABDULRAZAQ ADENIYI

Nationality : NIGERIAN

Date of Birth : 04/09/1986

Email : razaq026@gmail.com

Address : No 167a, off lemor hotel Agura Sabo, Sagamu Ogun state

ACADEMIC BACKGROUND

King Fahd University of Petroleum & Minerals (KFUPM), Dhahran, Saudi Arabia
M.Sc. Mechanical Engineering (Distinction) 2016

Obafemi Awolowo University (OAU), Ile Ife, Osun State, Nigeria
B.Sc. Mechanical Engineering (First Class Honors) 2011

RESEARCH

Erosion downstream of a multiple orifice tube due to solid particles and/or turbulence intensity of two-phase flows, 2015.

Analysis of multi-phase flow (slug flow, bubbly flow) using Particle Image Velocimetry (PIV) measuring technique, 2013/2014.

Undergraduate Final Year Project: Fabrication and Performance Evaluation of a Laboratory-scale Fluidized bed Combustor

PUBLICATIONS

- **A.A. Araoye**, H.M. Badr, W.H. Ahmed, M.A. Habib and A. Alsarkhi, "Investigation of Solid Particle Erosion in a Multi-Stage Orifice Configuration", submitted to ASME J. Fluids Engineering for possible publication (February 23, 2016).
- **A.A. Araoy**e, H.M. Badr and W.H. Ahmed, "Flow Through Multi-Stage Restricting Orifices", Submitted to 3rd International Conference on Fluid Flow, Heat and Mass Transfer (FFHMT'16), Ottawa, Canada – May 2–3, 2016.

- O.E. Bamidele, S.A. Salaudeen, I.Z. Mohamed, **A.A. Araoye**, and L. Al-Hadhrami, "Numerical Analysis of Spray Coating Processes". International Journal of Modern Engineering Research, Vol. 5 Issue: 5 pp: 1-13, (2015).
- **A. Araoye**, W. H. Ahmed, A. Al-Sarkhi, H. M. Badr, I. H. Alsurakji, "Characterizing Drift Velocity for Two-Phase Flow Using Particle Image Velocimetry", Proceedings of the 8th International Conference on Computational and Experimental Methods in Multiphase and Complex Flow, Valencia, Spain, April 20-22, 2015.

MEMBERSHIPS

- SAP Professional
- International Project Management Professional (IPMP)

AWARDS

- WAPCO prize, best graduating student in Mechanical Engineering for 2009/2010 Session.
- Attained Vice Chancellor's List of Outstanding Students for 2009/2010 Session

COMPUTER SKILLS: Microsoft Office Suite, AUTOCAD, MATLAB, ANSYS

REFERENCES

- Professor Hassan M. Badr
  Mechanical Engineering Department
  King Fahd University of Petroleum & Minerals
  KFUPM Box # 322
  Dhahran: 31261, Saudi Arabia
  Tel.: +966-3-860-2543, Mobile: +966 50 843 9544
  Fax: +966-3-860-2949
  e-mail: badrhm@kfupm.edu.sa
- Professor Mohamed A. Habib
  Mechanical Engineering Department
  King Fahd University of Petroleum & Minerals
  KFUPM Box # 322
  Dhahran: 31261, Saudi Arabia
  Tel.: +966-3-860-4467,
  Fax: +966-3-860-2949
  e-mail: mahabib@kfupm.edu.sa
- Professor Palanichamy Gandhidassan
  Mechanical Engineering Department
  King Fahd University of Petroleum & Minerals
  KFUPM Box # 322
  Dhahran: 31261, Saudi Arabia
  Tel.: +966-3-860-2950,
  Fax: +966-3-860-2949
  e-mail: pgandhi@kfupm.edu.sa